Perspective on the Genesis of E-MORB from Chemical and Isotopic Heterogeneity at 9-10 degrees N East Pacific Rise

Chrisopher L. Waters, Kenneth W. W. Sims, Michael R. Perfit, Janne Blichert-Toft, J. Blusztajn

JOURNAL OF PETROLOGY | VOLUME 52 | NUMBER 3 | PAGES 565–602 | 2011 | doi:10.1093/petrology/egq091

Perspective on the Genesis of E-MORB from Chemical and Isotopic Heterogeneity at 9–10°N East Pacific Rise

CHRISTOPHER L. WATERS[1,2]*, KENNETH W. W. SIMS[2,3], MICHAEL R. PERFIT[4], JANNE BLICHERT-TOFT[5] AND JUREK BLUSZTAJN[3]

[1]DEPARTMENT OF GEOLOGY AND GEOPHYSICS, MASSACHUSETTS INSTITUTE OF TECHNOLOGY/WOODS HOLE OCEANOGRAPHIC INSTITUTION JOINT PROGRAM IN OCEANOGRAPHY, WOODS HOLE, MA 02543, USA

[2]DEPARTMENT OF GEOLOGY AND GEOPHYSICS, UNIVERSITY OF WYOMING, LARAMIE, WY 82071, USA

[3]DEPARTMENT OF GEOLOGY AND GEOPHYSICS, WOODS HOLE OCEANOGRAPHIC INSTITUTION, WOODS HOLE, MA 02543, USA

[4]DEPARTMENT OF GEOLOGICAL SCIENCES, UNIVERSITY OF FLORIDA, GAINESVILLE, FL 32611, USA

[5]UNIVERSITE DE LYON, CNRS, UMR 5570, ECOLE NORMALE SUPERIEURE, 46 ALLEE D'ITALIE, 69364 LYON, FRANCE

RECEIVED JANUARY 10, 2010; ACCEPTED DECEMBER 2, 2010
ADVANCE ACCESS PUBLICATION FEBRUARY 1, 2011

The discovery of chemically and isotopically enriched mid-ocean ridge basalts (E-MORB) has offered substantial insight into the origin, time scales, and length scales of mantle heterogeneity. However, the exact processes involved in producing this E-MORB enrichment are vigorously debated. Additionally, because the ages of E-MORB are not well constrained, the petrogenetic, temporal, and geological relationships between E-MORB and normal (N)-MORB are not known. To investigate these relationships and to explore how melting and melt transport processes contribute to or modify enriched mantle source compositions and generate E-MORB melts beneath mid-ocean ridges, we measured major and trace elements, and Sr, Nd, Hf, Pb, and U–Th–Ra isotopes for a suite of lavas that were collected off-axis, including several E-MORB, at 9–10°N along the East Pacific Rise (EPR). These data show coherent mixing trends among long-lived radiogenic isotopes, U-series nuclides, and incompatible trace elements, implying that mixing of melts from different sources occurs at different depths. Our results are consistent with previous studies that show that melting occurs in a two-porosity melting regime, with high-porosity channels forming deeply in the presence of garnet and transporting enriched melts with large ^{230}Th excesses to the crust, whereas low-porosity channels transport melts more slowly, allowing them to equilibrate at shallow depths and develop large ^{226}Ra excesses at the expense of diminished ^{230}Th excesses. Forward modeling of the trace element data also is consistent with mixing of melts in a two-porosity melting regime. U-series age constraints suggest that E-MORB neither erupt at systematically different times from N-MORB, nor necessarily through different pathways. Previous studies of E-MORB at 9–10°N have suggested that E-MORB compositions could be explained by off-axis eruption. However, when considered in light of previously published magnetic paleointensity and U-series age constraints, recent geological studies, and the most widely accepted contemporary understanding of volcanic construction at 9–10°N EPR, the asymmetric, off-axis distribution of E-MORB at 9–10°N EPR is consistent with, and more simply explained by, a model in which E-MORB erupted within the axial summit trough (AST) and flowed down the ridge flanks (~0–3 km). These E-MORB subsequently spread away from the AST, and, finally, were preserved on the seafloor through asymmetric construction of the extrusive layer. Taken together, the range of ages of E-MORB at 9–10°N EPR and the geochemical and isotopic mixing trends suggest that enriched melts are continuously supplied to the ridge axis, but because of their

*Corresponding author. Telephone: (307) 766-2020.
E-mail: cwaters@whoi.edu and cwaters3@uwyo.edu

small proportions relative to the volumetrically and volcanically dominant N-MORB, E-MORB preservation and exposure is comparatively scarce.

KEY WORDS: *East Pacific Rise; E-MORB; off-axis volcanism; petrogenesis; U-series*

INTRODUCTION

The formation of the continental crust from Earth's early mantle is thought to have left a complementary upper mantle reservoir largely depleted and broadly homogeneous with respect to its incompatible element abundances and long-lived radiogenic isotope compositions (e.g. Hurley, 1968; DePaolo & Wasserburg, 1976; Allègre *et al.*, 1983). This depleted reservoir, termed DMM (Zindler & Hart, 1986), or depleted MORB mantle, is considered to be the source of mid-ocean ridge basalts (MORB). However, long-term chemical heterogeneities in the oceanic mantle have long been known to exist at different length scales (e.g. Tatsumoto, 1966; Hedge & Peterman, 1970; Hart *et al.*, 1973; White & Schilling, 1978; Zindler & Hart, 1986; Sims & Hart, 2006). Even at a ridge segment far from the influence of any hotspot, such as at the East Pacific Rise (EPR), the adjacent and seemingly coeval occurrence of enriched (E-MORB), normal (N-MORB), and very depleted (D-MORB) MORB attests to the ubiquitous presence of old heterogeneous mantle domains over short length scales (e.g. Zindler *et al.*, 1984; Langmuir *et al.*, 1986; Fornari *et al.*, 1988, 1989; Allan *et al.*, 1989; Hekinian *et al.*, 1989; Prinzhofer *et al.*, 1989; Reynolds *et al.*, 1992; Mahoney *et al.*, 1994; Perfit *et al.*, 1994; Niu & Batiza, 1977; Lundstrom *et al.*, 1999; Niu *et al.*, 1999, 2002; Castillo *et al.*, 2000; Reynolds & Langmuir, 2000; Sims *et al.*, 2002). Although the isotopic and chemical heterogeneity of the present-day mantle almost certainly represents the continuous processes of differentiation and remixing, the origin of these enriched mid-ocean ridge mantle domains and the genesis of E-MORB are still vigorously debated. Furthermore, because the ages of E-MORB are not well constrained, the petrogenetic, temporal, and geological relationships between the less abundant E-MORB and volumetrically predominant N-MORB are poorly known.

To investigate how melting and melt transport processes modify enriched mantle source compositions and generate E-MORB melts beneath mid-ocean ridges, and to understand the geological and temporal relationships between N-MORB and E-MORB, we measured major and trace elements, and Sr, Nd, Hf, Pb, and U–Th–Ra isotopes for a suite of off-axis lavas, including several E-MORB, collected at 9–10°N along the East Pacific Rise. These samples were collected using the deep submersible *Alvin* and, hence, their spatial and geological contexts are well known (Fig. 1). U-series model ages of E-MORB and N-MORB provide an additional temporal context within which to interpret geochemical and isotopic variability, which reflect time-dependent variations in mantle melting processes and source compositions.

PREVIOUS STUDIES OF E-MORB GENESIS

Although ocean floor basalts classified as E-MORB span a wide range, and often a continuum, of enrichment, several compositional characteristics are observed to be common to all E-MORB, as follows.

(1) E-MORB tend to have slightly higher Al_2O_3 and lower FeO than N-MORB.
(2) E-MORB are more enriched than N-MORB in highly incompatible trace elements such as Rb, Ba, Th, U, and Nb by more than roughly an order of magnitude.
(3) E-MORB have more fractionated highly incompatible trace elements than N-MORB (e.g. La/Sm is ~3 times that in N-MORB, and Ba/La up to ~5 times that in N-MORB).
(4) In contrast to the light rare earth elements (LREE), heavy rare earth elements (HREE) are nearly chondritic [e.g. $(Dy/Yb)_N \sim 1$].
(5) The Sr isotope compositions of E-MORB tend to be more radiogenic than those of N-MORB, whereas Nd and Hf isotope compositions tend to be less radiogenic, reflecting enrichment of the more incompatible element (i.e. Rb, Nd, Hf) in the parent/daughter ratios Rb/Sr, Sm/Nd, and Lu/Hf that control the long-term radiogenic ingrowth.
(6) Young E-MORB also almost always have large ^{230}Th excesses [i.e. $(^{230}Th/^{238}U) > 1$] but small ^{226}Ra excesses [i.e. $(^{226}Ra/^{230}Th) > 1$] compared with the relatively small ^{230}Th excesses and large ^{226}Ra excesses of zero-age N-MORB (and even smaller ^{230}Th excesses and larger ^{226}Ra excesses of young D-MORB) (see Volpe & Goldstein, 1990; Goldstein *et al.*, 1992, 1994; Sims *et al.*, 1995, 2002, 2003; Lundstrom *et al.*, 1999).

In the past, definitions of E-MORB have often relied on relative trace element enrichments, such as high K/Ti (defined as $K_2O/TiO_2 \times 100$), Zr/Y, La/Sm, and Th/U without the supporting isotopic information on long-term source enrichment (e.g. Langmuir *et al.*, 1986; Batiza & Niu, 1992; Lundstrom *et al.*, 1999; Perfit *et al.*, 1994; Smith *et al.*, 2001). Prior to this work, studies of seamount lavas from near 9–10°N EPR (Zindler *et al.*, 1984; Fornari *et al.*, 1988, 1989; Prinzhofer *et al.*, 1989; Niu & Batiza, 1997; Niu *et al.*, 1999, 2002) and lavas from the nearby Siqueiros Fracture Zone at 8°25′N EPR (Sims *et al.*, 2002) have demonstrated the presence of isotopic source heterogeneity beneath this region of the EPR. However, there are no

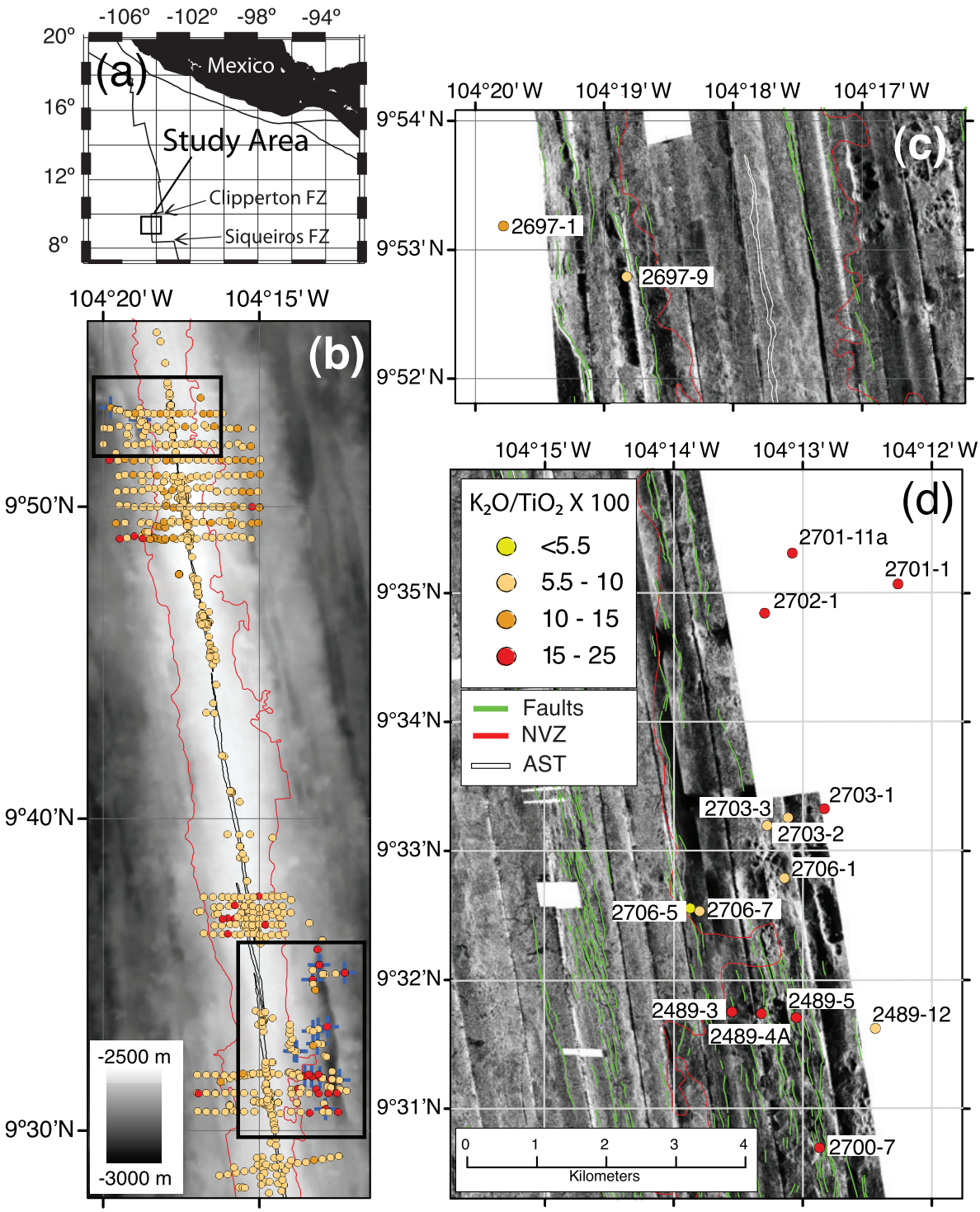

Fig. 1. Sample location maps for 9–10°N East Pacific Rise (EPR). (a) Map of the study area with respect to Mexico, the EPR from 8°N to 19°N, and the Clipperton and Siqueiros Fracture Zones (FZ). (b) Multibeam bathymetry (Cochran *et al.*, 1999) underlies sample locations for samples collected from 9°29′N to 9°55′N EPR by rock core and *Alvin* (Perfit *et al.*, 1994; Perfit & Chadwick, 1998; Smith *et al.*, 2001; Sims *et al.*, 2002, 2003). Variations in sample K/Ti ($K_2O/TiO_2 \times 100$) are shown by colored symbols [key as in (d)]. Blue crosses indicate samples analyzed in this study. Focus areas of this study are outlined by black rectangles and expanded to the right, showing side-scan sonar imaging for (c) the western side of the 9°50′N region and (d) the eastern side of the AST at 9°30′N–9°35′N (Fornari *et al.*, 2004). Samples are colored as in (b). NVZ, neo-volcanic zone; AST, axial summit trough; boundaries are from Soule *et al.* (2009). Fault locations are from Escartin *et al.* (2007). All samples from this study were collected from outside of the neo-volcanic zone; enriched MORB from 9°30′N were recovered from more highly tectonized terrain.

isotopic data establishing the presence of a heterogeneous mantle source in the immediate area near the axis from 9°17′N to 10°N EPR (Sims *et al.*, 2002, 2003). In fact, the samples selected for this study were defined as N-MORB and E-MORB according to the classification by Smith *et al.* (2001), which defines N-MORB as lavas with K/Ti < 11 and E-MORB as lavas with K/Ti > 11 (Fig. 2), with the explicit goal of looking for isotopic heterogeneity. Because incompatible elements can be enriched and their ratios fractionated by processes such as small extents of

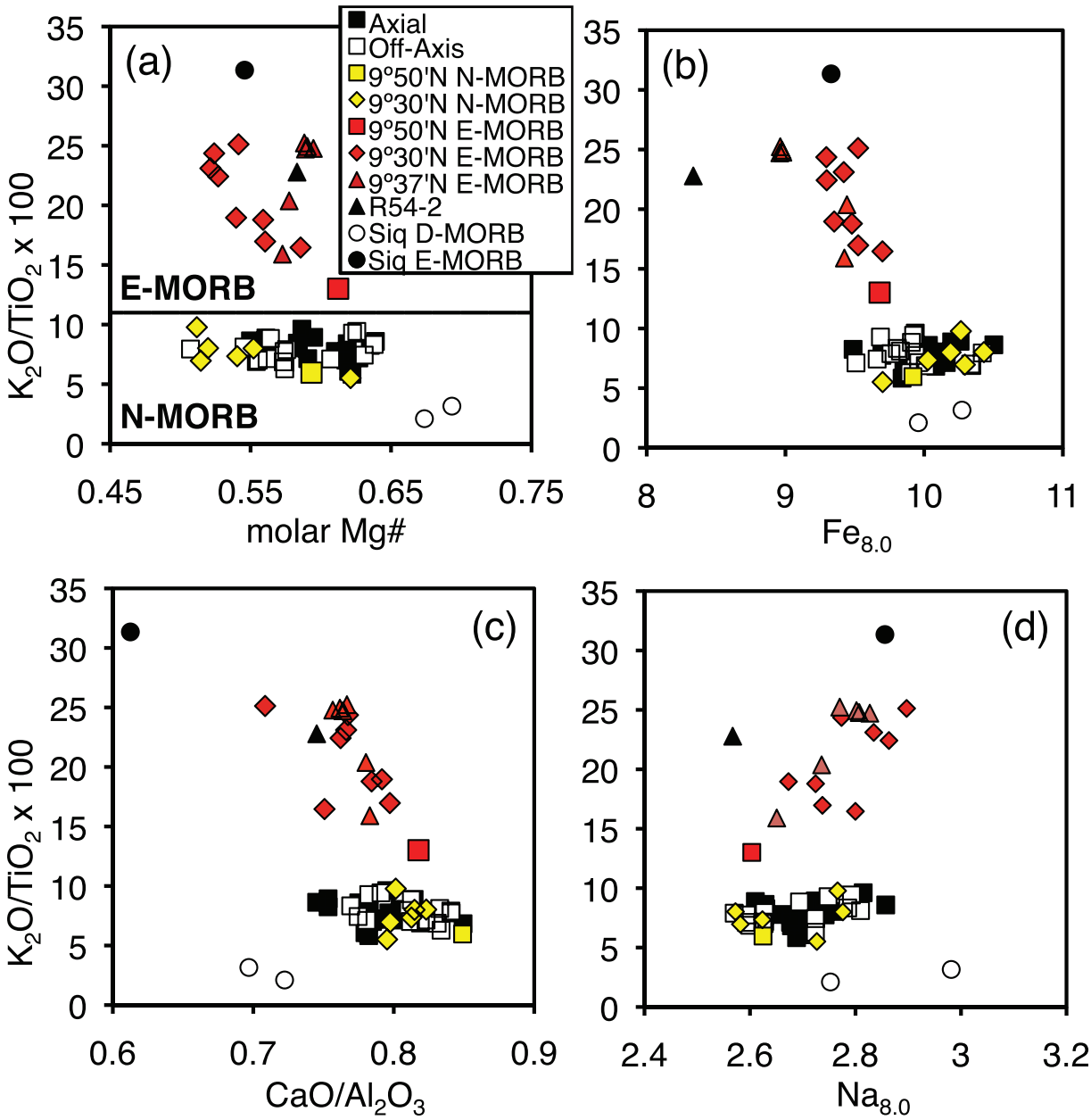

Fig. 2. (a) Plot of molar Mg-number vs K/Ti (wt % $K_2O/TiO_2 \times 100$). The horizontal dashed line at K/Ti = 11 separates fields for N-MORB (<11) and E-MORB (>11) (Smith *et al.*, 2001). Lavas collected off-axis and labeled 9°30′N and 9°50′N N-MORB and E-MORB are from this study. 'Axial' samples are from 9°17′N to 9°54′N (Sims *et al.*, 2002). 'Off-axis' samples were collected near 9°50′N (Sims *et al.*, 2003). E-MORB sample R54-2 was dredged from 9°35′N (Batiza & Niu, 1992). Also shown are E-MORB from the small OSC at 9°37′N (Smith *et al.*, 2001). Siqueiros data are from Perfit *et al.* (1996). (b) Plot of $Fe_{8\cdot0}$ vs K/Ti. $Fe_{8\cdot0}$ is negatively correlated with K/Ti (as is Fe_{72}; Niu & O'Hara, 2008), where E-MORB trend to lower $Fe_{8\cdot0}$ and higher K/Ti than N-MORB. Similarly, (c) CaO/Al_2O_3 is negatively correlated with K/Ti. (d) $Na_{8\cdot0}$ is positively correlated with K/Ti. These correlations suggest that E-MORB melts derive from a greater contribution of garnet than N-MORB—more garnet results in higher Al_2O_3 concentration and lower CaO/Al_2O_3, and a more fertile mantle corresponds to more Na-rich clinopyroxene, a higher clinopyroxene/olivine abundance ratio, and lower Fe, Mg, and Mg-number (Niu *et al.*, 2008).

melting (see Sims & DePaolo, 1997) without the presence of a long-term enriched mantle source reservoir, definitions of E-MORB based on incompatible element abundances and ratios alone are insufficient. Comparison of long-lived radiogenic isotope compositions (i.e. Sr, Nd, Hf, Pb) with incompatible element ratios and U-series isotopic data is required to decipher the relative effects of partial melting versus the presence of source heterogeneity over the length scale of melting (see Sims & DePaolo, 1997) and, hence, to determine the origin of E-MORB.

Enriched source compositions for E-MORB are generally argued to derive from either melt metasomatism of peridotite, either cryptically or in the form of fine dikes or veins (e.g. Galer & O'Nions, 1986; Niu *et al.*, 2002; Donnelly *et al.*, 2004), or from formation of garnet pyroxenite or eclogite veins through stretching and thinning of subducted and recycled oceanic crust (e.g. Allègre & Turcotte, 1986; Prinzhofer *et al.*, 1989; Ben Othman & Allègre, 1990; Hirschmann & Stolper, 1996; Lundstrom *et al.*, 1999). In all models positing a metasomatic origin for E-MORB, a common requirement is that an earlier episode of low-degree melting of some other enriched mantle source must occur to generate the elevated highly incompatible trace element abundances (Niu *et al.*, 2002; Donnelly *et al.*, 2004). Proposed low-degree melt mechanisms include metasomatism of overlying mantle by melting of eclogitized recycled crust in subduction zones (Donnelly *et al.*, 2004), metasomatism by melting of mantle within the low-velocity zone beneath oceanic lithosphere (Niu *et al.*, 2002), and metasomatism of subcontinental lithosphere and subsequent delamination (Galer & O'Nions, 1986). These low-degree melt-metasomatized mantle packages subsequently undergo larger extents of melting (up to 10%) beneath ocean ridges as spinel peridotite to produce E-MORB (Donnelly *et al.*, 2004). An absence of residual garnet in the E-MORB source is used to explain the observed chondritic Dy/Yb observed in most E-MORB (Donnelly *et al.*, 2004). However, this inference is contradictory to the observation that E-MORB typically have large Th excesses (Goldstein *et al.*, 1992, 1994; Lundstrom *et al.*, 1995, 1998, 1999; Sims *et al.*, 1995, 2002), which most probably indicates residual garnet in the source (Beattie, 1993; LaTourrette *et al.*, 1993; Hauri *et al.*, 1994; Salters & Longhi, 1999; Salters *et al.*, 2002; Pertermann *et al.*, 2004; Elkins *et al.*, 2008).

Production of E-MORB by melting of mafic components in a mixed-lithology mantle of pyroxenitic–eclogitic recycled crust and peridotite calls for recent ($\ll$375 ka) low-degree melting in the presence of garnet to generate the large observed ^{230}Th excesses, followed by efficient segregation and preservation of these low-degree melts. Melting of mafic veins has been proposed to explain U–Th disequilibria in E-MORB (e.g. Ben Othman & Allègre, 1990; Lundstrom *et al.*, 1995, 1998, 1999; Hirschmann & Stolper, 1996), but in the absence of isotopic heterogeneity, deep, low-degree melting of unmetasomatized garnet peridotite could also potentially explain the observed ^{230}Th excesses (Sims *et al.*, 2002).

Although both the 'metasomatic' and 'recycling' models provide potential explanations for the ultimate origin of the long-term E-MORB mantle source reservoir, they do not account for how enriched melt compositions are preserved from the time the enriched mantle source melts beneath the mid-ocean ridge to the time they are erupted on the seafloor. For example, E-MORB from the fast-spreading ridge at 9°17′–10°N EPR (Batiza & Niu, 1992; Perfit *et al.*, 1994; Perfit & Chadwick, 1998; Smith *et al.*, 2001) and similarly enriched MORB from 17°30′S EPR and from 12 to 13°N EPR (Reynolds *et al.*, 1992; Reynolds & Langmuir, 2000; Bergmanis *et al.*, 2007) have been sampled adjacent to N-MORB, suggesting that N-MORB and E-MORB melts are either generated and erupted at discrete time intervals (e.g. Hekinian *et al.*, 1989; Batiza & Niu, 1992; Reynolds *et al.*, 1992; Bergmanis *et al.*, 2007) or are extracted and transported to the seafloor along different mantle and crustal pathways (e.g. Perfit *et al.*, 1994). In addition, it has also been suggested that E-MORB erupted near the axis at the small overlapping spreading center (OSC) at 9°37′N on the EPR could reflect waning magmatism beneath the retreating limb of the OSC (Smith *et al.*, 2001).

Coupled U-series and long-lived radiogenic isotope studies examining the relationship between E-MORB and N-MORB have suggested that mixing of deep, small-degree melts with shallow, high-degree melts is required to produce correlations between U–Th disequilibria and Sm/Nd fractionation (Sims *et al.*, 1995, 2002). Consistent with the predictions of Kelemen *et al.* (1997), studies of U-series disequilibria in demonstrably young (relative to the half-life of ^{226}Ra) 9–10°N EPR N-MORB lavas have shown that for lavas to have both negatively correlated primary ^{226}Ra and ^{230}Th excesses and positively correlated (^{230}Th/^{232}Th) and (^{238}U/^{232}Th), the melting must occur in a two-porosity mantle, with high-porosity channels forming deeply in the presence of garnet and transporting melts with large ^{230}Th excesses to the crust, whereas low-porosity channels transport melts more slowly, allowing them to equilibrate at shallow depths and develop large ^{226}Ra excesses at the expense of diminished ^{230}Th excesses (Sims *et al.*, 1999; Lundstrom, 2000; Jull *et al.*, 2002; Sims *et al.*, 2002). Hence, given the observation of large ^{230}Th and small ^{226}Ra excesses in E-MORB, we hypothesize that E-MORB represent deep melts of an enriched source that have been segregated into high-porosity channels and largely removed from interaction with incompatible element-depleted, peridotitic N-MORB melts.

GEOLOGICAL BACKGROUND, SAMPLE LOCATIONS, EXISTING DATA, AND PRIOR MODELS

The second-order ridge segment at 9–10°N East Pacific Rise (EPR) is fast-spreading with a half-spreading rate of ~5·5 cm a^{-1}. Magnetic data show that it has been spreading at this rate for the last 2 Myr (Carbotte & Macdonald, 1992). This segment of the EPR is far from the influence of hotspot interaction and erupts predominantly N-MORB. It is bounded to the north by the Clipperton transform fault at 10°10′N and to the south by a large OSC at 9°03′N (Macdonald *et al.*, 1984). It is interrupted by a third-order ridge discontinuity with a ~0·45 km offset and 3 km overlap at ~9°36–9°38′N, which has been termed a 'small OSC' (Smith *et al.*, 2001). This discontinuity is thought to represent a volcanological divide: the eastern limb of the axial summit trough (AST) appears to be propagating southward, whereas magmatic activity on the western limb appears to be waning (Smith *et al.*, 2001). This interpretation is based on differences in lava geochemistry, a reduction in seismically determined melt volume as the OSC is approached (Dunn *et al.*, 2000), the presence of extinct hydrothermal vents and older-looking lava flows to the south of the discontinuity, and observations of younger-looking lava flows and hydrothermal activity indicative of a more recent eruption to the north (Smith *et al.*, 2001). North of 9°38′N, the ridge segment near 9°48′N–9°52′N has a broad, inflated bathymetric cross-sectional profile with a shallow, narrow (~50 m) AST and is considered magmatically robust (Scheirer & Macdonald, 1993; Fornari *et al.*, 1998; Cochran *et al.*, 1999). Two eruptions have been documented north of 9°38′N near 9°50′N during 1991–1992 and 2005–2006 (Haymon *et al.*, 1993; Tolstoy *et al.*, 2006; Soule *et al.*, 2007; Goss *et al.*, 2010) with no corresponding volcanism south of the small OSC. The profile at 9°31′N is flatter, with a deeper, wider (~250 m) AST nested within the broad summit depression of a developing axial summit graben (ASG) (Fornari *et al.*, 1998; Scheirer & Macdonald, 1993). Hence, the ridge south of 9°36′N to ~9°30′N is thought to be magmatically 'starved' in comparison with the segment from 9°48′N to 9°52′N.

Previous sampling of over 1200 basalts from between 9°17′N and 10°N EPR (major element compositions for ~300 samples can be found at www.petdb.org) has documented eight E-MORB (defined by K/Ti > 11) near 9°30′N, with seven of the eight samples deriving from the east side of the AST (Perfit *et al.*, 1994; Perfit & Chadwick, 1998). Ten E-MORB were collected by wax-filled rock core at the small OSC at 9°36′–9°38′N (Smith *et al.*, 2001). Seven of these samples were collected from west of the western limb, two from east of the eastern limb, and one from between the two limbs (Fig. 1; see also Smith *et al.*, 2001, fig. 4). One E-MORB was also collected by dredging from SE of the western limb of the discontinuity at 9°35′N and has been measured for its Sr, Nd, Pb, ($^{238}U/^{232}Th$), ($^{230}Th/^{232}Th$), and ($^{226}Ra/^{230}Th$) isotopic compositions (sample R54-2; Harpp *et al.*, 1990; Batiza & Niu, 1992; Volpe & Goldstein, 1993; Goldstein *et al.*, 1994). Although there has been extensive sampling within and immediately adjacent to the AST, no E-MORB have been recovered from the axial region (<~0·5 km) anywhere along 9°17′N–10°N EPR (Fig. 1).

The existence of E-MORB in the study area suggests that MORB genesis is more complicated than what has been inferred solely from N-MORB compositions (Sims *et al.*, 2002, 2003). Although incompatible element ratios (e.g. K/Ti, Nb/Th, Th/U, Zr/Y) by themselves cannot be used to infer source characteristics, the higher abundances of moderately and highly incompatible trace elements in E-MORB require generation of enriched parental melts, whether by melting of a heterogeneous mantle source or by low degrees of melting of a homogeneous source, and subsequent preservation of these melts. More recent studies of global E-MORB have indicated that low degrees of melting of a homogeneous peridotitic mantle source alone cannot produce the trace element patterns of E-MORB. In particular, at the very low extents of melting necessary for producing the large fractionations observed in E-MORB of highly incompatible elements such as Th and U, not only are these highly incompatible elements too abundant, but more moderately incompatible elements, such as the HREE, are also too fractionated and have too low abundances to match the composition of typical E-MORB (Donnelly *et al.*, 2004).

Previous studies of E-MORB at 9–10°N EPR have arrived at two models for the emplacement of E-MORB melts (Batiza & Niu, 1992; Perfit *et al.*, 1994; Smith *et al.*, 2001). Based on $^{226}Ra/^{230}Th$–Ba/Th model age dating of dredged samples from 9°32′N to 9°36′N, including two N-MORB (9°32′N–9°33′N) and one E-MORB (9°36′N; Volpe & Goldstein, 1990, 1993), and following the model of Hekinian *et al.* (1989), Batiza & Niu (1992) suggested that E-MORB (T_{model} ~ 6·40 kyr) were generated from an older episode of magmatic activity different from that which produced N-MORB (T_{model} ~ 2·40–2·65 kyr). This older episode potentially involved progressive melting and persistent depletion of a heterogeneous mantle source over time. In essence, Batiza & Niu (1992) suggested, as did Reynolds *et al.* (1992) for 12°N EPR and Bergmanis *et al.* (2007) for 17°S EPR, that periods of E-MORB eruption may alternate with periods dominated by N-MORB eruption, reflecting temporal changes in the composition of magma supplied to the axial magma chamber (AMC). A specific case of this model has been proposed to account for the preservation and emplacement of E-MORB near the ridge axis (<1 km) at 9°37′N EPR (Smith *et al.*, 2001).

Smith *et al.* (2001) proposed that E-MORB melts may be erupted near the AST in locations of waning magmatism, where the extent of melting in the mantle is lower and/or the extent of crystallization is greater, such as at the retreating western limb of the small OSC at 9°37′N. In such a setting, melt mixing may be inhibited in locations of structural offsets at times when magmatic systems are poorly developed and contain relatively low volumes of N-MORB melt.

Shortly after the Volpe & Goldstein (1990, 1993) and Batiza & Niu (1992) studies were published, Goldstein *et al.* (1994) showed, using ages calculated from ^{238}U–^{230}Th and ^{235}U–^{231}Pa disequilibria, that N-MORB lavas collected from up to ~4 km off-axis had anomalously young ages (i.e. younger than would be inferred from the spreading rate). Because the lavas were anomalously young and collected off-axis, Goldstein *et al.* (1994) inferred that these lavas were also erupted off-axis. Based partly on these observations of anomalously young off-axis N-MORB (Goldstein *et al.*, 1994), Perfit *et al.* (1994) suggested an alternative explanation for the emplacement of E-MORB melts, in which the nearby E-MORB, which even today have only been sampled off-axis from the 9–10°N region, were also young and erupted off-axis. Given the off-axis location of E-MORB, Perfit *et al.* (1994) further suggested that E-MORB melts might be transported through off-axis pathways that allowed them to escape extensive mixing with the more voluminous N-MORB melts that reside in the AMC. Finally, Perfit *et al.* (1994) suggested that off-axis thickening of seismic layer 2A could be due to extensive intrusive and extrusive activity (both E-MORB and N-MORB) outside the AST and on the ridge flanks.

However, the studies of Batiza & Niu (1992), Goldstein *et al.* (1994) and Perfit *et al.* (1994) were published prior to the first high-resolution DSL-120A 120 kHz side-scan sonar imaging at 9–10°N EPR that covered the ridge flanks up to ~4 km on either side (Schouten *et al.*, 2001, 2002; Sims *et al.*, 2003; Fornari *et al.*, 2004), which clearly shows that the dominant feature surrounding the ridge crest is highly reflective, scalloped terrain. The nature of this ubiquitous ridge flank terrain has been confirmed during *Alvin* dive observations from towed camera seafloor photographs and ABE microbathymetry as young, gravity-driven lobate and sheet flows that overflow the AST and travel down the ridge flanks (e.g. Kurras *et al.*, 2000; Fornari *et al.*, 2004; Soule *et al.*, 2005, 2007, 2009; Escartin *et al.*, 2007). Thus, the most important mechanism for constructing the uppermost volcanic layer of the oceanic crust is axially erupted lava that overflows the AST and flows down the ridge flanks for distances of up to ~2–4 km. Stochastic models of crustal accretion using both bimodal (Hooft *et al.*, 1996) and unimodal (Bowles *et al.*, 2006) lava flow volumes sourced at the AST, as well as inverse modeling of magnetic data (Schouten *et al.*, 1999), support this notion as they reconstruct well the extrusive layer thickness and/or geometry as inferred from seismic studies of layer 2A (Harding *et al.*, 1993; Christeson *et al.*, 1994, 1996; Vera & Diebold, 1994; Sohn *et al.*, 2004).

Side-scan sonar data (e.g. Schouten *et al.*, 2001, 2002; White *et al.*, 2002; Sims *et al.*, 2003; Fornari *et al.*, 2004) also reveal that pillow ridges or mounds (and by inference off-axis volcanic eruptions, although some pillow mounds occur within <0·5 km of the AST, most commonly near third-order segment boundaries; White *et al.*, 2002) constitute only a volumetrically small component of volcanic crustal accretion, and U-series model ages indicate that at least some of this off-axis volcanic activity is young (Sims *et al.*, 2003). More recent geochemical studies, such as that of Sims *et al.* (2003) and Hinds (2004), have examined some of these off-axis pillow ridges in detail and revealed that they are not composed of E-MORB. Rather, many of the lava samples from pillow ridges are on the geochemically depleted side of the N-MORB spectrum and have Nd, Hf, Sr, and Pb isotope compositions similar to those of the adjacent axial N-MORB (Sims *et al.*, 2003). And yet—despite the widely accepted contemporary view that N-MORB volcanism and present-day volcanic accretion occur predominantly by eruption within the AST, overflow of the AST, and flow down the ridge flanks in lava channels and tubes—the persistent belief remains that E-MORB are erupted primarily off-axis as pillow mounds in the 9–10°N EPR region (with the possible exception of lavas erupted near the AST at the small OSC at 9°37′N). In this regard, it is worth noting that this view is not held for other fast-spreading ridge segments, where E-MORB lavas have been collected within the axial graben and even from sheet flows (e.g. Hekinian *et al.*, 1989; Reynolds *et al.*, 1992).

To shed light on how melting and melt transport processes—in particular two-porosity melt transport—contribute to or modify enriched mantle source compositions and generate E-MORB melts beneath mid-ocean ridges, we analyzed major and trace element abundances, Sr, Nd, Hf, and Pb isotope compositions, and U–Th–Ra disequilibria for a suite of 16 off-axis N- and E-MORB glasses from 9°31′N to 9°54′N EPR. These glasses were collected off-axis during the AdVenture Series cruises (dive 2489; see Perfit & Chadwick, 1998, fig. 20; Kutza, 2002) from 1991 to 1997 and during the Abyssal Hill Cruise (dives 2697, 2700, 2701, 2702, 2703, 2706) in 1992 (Alexander & Macdonald, 1996*a*, 1996*b*; Macdonald *et al.*, 1996; Kutza, 2002) with the submersible *Alvin* from lava flows <4 km west of the axis at 9°50′N and <5 km east of the axis at 9°31–9°35′N (herein referred to as 9°30′N). Hence, the location and geological context of these samples are relatively well known (Fig. 1, Table 1). Given model

Table 1: Sample descriptions and locations of 9°30′N and 9°50′N EPR off-axis samples, summarized from Kutza (2002)

Sample	Long. (W)	Lat. (N)	Time of collection	Depth (m)	Distance from AST (km)	Description
9°50′N EPR						
2697-1	104°19·779′	9°53·186′	10:28	2774	3·52	Pillow from middle of outward dipping fault west of AST; 30% plag/olivine phenocrysts in variolitic, glassy groundmass
2697-9	104°18·826′	9°52·792′	13:09	2695	1·90	Truncated pillow from the top of an outward dipping fault from trough west of axis
9°30′N EPR						
2489-3	104°13·548′	9°31·752′	11:23	2664	2·24	Well-formed pillows from small pillow mound
2489-4a	104°13·320′	9°31·740′	11:47	2689	2·64	Pillow bud from west-facing pillow ridge next to east-facing scarp; <5% plag + cpx + olivine microphenocrysts in glassy microlitic groundmass
2489-5	104°13·050′	9°31·710′	12:18	2722	3·12	Pillow fragment from heavily sedimented depression; few plag + cpx microphenocrysts in glassy groundmass
2489-12	104°12·438′	9°31·626′	14:40	2692	4·20	Round pillow bud
2700-7	104°12·870′	9°30·700′	14:28	2711	3·15	Lobate flow from top of outward dipping fault bounding a graben
2701-1	104°12·260′	9°35·070′	10:15	2806	5·00	Elongate old pillow from middle of outward dipping fault to east of 9°35′
2701-11a	104°13·080′	9°35·310′	13:16	2840	3·64	Pillow in off-axis graben
2702-1	104°13·296′	9°34·846′	10:20	2706	3·08	Pillow in graben or on outward dipping fault east of axis at 9°35′ south of dive 2701
2703-1	104°12·811′	9°33·327′	10:13	2812	3·88	Pillow in graben to south and west
2703-2	104°13·115′	9°33·260′	10:54	2725	3·33	Bulbous pillow from middle of outward dipping fault
2703-3	104°13·277′	9°33·197′	11:12	2687	3·00	Bulbous decorated pillow on top of outward dipping fault
2706-1	104°13·141′	9°32·792′	2:09	2676	3·15	Pillow at base of outward dipping fault between trough and ridge at 9°32·5′N
2706-5	104°13·801′	9°32·534′	5:31	2592	1·90	Pillow from the base of an inward dipping fault covered with talus; dark, aphyric groundmass with subaligned microlites and many vesicles
2706-7	104°13·871′	9°32·557′	12:28	2623	1·80	Hackly sheet flow in local graben at summit of outward dipping fault

In this and following tables, enriched MORB (E-MORB) are designated by bold sample numbers. Locations are shown in Fig. 1.

eruption-age constraints from ^{238}U–^{230}Th and ^{230}Th–^{226}Ra disequilibria and accurate knowledge of the spatial distribution of E-MORB relative to N-MORB at 9–10°N, we place new constraints on the temporal variability of the isotopically and elementally heterogeneous EPR mantle and explore an axial versus off-axis origin for E-MORB.

ANALYTICAL METHODS

The analytical details for major element analyses by electron microprobe are reported in the footnotes to Table 2. Details for trace element concentration data obtained by inductively coupled plasma mass spectrometry (ICP-MS) are reported in the footnotes to Table 3. Isotopic compositions were measured by multicollector (MC)-ICP-MS at WHOI and at the Ecole Normale Supérieure in Lyon, and details of these measurements are reported in the footnotes to Table 4. ^{238}U and ^{232}Th concentrations were measured at WHOI by isotope dilution (ID)-ICP-MS using a ThermoFinnigan Element 2, whereas $^{234}U/^{238}U$, $^{230}Th/^{232}Th$, and ID ^{226}Ra were measured using the WHOI ThermoFinnigan Neptune MC-ICP-MS system. The analytical details are reported in the footnotes to Table 5. Further information on the ^{238}U–^{230}Th–^{226}Ra chemical and analytical procedures at WHOI has been given by Sims *et al.* (2008*a*, appendix A1), and further details of the Th and U isotopic measurement methods and standards have been summarized by Ball *et al.* (2008) and Sims *et al.* (2008*b*). It should be noted that all the Th and U data plotted in various figures are ID data, with the exception of the data for samples 2489-5 and 2703-1, for which no ID data exist. For these two samples, solution ICP-MS Th and U data from the University of Florida have been used instead.

The data for 9°50′N off-axis lavas reported by Sims *et al.* (2003), compiled from ICP-MS data produced by the Geological Survey of Canada (GSC), plot at values for

Table 2: Major element compositions (weight per cent oxide) of 9°30′N and 9°50′N EPR glasses by electron microprobe analysis

Sample	SiO_2	TiO_2	Al_2O_3	FeO^T	MnO	MgO	CaO	Na_2O	K_2O	P_2O_5	Total	(K_2O/TiO_2) ×100	Mg-no.
9°50′N EPR													
2697-1	49·0	1·23	15·4	9·36	0·14	8·30	12·6	2·51	0·16	0·15	98·92	13·0	0·61
2697-9	50·1	1·34	14·7	9·85	0·15	8·06	12·5	2·61	0·08	0·11	99·39	6·0	0·59
9°30′N EPR													
2489-3	51·0	1·83	14·5	10·71	0·20	6·69	11·0	3·26	0·41	0·28	99·87	22·4	0·53
2489-4a	51·0	1·80	14·4	10·88	0·19	6·65	11·0	3·25	0·42	0·26	99·86	23·1	0·52
2489-5	51·0	1·79	14·4	10·76	0·21	6·65	11·1	3·19	0·44	0·31	99·85	24·4	0·52
2489-12	50·3	2·00	14·1	11·56	0·22	6·80	11·3	3·14	0·20	0·22	99·84	9·8	0·51
2700-7	49·8	1·65	14·8	10·25	0·23	7·29	11·6	2·94	0·31	0·19	98·97	18·8	0·56
2701-1	49·4	1·64	15·6	9·88	0·17	7·83	11·7	2·85	0·27	0·19	99·55	16·5	0·59
2701-11a	49·7	1·74	14·5	10·52	0·18	6·92	11·5	3·01	0·33	0·22	98·65	19·0	0·54
2702-1	49·7	1·65	14·7	10·25	0·16	7·33	11·7	2·94	0·28	0·19	98·85	17·0	0·56
2703-1	49·1	2·03	15·3	10·59	0·20	7·01	10·8	3·20	0·51	0·33	99·00	25·1	0·54
2703-2	50·2	1·87	13·9	11·52	0·25	6·99	11·4	2·88	0·15	0·17	99·29	8·0	0·52
2703-3	50·1	1·75	14·4	10·78	0·21	7·46	11·7	2·94	0·14	0·17	99·59	8·0	0·55
2706-1	50·7	1·77	14·1	10·90	0·22	7·19	11·5	2·87	0·13	0·15	99·52	7·3	0·54
2706-5	50·4	2·01	13·9	11·53	0·17	6·86	11·1	2·93	0·14	0·17	99·14	7·0	0·51
2706-7	50·5	1·27	15·2	9·20	0·19	8·46	12·1	2·58	0·07	0·11	99·74	5·5	0·62
Standards													
USNM (accepted-XRF)	51·52	1·30	15·39	9·13	0·17	8·21	11·31	2·48	0·09	0·12	99·72		
USNM (accepted-EMPA)	51·77	1·29	15·13	9·04	0·16	8·03	11·12	2·78	0·08	0·12	99·52		
USNM (meas.)	51·46	1·32	15·18	9·24	0·17	8·16	11·29	2·64	0·08	0·13	99·68		
SD ($n=8$)	0·08	0·04	0·09	0·06	0·01	0·06	0·05	0·03	0·01	0·01			
USNM (meas.)	51·45	1·33	15·13	9·25	0·17	8·21	11·31	2·65	0·09	0·13	99·74		
SD ($n=15$)	0·22	0·01	0·15	0·06	0·01	0·06	0·04	0·07	0·00	0·01			
A99 (accepted-XRF)	50·94	4·06	12·49	13·30	0·15	5·08	9·30	2·66	0·82	0·38	99·18		
A99 (accepted-EMPA)	51·06	3·95	12·44	13·15	0·19	5·04	9·04	2·72	0·82	0·43	98·84		
A99 (meas.)	51·18	4·06	12·50	13·48	0·19	5·19	9·25	2·70	0·99	0·49	100·03		
SD ($n=10$)	0·23	0·04	0·14	0·09	0·02	0·05	0·07	0·10	0·01	0·02			
A99 (meas.)	51·19	4·05	12·52	13·51	0·19	5·07	9·14	2·69	0·90	0·47	99·74		
SD ($n=4$)	0·09	0·04	0·08	0·09	0·00	0·05	0·06	0·03	0·01	0·03			
In-house MORB standards													
2392-9													
(accepted values)	50·04	1·31	15·48	9·38	0·18	8·50	12·15	2·56	0·09	0·13	99·81		
Meas. (mean, $n=7$)	50·05	1·28	15·48	9·25	0·16	8·56	12·15	2·63	0·11	0·12	99·79		
$\pm 2\sigma$	0·25	0·02	0·18	0·09	0·02	0·20	0·16	0·03	0·00	0·01			
JdF-D2													
(accepted values)	50·80	1·89	13·80	12·17	0·22	6·83	10·80	2·77	0·22	0·23	99·73		
Meas. (mean, $n=24$)	50·81	1·89	13·81	12·13	0·22	6·86	10·81	2·77	0·21	0·23	99·74		
$\pm 2\sigma$	0·27	0·06	0·12	0·26	0·01	0·15	0·22	0·06	0·02	0·01			

Major elements were analyzed on polished glass chips at the USGS Microbeam Laboratory in Denver, CO using a JEOL 8900 electron microprobe. Analysis of 7–10 separate points (including spots on separate chips of the same sample) were averaged for each sample and then normalized and corrected for instrument drift based on the established values for in-house standards JdF-D2 (Reynolds, 1995) and ALV2392-9 (Sims *et al.*, 2002). Accuracy was assessed by repeated measurements of Smithsonian/USGS standards VG-A99 and USNM-113716 and comparison with X-ray fluorescence (Jarosewich *et al.*, 1979) and electron microprobe (Thornber *et al.*, 2002) analyses. It should be noted that all Fe^{2+} as measured by the electron microprobe is reported as FeO^T.

Table 3: Trace-element compositions of 9°30′N and 9°50′N EPR off-axis MORB glasses (ppm) as measured by solution ICP-MS

Sample	Rb	Ba	Th	U	Nb	Ta	Pb	Sr	Zr	Hf	Y	La	Ce	Pr	Nd	Sm	Eu	Dy	Ho	Yb	Lu
9°50′N EPR																					
2697-1	1·9	22·2	0·25	0·09	3·55	0·23	0·36	120	78	1·96	23·0	3·60	10·4	1·66	8·11	2·57	0·99	3·88	0·83	2·30	0·35
2697-9	0·68	6·46	0·11	0·05	1·57	0·12	0·35	107	86	2·20	29·4	2·88	9·5	1·66	8·68	2·96	1·12	4·79	1·05	2·93	0·44
9°30′N EPR																					
2489-3	5·8	68·5	0·70	0·24	9·52	0·59	0·96	156	150	3·79	39·5	8·19	21·2	3·17	15·98	4·71	1·57	6·44	1·42	3·96	0·59
2489-4a	6·1	71·0	0·72	0·24	9·99	0·61	0·90	163	160	3·91	42·3	8·51	22·0	3·30	16·41	4·86	1·64	6·71	1·47	4·08	0·61
2489-5	5·8	67·6	0·69	0·23	9·54	0·58	0·85	156	150	3·72	39·7	8·18	21·1	3·10	15·69	4·71	1·58	6·37	1·42	3·92	0·58
2489-12	2·2	22·9	0·31	0·12	4·78	0·32	0·60	135	143	3·60	43·6	5·99	17·7	2·82	15·05	4·75	1·61	6·95	1·57	4·31	0·63
2700-7	4·3	53·8	0·52	0·17	7·20	0·45	0·68	142	127	3·21	35·2	6·63	17·5	2·67	13·57	4·16	1·42	5·78	1·28	3·54	0·53
2701-11a	4·3	53·7	0·52	0·17	7·31	0·45	0·70	146	128	3·16	35·9	6·59	17·4	2·64	13·51	4·12	1·42	5·71	1·27	3·53	0·52
2702-1	3·7	46·5	0·43	0·15	6·19	0·39	0·64	142	120	3·00	34·5	5·90	15·9	2·49	12·74	3·93	1·36	5·57	1·23	3·39	0·50
2703-1	7·8	103	0·97	0·32	14·8	0·88	1·05	260	154	3·70	35·7	11·23	26·6	3·71	17·88	4·87	1·64	5·89	1·28	3·48	0·51
2703-2	1·1	10·2	0·17	0·07	2·62	0·20	0·60	116	117	3·05	38·6	4·25	13·4	2·27	12·13	4·06	1·42	6·21	1·40	3·89	0·58
2703-3	1·2	11·6	0·17	0·07	2·56	0·19	0·62	116	113	2·91	36·5	4·05	12·8	2·17	11·58	3·85	1·34	5·88	1·31	3·66	0·54
2706-1	1·0	9·68	0·16	0·07	2·50	0·18	0·60	120	113	2·90	37·1	4·03	12·9	2·17	11·52	3·83	1·36	5·87	1·32	3·71	0·55
2706-5	1·3	11·6	0·20	0·09	3·25	0·23	0·71	110	141	3·67	46·9	4·91	15·4	2·60	14·20	4·75	1·58	7·28	1·66	4·70	0·68
2706-7	0·56	5·18	0·09	0·04	1·24	0·11	0·71	111	84	2·18	28·6	2·78	9·37	1·66	8·66	2·95	1·12	4·71	1·02	2·91	0·43
Standards																					
BHVO-1	9·2	135	1·25	0·43	19·1	1·20	2·41	402	172	4·36	26·8	15·1	36·3	5·04	24·57	6·06	1·91	5·23	0·99	2·07	0·30
Ref. values[1]	9·35	134	1·22	0·41	18·9	1·22	2·2	406	172	4·48	24·4	15·5	39·4	5·53	24·7	6·17	2·11	5·36	0·97	2·07	0·27
AGV-1 (mean, $n=21$)	67·2	1221	6·44	1·94	14·7	0·90	36·5	659	226	5·11	20·2	39·0	69·0	8·1	32·3	6·00	1·67	3·60	0·68	1·69	0·26
SD (2σ)	1·6	70	0·26	0·10	0·6	0·08	2·74	15·0	8·4	0·36	1·8	3·8	6·2	0·8	3·6	0·64	0·08	0·18	0·04	0·08	0·02
Ref. values[2]	66·6	1200	6·4	1·93	14·6	0·87	37·4	660	231	5·1	19	38·2	67·6	8·3	31·7	5·72	1·58	3·55	0·68	1·63	0·24

Samples were analyzed for trace elements at the University of Florida by ICP-MS using a Thermo Finnigan Element II. The analyses were performed in medium resolution with Re and Rh used as internal standards to correct for instrumental drift and matrix effects. Concentrations were calculated by external calibration using a combination of USGS (BHVO-1) and in-house (ENDV, an Endeavor Ridge MORB standard from the Geological Survey of Canada, Ottawa) rock standards. Measurement of BHVO-1 and repeated chemical analyses of USGS standard AGV-1 were used to evaluate in-run and long-term accuracy of the measurements; repeated runs of ENDV and a second in-house MORB standard (ALV2392-9) were used to assess instrumental drift and the precision of the measurements. Precision (2σ) was found to be better than ±5% for the REE, Ba, Hf, Nb, Rb, Sr, Th, Y and Zr, and better than ±9% for Pb, Ta and U.
[1]Reference values from Chazey *et al*. (2003).
[2]Reference values from GeoReM, 9/8/2010, Jochum *et al*. (2005).

Lu/Hf that are suspiciously low [mean off-axis sample Lu/Hf = 0·186 ± 0·021 (1σ, $n=14$), 3·08 relative %], especially when considering the exceptional compositional similarities otherwise characterizing these off-axis samples as compared with axial samples reported by Sims *et al*. (2002) [mean axial sample Lu/Hf = 0·211 ± 0·006 (1σ, $n=14$), 11·2 relative %]. Thus, we reanalyzed 12 of the 14 off-axis samples reported by Sims *et al*. (2003), as well as seven of the 19 axial samples reported by Sims *et al*. (2002) (similarly compiled from data from the GSC), for a selection of REE and incompatible trace elements. These data are reported in Electronic Appendix EA-1 (available at http://www.petrology.oxfordjournals.org). Samples were measured at the University of Florida (UF) using a Thermo Finnigan Element2 ICP-MS system, as were off-axis lavas reported in this study, and the analytical details are the same as described in the footnotes to Table 3.

The most striking feature of the newly determined UF data (inclusive of both axial and off-axis samples) is that Lu/Hf ratios calculated from the Lu and Hf abundances are nearly an order of magnitude less variable than Lu/Hf ratios determined from GSC data (i.e. for UF measurements, Lu/Hf = 0·192 ± 0·003 (1σ, $n=19$), or 1·7 relative %; for GSC measurements, Lu/Hf = 0·191 ± 0·02 (1σ,

Table 4: Sr, Nd, Hf, and Pb isotopic compositions of 9°30′N and 9°50′N off-axis samples

Sample	$^{87}Sr/^{86}Sr$	$^{143}Nd/^{144}Nd$	ε_{Nd}	$^{176}Hf/^{177}Hf$	ε_{Hf}	$^{208}Pb/^{204}Pb$	$^{207}Pb/^{204}Pb$	$^{206}Pb/^{204}Pb$	$^{208}Pb/^{206}Pb$
9°50′N EPR									
2697-1	0·702575	0·513151	10·0	0·283185	14·6	37·6898	15·4722	18·3378	2·0553
2697-9	0·702478	0·513160	10·2	0·283190	14·8	37·6394	15·4685	18·2301	2·0647
9°30′N EPR									
2489-3	0·702625	0·513086	8·7	0·283129	12·6	37·5729	15·4892	18·1786	2·0669
2489-4a	0·702860	0·513074	8·5	0·283130	12·7	37·5722	15·4890	18·1782	2·0669
2489-5	0·702760	0·513083	8·7	0·283129	12·6	37·5879	15·4904	18·1789	2·0677
2489-12	0·702498	0·513137	9·7	0·283174	14·2	37·6466	15·4696	18·2442	2·0635
2700-7	0·702478	0·513089	8·8	0·283122	12·4	37·5877	15·4853	18·1897	2·0664
2701-1	0·702678	0·513092	8·9	0·283127	12·6	37·8961	15·5061	18·4589	2·0530
2701-11a	0·702812	0·513090	8·8	0·283127	12·6	37·5754	15·4816	18·1860	2·0662
2702-1	0·702615	0·513104	9·1	0·283129	12·6	37·6047	15·4849	18·2006	2·0661
2703-1	0·702769	0·513043	7·9	0·283074	10·7	37·9965	15·5236	18·5743	2·0456
2703-2	0·702504	0·513153	10·0	0·283156	13·6	37·6656	15·4674	18·2547	2·0633
2703-3	0·702487	0·513152	10·0	0·283156	13·6	37·6651	15·4698	18·2456	2·0643
2706-1	0·702617	0·513144	9·9	0·283160	13·7	37·6820	15·4715	18·2600	2·0636
2706-5	0·702609	0·513155	10·1	0·283158	13·7	37·6514	15·4688	18·2422	2·0640
2706-7	0·702503	0·513157	10·1	0·283164	13·9	37·6781	15·4699	18·2408	2·0656
2706-7 (replicate)				0·283169	14·0				

All Sr, Nd, and Pb isotopic analyses were conducted at WHOI using a ThermoFinnigan Neptune MC-ICP-MS. Sr and Nd analyses have internal precision of 5–10 ppm. After adjusting to 0·71024 (NBS SRM 987) and 0·511847 (La Jolla Nd Standard), for Sr and Nd, respectively, external precision is estimated at 15–30 ppm. Sr and Nd whole chemistry blanks are 500–600 pg and 200 pg, respectively. ε_{Nd} values were calculated using $(^{143}Nd/^{144}Nd)_{CHUR(O)} = 0{\cdot}512638$. Measurements of $^{208}Pb/^{204}Pb$, $^{207}Pb/^{204}Pb$, and $^{206}Pb/^{204}Pb$ have estimated internal precisions of 15–30 ppm and external precisions of 150–200 ppm (2σ). SRM 997 Tl was used as an internal standard, and measurements were then normalized to NBS 981 using the values of Todt *et al.* (1996). Pb blanks are 120–150 pg. Further details have been given by Hart *et al.* (2004) and Hart & Blusztajn (2006). All Hf isotopic analyses were conducted at ENS Lyon by MC-ICP-MS using the VG Plasma 54 (Blichert-Toft *et al.*, 1997). Measured isotope ratios were normalized for mass fractionation to $^{179}Hf/^{177}Hf = 0{\cdot}7325$ using an exponential law. External analytical uncertainties of $<\pm 30$ ppm for Hf isotopic measurements were estimated from repeated runs of the JMC-475 Hf standard, which gave $0{\cdot}282160 \pm 0{\cdot}000010$ during the course of this study. In-run analytical errors were half that (i.e. $<\pm$ 0·000005). Hf blanks were <20 pg. ε_{Hf} values were calculated using $(^{179}Hf/^{177}Hf)^{CHUR(0)} = 0{\cdot}282772$ (Blichert-Toft & Albarède, 1997). Nd isotopic compositions for axial and 9°50′N off-axis lavas, as well as Siqueiros lavas reported by Sims *et al.* (2002, 2003) were measured at UC Berkeley. However, in 1994–1995, drift in the Nd isotopic measurements by the VG Sector 54 multi-collector mass spectrometer began occurring. This drift became apparent around 2003, and measurements made during that time span, including the Sims *et al.* (2002, 2003) data, were affected. We have applied the necessary corrections to these measurements, and the corrected values are reported in Electronic Appendix EA-2. Details of this shift have been documented by Bryce *et al.* (2005). As previously noted, Nd isotopic measurements for this study were conducted solely at WHOI and are unaffected by this drift.

$n = 19$), or 10·7 relative %). The UF Lu/Hf data for axial samples and off-axis samples alone have average $Lu/Hf = 0{\cdot}190 \pm 0{\cdot}004$ (1σ, $n = 7$) and average $Lu/Hf = 0{\cdot}193 \pm 0{\cdot}003$ (1σ, $n = 12$), respectively. Thus, UF Lu/Hf data are generally lower for axial samples (Sims *et al.*, 2002) and higher for off-axis samples (Sims *et al.*, 2003) than the GSC data, bringing the dataset as a whole to a nearly common value of $\sim 0{\cdot}192 \pm 0{\cdot}003$. In terms of single Lu and Hf sample abundances, there does not appear to be any systematic offset between the GSC measurements and the UF measurements. As a group, UF measurements on axial samples are on average ~6·3% higher for Hf and 5·5% lower for Lu. UF measurements for off-axis samples are on average ~8·7% lower for Hf and ~6·6% lower for Lu. Although it appears there is no simple correction that can be made to the GSC data, Lu and Hf measurements at UF appear to be more coherent and precise, resulting in a closer match in Lu/Hf for both axial and off-axis EPR samples.

With regard to U-series analyses, we are cautious of $(^{226}Ra/^{230}Th)$ for three E-MORB samples (2700-7, 2701-11a, and 2702-1) with large analytical uncertainties of

Table 5: ($^{230}Th/^{232}Th$), ($^{230}Th/^{238}U$), ($^{226}Ra/^{230}Th$), ($^{234}U/^{238}U$), and U, Th, and ^{226}Ra concentrations of 9°30′N and 9°50′N EPR off-axis samples

Sample	[Th] (ppm)[1]	[U] (ppm)[1]	Th/U	($^{238}U/^{232}Th$)[2]	($^{230}Th/^{232}Th$)[3]	($^{230}Th/^{238}U$)[3]	[Ra] (fg g^{-1})[4]	($^{226}Ra/^{230}Th$)[4]	($^{234}U/^{238}U$)[5]
9°50′N EPR									
2697-1 (1)	0·239	0·081	2·935	1·033			54·8	1·65	1·000
2697-1 (2)[6]	0·235	0·082	2·855	1·062	1·200	1·129	50·5	1·62	1·003
2697-1 (av.)	0·237	0·082	2·895	1·048	1·200	1·129	52·6	1·63	1·001
2697-9	0·100	0·043	2·329	1·303	1·386	1·064	21·1	1·37	1·003
9°30′N EPR									
2489-3 (1)	0·661	0·221	2·998	1·012			80·0	0·97	1·002
2489-3 (2)[6]	0·656	0·222	2·958	1·025	1·130	1·102	81·2	0·98	1·003
2489-3 (av.)	0·659	0·222	2·978	1·019	1·130	1·102	80·6	0·98	1·002
2489-4a (1)	0·662	0·224	2·960	1·025			81·0	0·99	1·002
2489-4a (2)[6]	0·654	0·227	2·880	1·054	1·128	1·071	84·0	1·02	1·003
2489-4a (av.)	0·658	0·226	2·920	1·040	1·128	1·071	82·5	1·01	1·002
2489-12	0·290	0·106	2·734	1·110	1·259	1·134			1·003
2700-7	0·487	0·161	3·027	1·002	1·184	1·182	68·2	1·06	1·002
2701-1	0·488	0·165	2·963	1·024	1·101	1·075			1·006
2701-11a	0·488	0·173	2·817	1·077	1·191	1·106	69·4	1·08	1·004
2702-1	0·412	0·139	2·959	1·025	1·229	1·198	59·8	1·06	1·002
2703-2	0·166	0·070	2·365	1·283	1·352	1·054	25·3	1·02	1·003
2703-3	0·171	0·068	2·511	1·208	1·369	1·133	26·8	1·03	1·000
2706-1	0·159	0·066	2·426	1·251	1·377	1·101	24·9	1·02	1·006
2706-5	0·197	0·081	2·442	1·242	1·367	1·100	28·7	0·96	1·003
2706-7	0·085	0·037	2·298	1·320	1·400	1·061	20·1	1·52	1·001
Standards									
TML meas. av.[7]	30·51(2)	10·80(2)	2·828(2)	1·073(2)	1·079(5)	0·998(5)	3688(4)	1·01(4)	1·002(1)
TML accepted[8]	30·50	10·79	2·827	1·073	1·070	0·998	3604(6)	0·99(6)	1·001
AThO meas. av.[7]	7·52(1)	2·26(1)	3·322(1)	0·913(1)	1·023(2)	1·119(2)	848(2)	0·99(2)	1·001(1)
AThO accepted[8]	7·44	2·26	3·292	0·920	1·015	1·104	844(3)	1·00(3)	1·002

[1][U] and [Th] were measured by ID-ICP-MS using the Thermo Finnigan Element system. Measurement errors (2σ) for [U] and [Th] are <2·2% and <1·6%, respectively.
[2]() denotes activity; $\lambda_{238} = 1{\cdot}551 \times 10^{-10}$ a^{-1}; $\lambda_{232} = 4{\cdot}948 \times 10^{-11}$ a^{-1}; ($^{238}U/^{232}Th$) errors (2σ) range from 1·9% to 4·4% and do not include uncertainties in λ_{238} (0·07%) or λ_{232} (0·5%).
[3]Th isotopic compositions measured by MC-ICP-MS using the Thermo Finnigan Neptune system at WHOI (Ball *et al.*, 2008; Sims *et al.*, 2008*b*); activity ratios were calculated using $\lambda_{230} = 9{\cdot}195 \times 10^{-6}$ a^{-1} and $\lambda_{232} = 4{\cdot}948 \times 10^{-11}$ a^{-1}; errors (2SE) range from 0·16 to 0·54% and do not include uncertainties in λ_{230} (0·4%) or λ_{232} (0·5%).
[4](^{226}Ra) measured by isotope dilution MC-ICP-MS using the Thermo Finnigan Neptune system at WHOI after Sims *et al.* (2008*a*); $\lambda_{226} = 4{\cdot}331 \times 10^{-4}$ a^{-1}; measurement errors (2σ) range from 1·9 to 3·5% and do not include uncertainties in λ_{226} (0·4%) or λ_{230}. For all samples accuracy is limited by uncertainties (2σ; 1·5%) on the NBS ^{226}Ra standard used to calibrate the ^{228}Ra spike.
[5]($^{234}U/^{238}U$) measured by MC-ICP-MS using the Thermo Finnigan Neptune system at WHOI; $\lambda_{234} = 2{\cdot}823 \times 10^{-6}$ a^{-1}, errors (2σ) <1·0%; for these samples ($^{234}U/^{238}U$) = 1 within error, using an equilibrium ($^{234}U/^{238}U$) of 54·48 ppm for U010 (Richter & Goldberg, 2003). NBS 960 was first bracketed by standard U010 to cross-calibrate U010. U010 was then used as a bracketing standard for all sample measurements to determine mass bias.
[6]Duplicate measurements represent dissolution of separate glass splits; glass samples were leached on the ship in either distilled water or 6N HCl for 15 min, depending on the cruise. In the laboratory the samples were hand-picked under a microscope, then ultrasonically leached in sequential treatments of 0·1N HCl plus 2% H_2O_2 (15 min), deionized water (twice, each time for 15 min), 0·1N oxalic acid plus 2% H_2O_2, and deionized water (twice, each time for 15 min). Samples were then hand-picked by microscope for a second time and then lightly leached in the clean lab in 0·1N HCl plus 2% H_2O_2 (15 min) using ultrapure reagents. Sample splits (<1–3 g) were then dissolved, aliquoted and spiked, and then U, Th, and Ra were separated using chemical techniques outlined by Sims *et al.* (2008*a*, 2008*b*).
[7]Numbers in parentheses indicate the number of replicate measurements used to calculate the average.
[8]Accepted values for [U], [Th], $^{238}U/^{232}Th$, ($^{230}Th/^{232}Th$), ($^{230}Th/^{238}U$), and ($^{234}U/^{238}U$) are from Sims *et al.* (2008*b*). Both AThO and TML are equilibrium standards with respect to ($^{226}Ra/^{230}Th$), but for analytical comparison we show the average of results from Sims *et al.* (2008*a*), including the number of runs reported in that study, which we report in parentheses.

~6–8% owing to an insufficient amount of sample being available for precise isotopic analysis, large backgrounds in the relevant range of the mass spectra, and the lack of replicate analyses because of the aforementioned sample size limitations. These samples have slight ^{226}Ra excesses of 1·06, 1·08, and 1·06, respectively. Video observations show sediment cover similar to that seen for samples 2489-3 and 2489-4a, which have replicated measurements of ($^{226}Ra/^{230}Th$) that are all in equilibrium within analytical uncertainties (2489-3: 0·97, 0·98; 2489-4a: 0·99, 1·02; Table 5). Thus, we interpret these three samples as being in secular equilibrium, but with large measurement uncertainties (~<8%), although we cannot rule out the possibility that their small ^{226}Ra excesses are real. Regardless of whether these samples have small ^{226}Ra excesses or are in secular equilibrium, the main conclusions of this study are not affected.

RESULTS

Major elements

Major element concentrations for the off-axis samples of this study are reported in Table 2. They show a wide range of compositions, with, for example, K/Ti ranging from 5·5 to 25·1 and molar Mg-number [Mg/(Mg + Fe)] ranging from 0·51 to 0·62 (Fig. 2a). The off-axis N-MORB from 9°30′N span the previously reported range in Mg-number for 9°50′N off-axis samples and have relatively constant K/Ti. However, the off-axis samples, particularly those in the 9°30′N area, have more variable and lower Mg-number (<0·55) than the correlative axial samples. Compared with axial N-MORB samples, the off-axis E-MORB have lower and less variable Mg-number and higher and more variable K/Ti. Off-axis E-MORB from 9°30′N EPR exhibit increasing K/Ti with decreasing Mg-number. Additionally, K/Ti in E-MORB from 9°30′N EPR is negatively correlated with $Fe_{8·0}$ and CaO/Al_2O_3 (Fig. 2b and c) and positively correlated with $Na_{8·0}$ [Fig. 2d; $Fe_{8·0}$ and $Na_{8·0}$ were calculated by the method of Klein & Langmuir (1987) using a linear regression of MgO vs FeO and Na_2O for 9–10°N EPR samples from this study, axial samples from Sims *et al.* (2002), and off-axis samples from Sims *et al.* (2003)]. E-MORB trend towards lower $Fe_{8·0}$ (8·96–9·70) and CaO/Al_2O_3 (0·71–0·82), yet have similar $Na_{8·0}$ (2·60–2·90) as compared with N-MORB ($Fe_{8·0} = 9·49–10·50$; $CaO/Al_2O_3 = 0·78–0·85$, $Na_{8·0} = 2·57–2·86$).

Trace elements

Trace element abundances are reported in Table 3. Primitive mantle-normalized abundances of incompatible elements for off-axis N-MORB are similar to those in axial or previously reported off-axis samples (Fig. 3; see Sims *et al.*, 2002, 2003). Compared with N-MORB, off-axis E-MORB have higher abundances of the most incompatible elements (Rb–Nd), but similar abundances of the less incompatible elements (Zr–Lu) [Fig. 3; see also Perfit *et al.* (1994) and Smith *et al.* (2001) for similar observations]. This results in a continuum of normalized trace element patterns (Fig. 3) from the most depleted N-MORB to the most enriched E-MORB. N-MORB and E-MORB all have similar middle REE (MREE) and heavy REE (HREE) abundances, but fanning light REE (LREE) patterns. Both off-axis N-MORB and off-axis E-MORB show consistent depletions of Pb and Sr relative to similarly incompatible elements (Fig. 3). Apart from differences in the abundances of the more incompatible elements (Rb–Nd), the most striking difference between the E-MORB and N-MORB patterns is that E-MORB have Ba enrichments relative to Rb and Th, whereas both off-axis and axial N-MORB have Ba depletions relative to Rb and Th (Fig. 3).

Correlations exist between incompatible element ratios for axial and off-axis lavas when including the off-axis E-MORB suite (e.g. Ce/Yb vs Th/U, Sm/Yb vs Sm/Nd; see Fig. 4a and c). Although the axial and off-axis N-MORB appear to be compositionally similar, when also taking into consideration the off-axis E-MORB suite, the total range of trace element compositions and the correlations between incompatible element ratios are strongly suggestive of mixing. Thus, in terms of trace element compositions, the 9°30′N off-axis suite shows a continuum of compositions from the most depleted N-MORB (both off-axis and axial) to the most enriched off-axis E-MORB.

Long-lived radiogenic isotopes: Sr, Nd, Hf, and Pb

Sr, Nd, Hf, and Pb isotope compositions are reported in Table 4 and shown in Figs 5 and 6. It should be noted that we also report corrected Nd isotope data from Sims *et al.* (2002, 2003) for the samples measured at UC Berkeley using the time-dependent correction outlined by Bryce *et al.* (2005) (see Electronic Appendix EA-2 for details). This post-publication correction brings the old Nd isotope measurements into line with the newer Nd isotope measurements, which is consistent with the observation that the N-MORB samples have uniform Hf isotope compositions. The analytical details are reported in the footnotes to Table 4. The data for the newly analyzed off-axis N-MORB samples overlap with the range of existing data for axial and off-axis N-MORB (Sims *et al.*, 2002, 2003; Goss *et al.*, 2010) with respect to Sr ($^{87}Sr/^{86}Sr = 0·70244–0·70257$), Nd ($\varepsilon_{Nd} = +9·9$ to $+10·6$), and Hf ($\varepsilon_{Hf} = +14·1$ to $+15·0$) isotope compositions. However, the 9°30′N off-axis N-MORB exhibit overlapping, but slightly higher $^{87}Sr/^{86}Sr$ (0·70249–0·70262) and lower ε_{Hf} ($+13·6$ to $+14·2$) and ε_{Nd} ($+9·7$ to $+10·1$) values than the 9°50′N N-MORB (Fig. 5). In comparison, off-axis E-MORB from 9°30′N have more radiogenic and variable Sr isotope compositions (0·70248–0·70286). In addition, E-MORB from

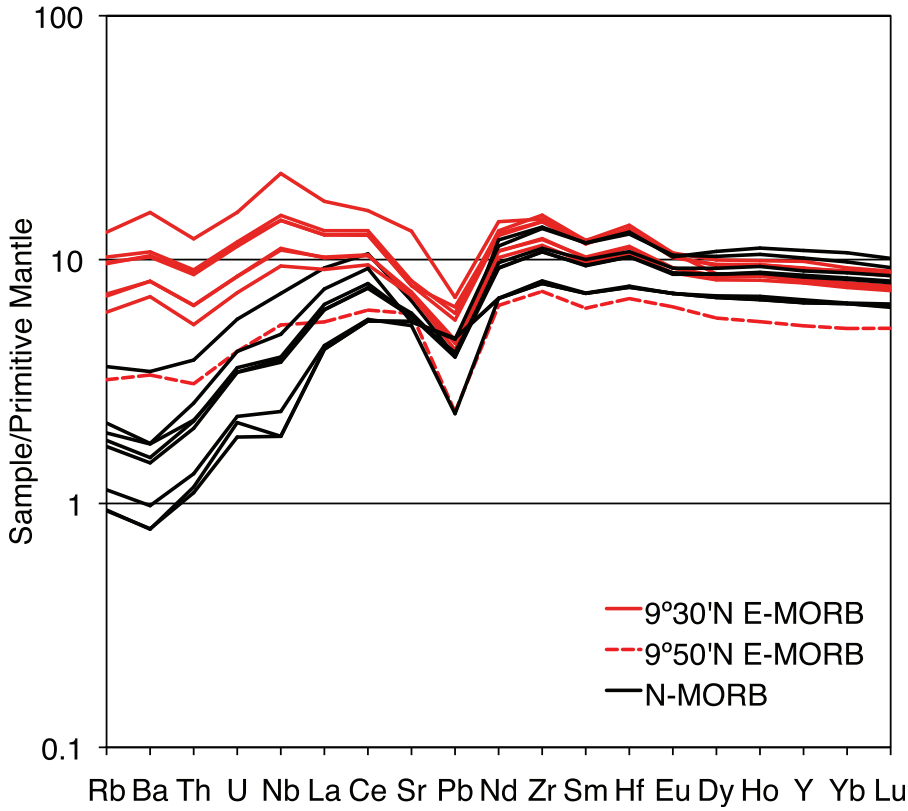

Fig. 3. Primitive mantle-normalized trace element patterns for E-MORB (9°30′N, 9°50′N) and N-MORB. Normalization constants from McDonough & Sun (1995). E-MORB and N-MORB have similar, relatively flat REE patterns. In contrast, E-MORB exhibit a wider range of highly incompatible elements and patterns consistently have positive Ba anomalies.

9°30′N have lower and more variable ε_{Nd} (+7·9 to +9·1) and ε_{Hf} values (+10·7 to +12·7) compared with the N-MORB (Fig. 5). Thus, the E-MORB from 9°30′N are demonstrably more isotopically 'enriched' with respect to their $^{87}Sr/^{86}Sr$, $^{143}Nd/^{144}Nd$, and $^{176}Hf/^{177}Hf$ isotope compositions than any of the N-MORB from the 9–10°N EPR region reported in this study and by Sims *et al.* (2002, 2003); the higher (relative to N-MORB) $^{87}Sr/^{86}Sr$ and lower (relative to N-MORB) $^{143}Nd/^{144}Nd$ and $^{176}Hf/^{177}Hf$ of these E-MORB indicate that they derive from a source with higher (relative to N-MORB) time-integrated Rb/Sr, Nd/Sm, and Hf/Lu and are thus enriched. The E-MORB from 9°50′N has Sr ($^{87}Sr/^{88}Sr = 0{\cdot}70258$), Nd ($\varepsilon_{Nd} = 10{\cdot}0$), and Hf ($\varepsilon_{Hf} = 14{\cdot}6$) isotopic compositions that are strikingly similar to N-MORB despite having a primitive mantle-normalized incompatible element abundance pattern and incompatible element ratios more similar to E-MORB (Figs 2a, 3, 4 and 7b).

Pb isotope data for the newly analyzed off-axis N-MORB from 9°50′N coincide with existing Pb isotope data for axial and off-axis N-MORB (Fig. 6; Sims *et al.*, 2002, 2003; Goss *et al.*, 2010). The range in Pb isotopic compositions for the newly measured off-axis N-MORB is narrower than that of both the off-axis and axial lavas reported by Sims *et al.* (2002, 2003). The off-axis E-MORB (sample 2697-1) from 9°50′N is compositionally indistinguishable from the N-MORB suites with respect to $^{208}Pb/^{204}Pb$ and $^{207}Pb/^{204}Pb$, but has slightly higher $^{206}Pb/^{204}Pb$ than the N-MORB suites for a given $^{208}Pb/^{204}Pb$ or $^{207}Pb/^{204}Pb$ (Fig. 7b and c). As shown by Sims *et al.* (2002, 2003), $^{208}Pb/^{204}Pb$, $^{207}Pb/^{204}Pb$, and $^{206}Pb/^{204}Pb$ for 9°17′N–10°N lavas are positively correlated. The off-axis E-MORB from 9°30′N can be subdivided into two groups in terms of Pb isotopic values: a 'more radiogenic' group and a 'less radiogenic' group (Figs 6 and 7). The 'more radiogenic' group includes two samples that have higher $^{208}Pb/^{204}Pb$, $^{207}Pb/^{204}Pb$, and $^{206}Pb/^{204}Pb$ than all of the other lavas from 9°17′N to 10°N EPR (Fig. 6). The 'less radiogenic' group has the lowest $^{208}Pb/^{204}Pb$ and $^{206}Pb/^{204}Pb$, and intermediate $^{207}Pb/^{204}Pb$ (Figs 6 and 7). However, when considering $^{208}Pb/^{206}Pb$, the 'more radiogenic' group is relatively enriched in uranogenic ^{206}Pb over thorogenic ^{208}Pb, whereas the 'less radiogenic' group has higher $^{208}Pb/^{206}Pb$ (Fig. 7).

Pb isotopes also correlate with incompatible trace element ratios and Sr, Nd, and Hf isotopes (Fig. 7).

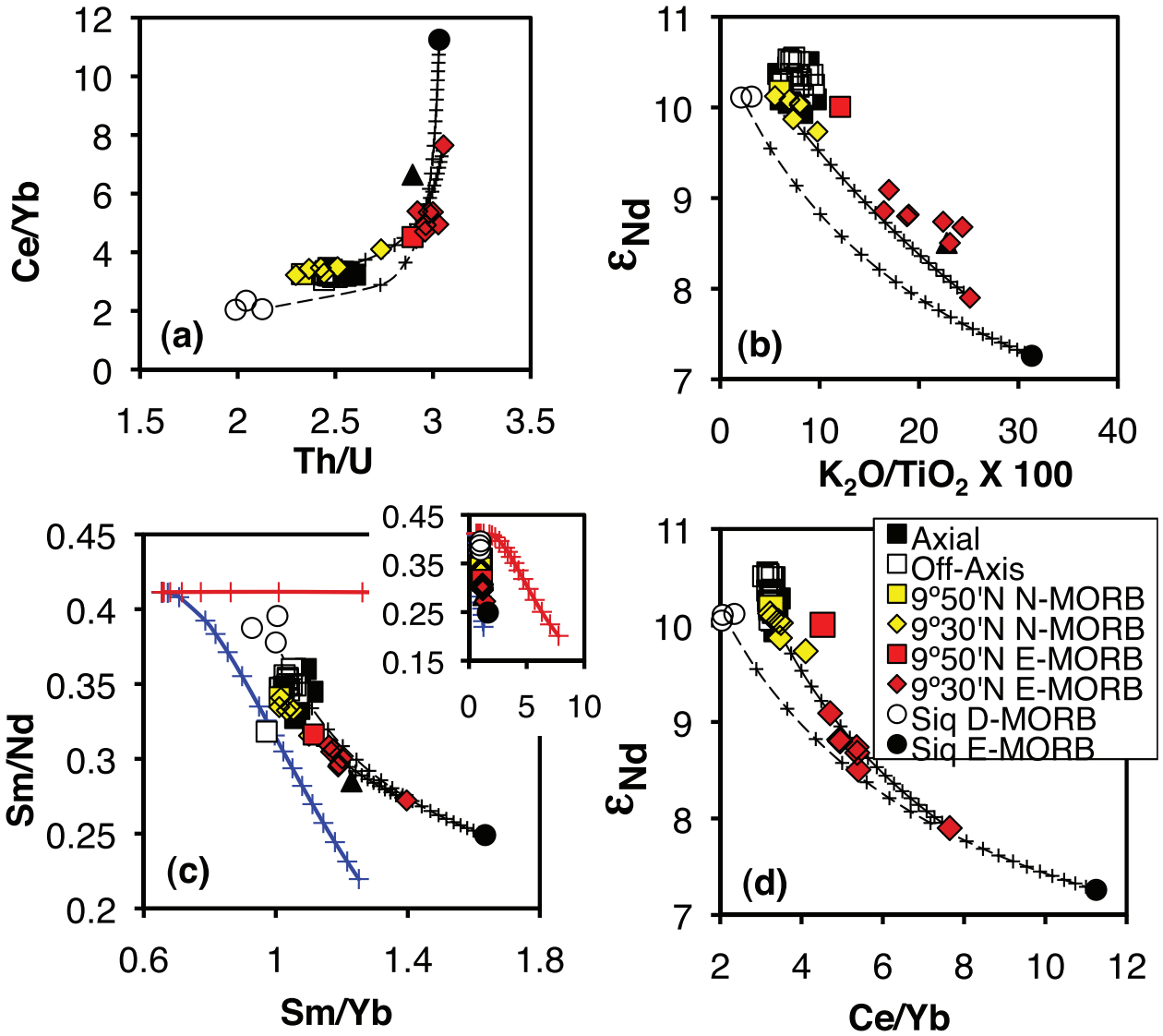

Fig. 4. Variation of (a) Th/U vs Ce/Yb, (b) $K_2O/TiO_2 \times 100$ vs ε_{Nd}, (c) Sm/Yb vs Sm/Nd, and (d) Ce/Yb vs ε_{Nd} for 9°N East Pacific Rise lavas. The dashed black line is a mixing trajectory between Siqueiros D-MORB (A2384-6) and E-MORB (A2390-5) end-members (Perfit *et al.*, 1996; Lundstrom *et al.*, 1999; Sims *et al.*, 2002). The continuous black line is a mixing trajectory between the most depleted (2706-7) and enriched (2703-1) samples from this study. Mixing increments of 5% are designated by black crosses. Also shown in (c) are modal accumulated fractional melting curves for garnet peridotite and spinel peridotite. Crosses on the melting trajectories indicate 0·1%, 1–10% in 1% increments, 12·5%, 15%, 17·5%, and 20–100% in 10% increments. (See text for details.) Inset is the same as (c) but at a different Sm/Yb scale to show the large extent of Sm/Yb fractionation by melting of garnet peridotite as compared with clinopyroxene-bearing spinel peridotite. The symbols and data sources are the same as in Fig. 2.

Finally, correlations exist between incompatible trace element ratios and Sr, Nd, and Hf isotopes for off-axis lavas from 9°30′N. Many of these correlations appear to be hyperbolic in geometry and are suggestive of two-component mixing (e.g. K/Ti vs ε_{Nd}, Ce/Yb vs ε_{Nd}; Fig. 4b and d).

U–Th–Ra disequilibria

U, Th, and ^{226}Ra concentrations and ($^{234}U/^{238}U$), ($^{230}Th/^{232}Th$), ($^{230}Th/^{238}U$), and ($^{226}Ra/^{230}Th$) for 9°30′N and 9°50′N off-axis N-MORB and E-MORB are reported in Table 5 and shown in Fig. 8.

(^{238}U)–(^{234}U)

All samples measured have ($^{234}U/^{238}U$) in equilibrium within analytical uncertainties (±0·5%) indicating that these samples have not undergone secondary alteration as a result of seawater–rock interaction following eruption. ($^{234}U/^{238}U$) is a sensitive indicator of alteration for submarine basalts, as seawater is significantly enriched in ^{234}U

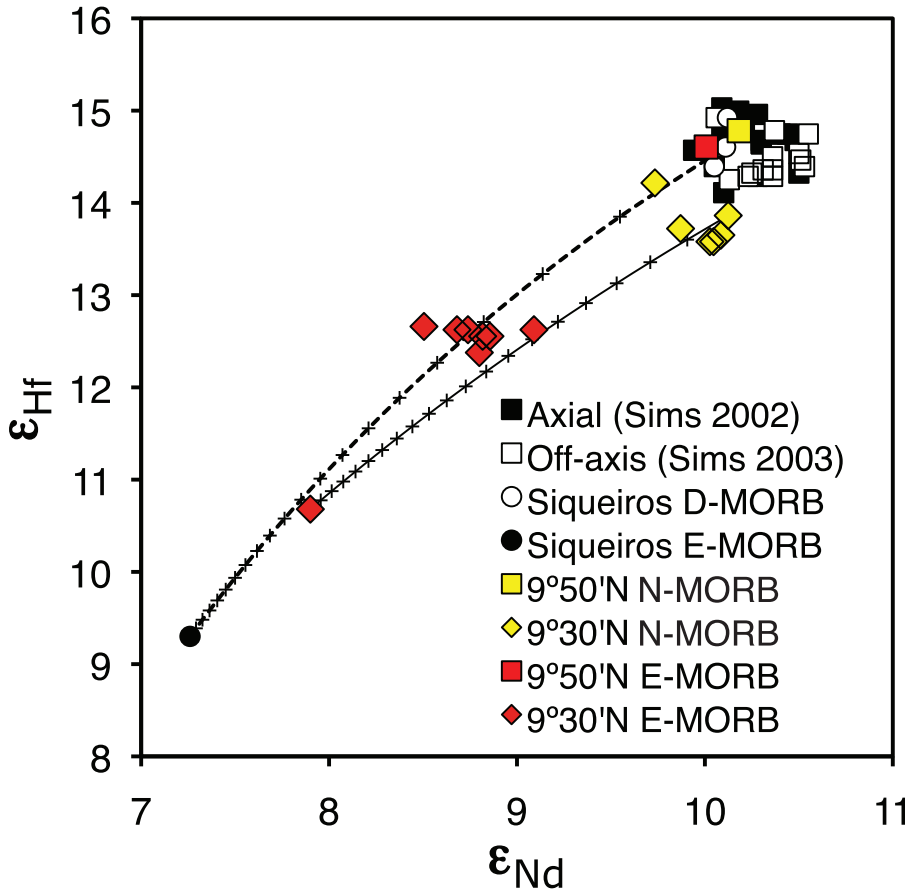

Fig. 5. ε_{Nd} vs ε_{Hf} for 9–10°N East Pacific Rise lavas. The dashed line is a binary mixing curve between Siqueiros E-MORB and D-MORB. The continuous line is a binary mixing curve between 9°30′N N-MORB (sample 2706-7) and E-MORB (sample 2703-1). Data sources and symbols are the same as in Fig. 2. Additional Siqueiros isotope data are from Sims *et al.* (2002). (See text for discussion.)

relative to ^{238}U [for seawater, $(^{234}U/^{238}U) \sim 1{\cdot}15$; Thurber, 1962; Ku *et al.*, 1977; Henderson *et al.*, 1993; Robinson *et al.*, 2004]. It should be noted that two samples (2701-1 and 2706-1) have slightly higher $(^{234}U/^{238}U)$ but are within the quoted analytical uncertainties [both samples have $(^{234}U/^{238}U) \sim 1{\cdot}006 \pm 0{\cdot}006$ (2SE)] and show no other signs of alteration (see Sims *et al.*, 2003, for a detailed discussion on alteration).

(^{238}U)–(^{230}Th)–(^{226}Ra)

All of the samples measured from both 9°30′N and 9°50′N EPR have $(^{230}Th/^{238}U) > 1$; that is, ^{230}Th excesses. Based on experimental studies, this large ^{230}Th enrichment relative to ^{238}U indicates that melting began in the presence of garnet (Beattie, 1993; LaTourrette *et al.*, 1993; Hauri *et al.*, 1994; Salters & Longhi, 1999; Landwehr *et al.*, 2001; Salters *et al.*, 2002). ^{230}Th excesses are highly variable (1·054–1·198), encompass much of the compositional range previously measured in MORB from this region, and are negatively correlated with $(^{238}U/^{232}Th)$ (see Goldstein *et al.*, 1993, 1994; Volpe & Goldstein, 1993; Lundstrom *et al.*, 1995, 1998, 1999; Sims *et al.*, 2002, 2003; Fig. 8). In addition, $(^{230}Th/^{232}Th)$ correlates with $(^{238}U/^{232}Th)$, in which E-MORB have the lowest $(^{230}Th/^{232}Th)$ (1·10–1·23) and $(^{238}U/^{232}Th)$ (1·00–1·08), N-MORB have intermediate $(^{230}Th/^{232}Th)$ (1·26–1·38) and $(^{238}U/^{232}Th)$ (1·11–1·25), and D-MORB have high $(^{230}Th/^{232}Th)$ (1·39–1·40) and $(^{238}U/^{232}Th)$ (1·30–1·32) (Fig. 8a). This correlation has previously been demonstrated and discussed by Goldstein *et al.* (1993) for 9–10°N EPR samples and extended by Lundstrom *et al.* (1999) to include E-MORB, N-MORB, and D-MORB from the Siqueiros Fracture Zone, N-MORB from the 9–10°N region, and D-MORB from the Lamont Seamounts. The samples in this study augment this trend by including samples with compositions that are transitional to the E-MORB and D-MORB end-members. Two samples have E-MORB-like $(^{230}Th/^{232}Th)$ and $(^{238}U/^{232}Th)$, but are only slightly enriched with respect to incompatible element compositions and have Sr, Nd, Hf, and Pb isotope compositions similar to N-MORB (e.g. 2697-1 and 2489-12 have Th/U = 2·94 and 2·73, respectively) (Figs 2–8). Additionally, samples 2697-9 and

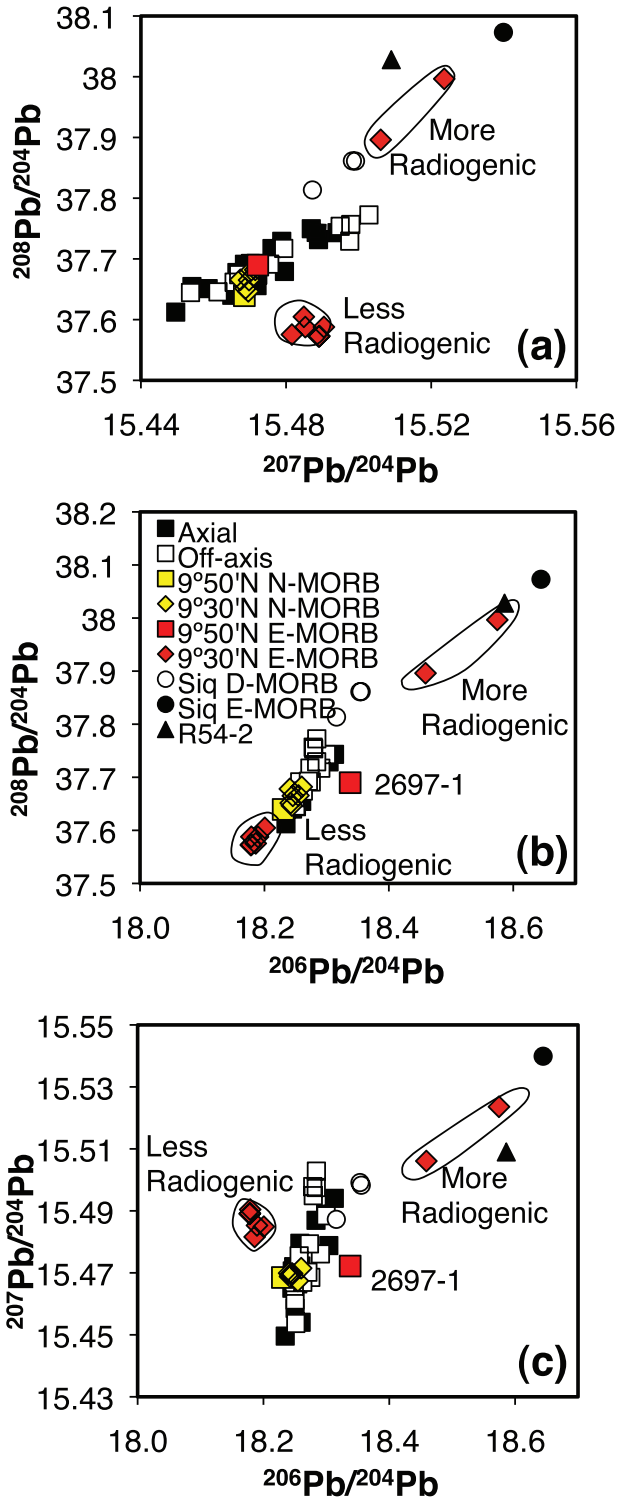

Fig. 6. (a) $^{208}Pb/^{204}Pb$ vs $^{207}Pb/^{204}Pb$, (b) $^{208}Pb/^{204}Pb$ vs $^{206}Pb/^{204}Pb$, and (c) $^{207}Pb/^{204}Pb$ vs $^{206}Pb/^{204}Pb$ for 9–10°N East Pacific Rise samples. Data sources and symbols are the same as in Figs 2 and 5. 'More radiogenic' and 'less radiogenic' off-axis E-MORB groups are marked as well as the off-axis E-MORB from 9°50′N (see text for discussion). Isotope data for sample R54-2 are from Harpp *et al.* (1990) and K. Harpp (personal communication).

2706-7 have ($^{230}Th/^{232}Th$), ($^{238}U/^{232}Th$), and incompatible element compositions that are transitional to Lamont and Siqueiros D-MORB compositions (Th/U = 2·33 and 2·30, respectively).

Three samples have measurable ($^{226}Ra/^{230}Th$) disequilibria. Sample 2697-1 [($^{226}Ra/^{230}Th$) = 1·65 ± 0·08 (2SE)] is an E-MORB (by its incompatible element composition, but not by its isotopic composition) collected from ~3·5 km off-axis at 9°50′N, and samples 2697-9 [($^{226}Ra/^{230}Th$) = 1·37 ± 0·08] from 9°50′N and 2706-7 [($^{226}Ra/^{230}Th$) = 1·52 ± 0·10)] from 9°30′N are both incompatible element-depleted N-MORB collected from <1·9 km off-axis (Fig. 8b). All other samples analyzed for ($^{226}Ra/^{230}Th$)—including all E-MORB from 9°30′N—are in equilibrium and were collected from >1·9 km off-axis. For these three samples with significant ^{226}Ra excesses [($^{226}Ra/^{230}Th$) > 1·00 ± ~0·08], ^{230}Th excesses can be assumed to be primary, as ^{230}Th undergoes only very slight decay over 8 kyr [i.e. five half-lives of ^{226}Ra—the time it takes for ($^{226}Ra/^{230}Th$) to return to equilibrium]. For the samples in equilibrium, this indicates an eruption age of at least 8 ka, and suggests that ^{230}Th excesses may need to be age-corrected to recover primary ^{230}Th disequilibria, assuming that these samples were generated and originally erupted with significant ^{226}Ra excesses. Because most samples have ($^{226}Ra/^{230}Th$) in equilibrium, they do not conform to the apparent negative correlation between ($^{226}Ra/^{230}Th$) and ($^{230}Th/^{238}U$) observed for young axial samples. The samples with ^{226}Ra excesses have low ($^{226}Ra/^{230}Th$) compared with the axial, zero-age trend (Sims *et al.*, 2002), and this is probably an effect of aging.

DISCUSSION

Correlations between chemical and isotopic variability

Based on Sr, Nd, Hf, and $^{208}Pb/^{206}Pb$ isotopic evidence, Sims *et al.* (2002) considered the axial samples from 9°17′N to 10°N EPR to be derived from a mantle source that was homogeneous over the length scale of melting. Our additional data show that off-axis E-MORB have mantle source compositions that are isotopically distinct and have a time-integrated incompatible trace element enrichment in comparison with all 9–10°N EPR N-MORB. We propose that the majority of the trends observed when including the new data for off-axis N-MORB and E-MORB in addition to previously published data for N-MORB from the 9–10°N EPR area (Sims *et al.*, 2002, 2003) result from mixing of melts derived from a heterogeneous mantle source with at least two major components that are both elementally and isotopically distinct. As mentioned above, Pb isotopes appear to be the more discriminating parameter and demonstrate mixing between each of two distinct off-axis E-MORB end-members and a

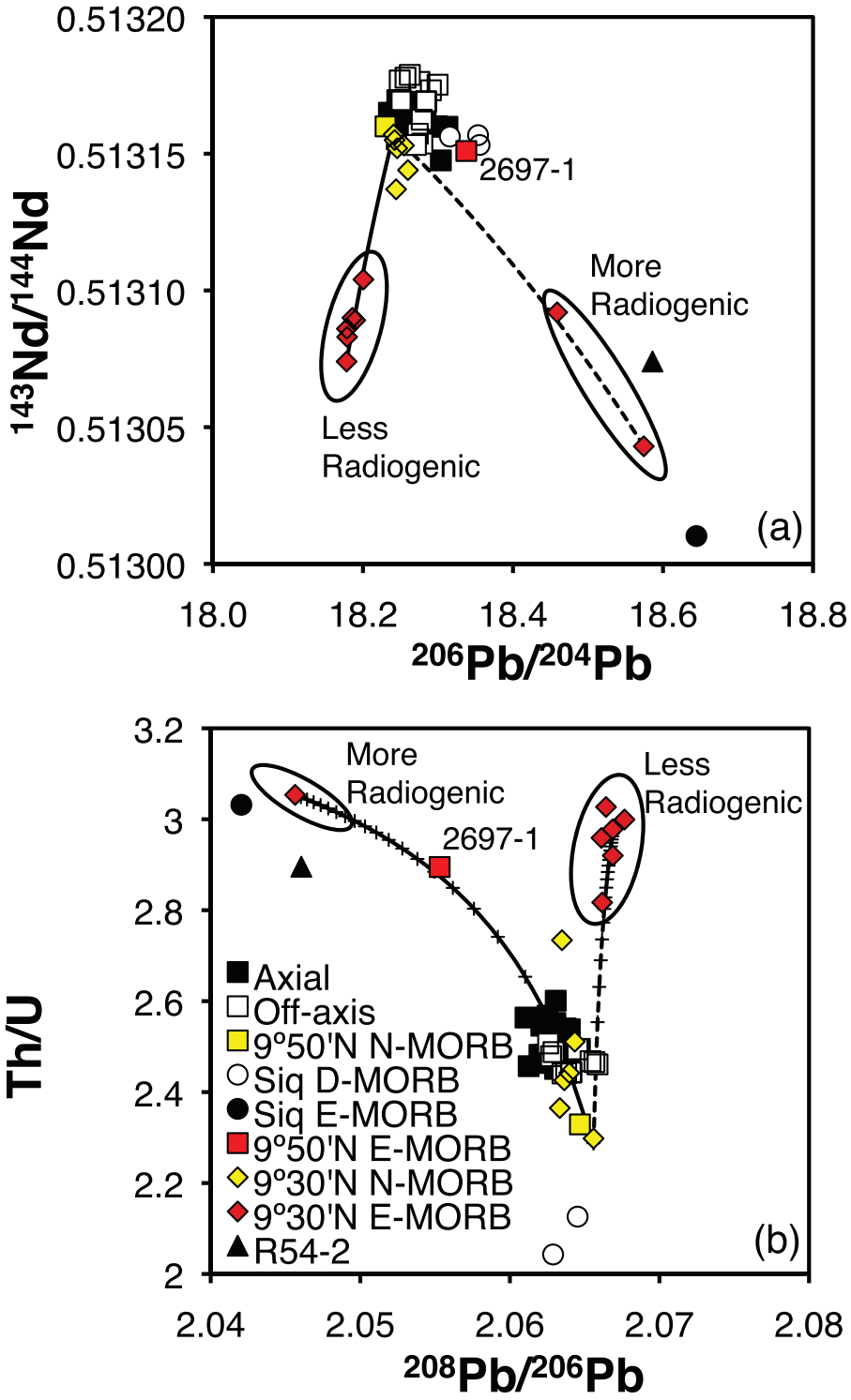

Fig. 7. Variation of (a) $^{206}Pb/^{204}Pb$ vs $^{143}Nd/^{144}Nd$ and (b) $^{208}Pb/^{206}Pb$ vs Th/U. Mixing lines are designated by a dashed line between samples 2706-7 (depleted end-member) and 2703-1 (more radiogenic E-MORB Pb end-member) and a continuous line between 2706-7 and 2489-3 (less radiogenic E-MORB Pb end-member). It should be noted that both E-MORB end-members are more isotopically enriched than N-MORB with respect to $^{143}Nd/^{144}Nd$. Data sources and symbols are the same as in Figs 2 and 5, and 6.

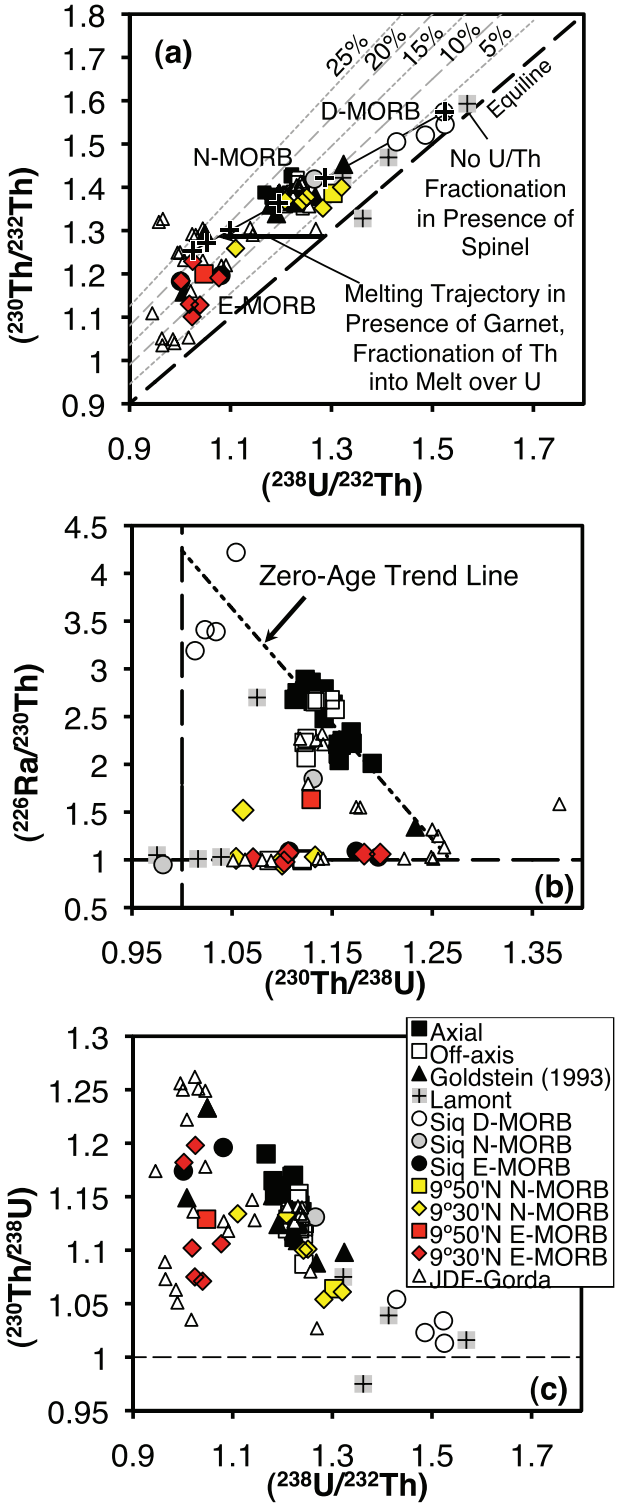

Fig. 8. (a) Variation of (^{238}U/^{232}Th) vs (^{230}Th/^{232}Th) for Pacific MORB showing the mixing relationship between D-MORB, N-MORB, and E-MORB. D-MORB have essentially negligible ^{230}Th excesses, suggesting that depleted melts were last equilibrated with spinel peridotite. In contrast, the large ^{230}Th excesses of E-MORB indicate melting in the presence of garnet. N-MORB represent mixtures of these enriched and depleted melts. The greater variability in (^{230}Th/^{232}Th) for E-MORB than for N- or D-MORB should be noted. Mixing between the Siqueiros D-MORB sample D20-2 (Lundstrom *et al.*, 1999) and the trend-line age-corrected E-MORB 2701-1 [the sample with the lowest (^{238}U/^{232}Th)] is represented by the thin black line, which is nearly identical to a regression line through samples with ^{226}Ra excesses from the 9–10°N EPR region, the Siqueiros Fracture Zone, and the Lamont Seamounts, or those samples with primary ^{230}Th excesses. This regression line is the zero-age trend-line used to calculate U–Th model ages in Table 6 and is described by the equation (^{230}Th/^{232}Th) = 0·6381 × (^{238}U/^{232}Th) + 0·6. Crosses along the mixing line represent 0%, 5%, 10%, 25%, 50%, and 100% mixing increments. ^{230}Th excesses are indicated in 5% increments by gray dashed lines. The black dashed line is the equiline. Symbols for samples from this study are the same as in Fig. 2. Also included are samples from Juan de Fuca and Gorda Ridge (Goldstein *et al.*, 1992, 1994), additional samples from the 9–10°N EPR region (Goldstein *et al.*, 1993, 1994), and samples from the Lamont Seamounts (Lundstrom *et al.*, 1999). (b) Plot of (^{230}Th/^{238}U) vs (^{226}Ra/^{230}Th) for Pacific MORB. The linear regression used to estimate the zero-age trend-line used for calculating Th–Ra model ages, indicated by a black short-dash line, includes only samples from Sims *et al.* (2002). The horizontal and vertical black dashed lines indicate equilibrium for (^{226}Ra/^{230}Th) and (^{230}Th/^{238}U), respectively. (c) Plot of (^{238}U/^{232}Th) vs (^{230}Th/^{238}U). The horizontal black dashed line indicates equilibrium for (^{230}Th/^{238}U). E-MORB samples from Juan de Fuca and Gorda Ridge that lie below the correlation have been interpreted as being older (>50–220 ka; see Goldstein *et al.*, 1992, 1993, for details).

more depleted end-member. [In this regard, we note that Sims *et al.* (2002) also could not reconcile the Pb isotopes with their assumption of source homogeneity and decided that ^{208}Pb/^{206}Pb, which was uniform in their dataset, was the most important variable for their interpretation of U-series data, as it implied constant time-integrated source ^{232}Th/^{238}U.] Despite this apparent tertiary mixing relationship with respect to Pb isotopes, we here focus on two-component mixing because this process appears sufficient to explain the entirety of the observed geochemical trends, except, puzzlingly, those of Pb. This is consistent with other studies that have shown on a global scale that U–Th, Nd, and Sr isotope systematics support a model that more closely approximates binary mixing, whereas inclusion of Pb isotopes consistently seems to call for several additional components that require fractionation of the siderophile and chalcophile element Pb relative to other lithophile elements such as U and Th (Sims & Hart, 2006). Along these lines, an interesting feature of the data, as we noted before in the Results section, is that the 'more radiogenic' group has lower ^{208}Pb/^{206}Pb, indicating a relative enrichment of uranogenic ^{206}Pb over thorogenic ^{208}Pb, whereas the 'less radiogenic' group is relatively enriched in thorogenic ^{208}Pb over uranogenic ^{206}Pb (Fig. 7).

To test the plausibility of two-component mixing, we have calculated binary mixing curves between incompatible element and long-lived radiogenic isotope compositions using the most depleted off-axis sample (2706-7) and the most enriched off-axis E-MORB (sample 2703-1)

from this study as end-member compositions. The resulting mixtures appear to reproduce the 9–10°N EPR trends reasonably well (Figs 4 and 5). We have also calculated mixing curves between Siqueiros E-MORB and D-MORB using the isotopic data from Sims *et al.* (2002) and the concentration data for the same samples published by Perfit *et al.* (1996) and Lundstrom *et al.* (1999). These represent some of the most incompatible element-enriched and -depleted samples from the first-order EPR segment between the Siqueiros and Clipperton transform faults and have been suggested to be plausible regional end-member mantle source compositions (Lundstrom *et al.*, 1999). However, the mixing curves between these Siqueiros compositions do not appear to fit the 9°30′N off-axis data nearly as well as simple mixing between depleted off-axis N-MORB and off-axis E-MORB from the 9–10°N EPR region. The isotopic variability present in the mantle source of Siqueiros transform fault lavas is similar to, but distinct from that at 9°30′N. Thus, it seems that 9°30′N and Siqueiros lavas may have slightly different mantle sources, which may reflect the length scale (or time scale) of mantle heterogeneities throughout the region. It should be noted that, for thoroughness, we have also calculated mixing relationships between the Siqueiros D-MORB sample D20-2 (Lundstrom *et al.*, 1999) and the trend-line age-corrected E-MORB sample 2701-1 (Fig. 8; see caption for details). Here again, inclusion of the Siqueiros data in mixing calculations does not reproduce the 9°30′N EPR mixing array, whereas binary mixing between end-member melt compositions from the 9–10°N samples reproduces the entire data suite fairly well.

Are E-MORB erupted on- or off-axis?

Two physical processes have been proposed to explain the geochemically enriched signatures of E-MORB melts along the EPR. In the first process, as advocated by Perfit *et al.* (1994), E-MORB melts are produced in the mantle away from the main melt zone and transported through crustal pathways outside the AMC to small, off-axis melt lenses, from which they subsequently erupt. This model can explain the off-axis occurrence of E-MORB and implies that E-MORB can be erupted off-axis only if the enriched geochemical signature is to be preserved. Perfit *et al.* (1994) also suggested that E-MORB melts may be transported through the mush zone and AMC, but they noted that the enriched signature of E-MORB melts that pass through the AMC and mush zone would be overwhelmed by the composition of the volumetrically dominant N-MORB melt. Although we cannot exclude this model, the geological evidence presented in more recent studies, as described above and discussed below, suggests that a model in which E-MORB erupt within the AST not only is equally viable but also is far simpler, and thus more likely.

The alternative scenario that has been proposed is that production of E-MORB and N-MORB occurs at different times, and that mixing of enriched and depleted melts, occurring during progressive depletion, produced the observed geochemical variations (e.g. Hekinian *et al.*, 1989; Batiza & Niu, 1992; Smith *et al.*, 2001). In other regions of the EPR, such as 11°45′N–13°N, E-MORB are known to erupt within the ridge axis (e.g. Hekinian *et al.*, 1989; Reynolds *et al.*, 1992; Castillo *et al.*, 2000). These lavas also display similar correlations between incompatible element enrichment and isotopic enrichment. At 17°30′S EPR, mantle melting processes and source characteristics have been argued to vary over the course of hundreds of years, based on the distribution of five geochemically and magnetically distinct lava sequences (Bergmanis *et al.*, 2007). We expect similar variations at 9–10°N EPR, although possibly over somewhat longer time scales, as the spreading rate is significantly slower (11 cm a^{-1} at 9–10°N vs ~14·6 cm a^{-1} at 17°S).

Yet another hypothesis proposes that E-MORB and N-MORB melts are produced concurrently and stored in a discontinuous melt lens, thereby avoiding complete melt homogenization and preserving the E-MORB composition. One would expect, in such a scenario, that periods of diminished melt production (which may occur randomly through time, even during long periods of generally high melt production) should allow for a more discontinuous melt lens with more extensively crystallized magmas, and, hence, greater preservation of E-MORB melts. During extended periods of high melt production and magma chamber replenishment, one would expect a more continuous AMC and that melts would homogenize more thoroughly. Similar types of scenarios have been suggested in other studies where E-MORB have been collected nearer the ridge axis (e.g. Reynolds *et al.*, 1992; Smith *et al.*, 2001). It is this type of scenario that we believe is best supported by the existing data and our geochemical modeling.

Because of the detailed studies conducted at 9°17′N–10°N EPR, we can readily identify relationships between spatial variations in lava chemistry and variations in lava age, which can help discriminate between the hypotheses presented above. In particular, we have excellent constraints on the extent of the neo-volcanic zone in this region from side-scan sonar imaging and magnetization profiles (e.g. Fornari *et al.*, 1998, 2004; Schouten *et al.*, 1999, 2004; Sims *et al.*, 2003; Soule *et al.*, 2005, 2009; Escartin *et al.*, 2007), qualitative age constraints on lava flows outside the axial summit trough from submersible observations (Haymon *et al.*, 1993; Sims *et al.*, 2003; Soule *et al.*, 2007), and quantitative age constraints obtained from paleointensity (Bowles *et al.*, 2006) and U-series analyses (e.g. Volpe & Goldstein, 1993; Goldstein *et al.*, 1994; Rubin *et al.*, 1994; Sims *et al.*, 2003).

Geological constraints

Based on observations of E-MORB collected within the axis in other MOR locations, particularly in the 12–13°N region (e.g. Langmuir *et al.*, 1986; Hekinian *et al.*, 1989; Reynolds *et al.*, 1992; Niu *et al.*, 1999; Reynolds & Langmuir, 2000) and the 17°S EPR (Bergmanis *et al.*, 2007), there appears to be no justification for assuming a solely off-axis eruptive origin of 9–10°N EPR E-MORB melts. Instead, we suggest that the off-axis occurrence and distribution of E-MORB are closely tied to the volcanic processes that locally contribute to crustal construction. The focus of many past studies at 9–10°N EPR has been to understand why seismic layer 2A, interpreted as the extrusive crust, rapidly doubles in thickness within ~2 km of the AST and then maintains a constant thickness (Harding *et al.*, 1993; Christeson *et al.*, 1994, 1996; Goldstein *et al.*, 1994; Vera & Diebold, 1994; Hooft *et al.*, 1996; Schouten *et al.*, 1999; Sims *et al.*, 2003; Bowles *et al.*, 2006; Escartin *et al.*, 2007). Although many of these studies preferentially advocate for different single lava emplacement mechanisms, the most widely accepted model for volcanic accretion along the ridge axis from the 9–10°N EPR region favors a scenario in which new volcanic construction occurs dominantly by lava overflow of the AST and subsequent flow down the ridge flanks (particularly in channels and as larger flows); flows typically interact with faults and are dammed ~1–2 km off-axis, doubling the thickness of the extrusive crust (Hooft *et al.*, 1996; Schouten *et al.*, 1999; Sims *et al.*, 2003; Fornari *et al.*, 2004; Soule *et al.*, 2005; Bowles *et al.*, 2006; Escartin *et al.*, 2007). Off-axis eruptions and pillow ridges probably play a less significant role in crustal construction (see Sims *et al.*, 2003). What has become increasingly clear from these studies is that lava emplacement is not confined to the AST and that young lava flows easily extend up to ~2 km on both sides of the AST (Fig. 1). This area of young lavas has been termed the 'neo-volcanic zone', and the difference between young, 'neo-volcanic' seafloor and flanking old seafloor has been interpreted to correspond to age differences of the order of ~1–10 ka (Escartin *et al.*, 2007).

In general, E-MORB are located in areas of diminished volcanic activity, particularly near the dying western limb of the small OSC (Smith *et al.*, 2001) and east of the neo-volcanic zone in the 9°30′N region northwards to 9°36′N, with a smaller population west of the neo-volcanic region at 9°50′N (Fig. 1). Evidence of decreased fault density (Escartin *et al.*, 2007), increased lava channel density (Soule *et al.*, 2005), thicker extrusive layer volumes (Harding *et al.*, 1993; Soule *et al.*, 2005; Escartin *et al.*, 2007), decreased apparent sedimentation in side-scan sonar (Fornari *et al.*, 1998, 2004; Soule *et al.*, 2009), higher magnetic anomalies (Schouten *et al.*, 1999), and a westward offset of the AMC relative to the AST (Crawford & Webb, 2002; Escartin *et al.*, 2007; Soule *et al.*, 2005) indicate that relatively recent volcanic activity and crustal accretion have been preferentially distributed to the west side of the axis at 9°30′N, opposite the highest concentration of E-MORB. Similarly, at 9°50′N, these lines of evidence (note the AMC is offset to the east at 9°50′N) indicate that volcanism and crustal accretion are focused to the east side of the AST. Thus, given the sampling distribution of E-MORB, the geological evidence suggests that E-MORB (with the exception of R54-2, a dredged E-MORB sampled east of the small OSC at 9°37′N) are indeed older and not currently erupting within the AST, and that current exposure on the seafloor simply reflects the fact that they have not been covered by younger lava flows of axial N-MORB compositions.

Paleointensity age constraints

Bowles *et al.* (2006) reported paleointensities on ~175 samples from the 9–10°N EPR region, including nine E-MORB that were collected off-axis. Of these nine E-MORB, three are from north of the small OSC at 9°37′N, and two of these three samples have paleointensities >20 μT, whereas the third has a paleointensity of ~7·7 ± 0·2 μT (1SE). The remaining six E-MORB come from east of the AST at 9°30′N, include three of our samples, and have paleointensities <15 μT [samples 2489-3 (~13·8 ± 0·6 μT), 2489-4a (~12·4 ± 0·2 μT), and 2489-5 (14·7 ± 0·6 μT) (1SE; see Table 6)]. Paleointensity measurements on off-axis N-MORB sample 2489-12 (~6·6 ± 0·1 μT) and other lavas from the same area east of the AST at 9°30′N have the lowest paleointensities of any samples from the 9–10°N EPR region (~6–8 μT) and are most probably associated with the globally observed Laschamp excursion at ~40 ka (Bowles *et al.*, 2006). The Laschamp excursion lasted for at most a few thousand years and is the only period over the past ~100 kyr during which the paleointensity field reached such low magnitudes (see Laj *et al.*, 2000; Bowles *et al.*, 2006). Following the Laschamp excursion, paleointensities increased until they peaked about ~500–2000 years ago (< ~53 μT) and since then have been declining to the present-day value of ~36 μT. As noted above, the E-MORB also have relatively low paleointensities (<20 μT), but because of incomplete knowledge of the paleointensity field variations, Bowles *et al.* (2006) restricted their interpretation to saying that these samples are most probably more than ~20 kyr old. Given the similarity in paleointensities and major element compositions of E-MORB samples 2489-3, 2489-4a, and 2489-5, Bowles *et al.* (2006) suggested that these samples were erupted within ~100 years of each other and may even have been part of the same flow unit (here we have further shown that they are also very similar with respect to both trace element and isotopic compositions; see Tables 3 and 4). Because a large number of samples beyond ~1·74 km east of 9°30′N (the area where the majority of the E-MORB reported in this study were collected)

Table 6: Spreading rate age, U–Th and Th–Ra age limits and U–Th and Th–Ra model ages[1]

Sample	Distance from AST (km)	Age based on spreading rate (ka)	U–Th–Ra age constraints (ka)	U–Th trend-line age (ka)	Th–Ra trend-line age (ka)	Emplacement distance[2] (km)	Paleointensity constraints (ka)
9°50′N EPR							
2697-1	3·52	64·0	<8	0	2·3 ± 0·5	3·40 ± 0·03	
2697-9	1·90	34·5	<8	0	4·4 ± 0·3	1·66 ± 0·02	
9°30′N EPR							
2489-3	2·24	40·7	8–375	81 ± 26	>8	[3]	>20
2489-4a	2·64	48·0	8–375	100 ± 27	>8	[3]	>20
2489-5	3·12	56·7					>20
2489-12	4·20	76·4	<375	31 ± 11	NM	2·52 ± 0·62	~40
2700-7	3·15	57·3	8–375	29 ± 25	>8[4]	1·54 ± 1·39	
2701-1	5·00	90·9	<375	85 ± 25	NM	0·34 + 1·36/−0·34	
2701-11a	3·64	66·2	8–375	64 ± 29	>8[4]	0·10 + 1·58/−0·10	
2702-1	3·08	56·0	8–375	12 ± 26	>8[4]	2·41 ± 1·44	
2703-1	3·88	70·5					
2703-2	3·33	60·5	8–375	43 ± 16	>8	0·94 ± 0·85	
2703-3	3·00	54·5	8–375	1 ± 14	>8	2·56 ± 0·76	
2706-1	3·15	57·3	8–375	17 ± 15	>8	2·22 ± 0·85	
2706-5	1·90	34·5	8–375	20 ± 15	>8	0·79 + 0·83/−0·79	
2706-7	1·80	32·7	<8	0	3·6 ± 0·3	1·60 ± 0·02	

[1]Samples from 9°50′N are from to the west of the AST. All sample from 9°30′N are from the east of the AST. AST locations determined by Soule *et al*. (2009). Spreading determined assuming a constant half-spreading rate of 5·5 cm a^{-1}. Age constraints are based upon the presence or absence of ($^{230}Th/^{238}U$) or ($^{226}Ra/^{230}Th$) disequilibria and the half-lives of ^{226}Ra and ^{230}Th. To account for variations in ($^{238}U/^{232}Th$) and ($^{230}Th/^{232}Th$) when calculating a linear regression to estimate a U–Th zero-age trend-line, we include all data for enriched and depleted samples with ^{226}Ra excesses >1·05 from the Siqueiros Fracture Zone (Lundstrom *et al*., 1999), the Lamont Seamounts (Lundstrom *et al*., 1999), and the 9–10°N area (Volpe & Goldstein, 1993; Goldstein *et al*., 1994; Sims *et al*., 2002, 2003)—including samples from this study (2697-1, 2697-9, 2706-7) (see 'zero-age trend-line,' Fig. 9a). Hence, samples from this study with ^{226}Ra excesses are assigned U–Th model ages of zero. U–Th model ages are calculated for all samples with no ^{226}Ra excesses, even if the sample has ($^{238}U/^{232}Th$) and ($^{230}Th/^{232}Th$) disequilibria indistinguishable from zero-age lavas. Because ($^{230}Th/^{232}Th$) disequilibria decay along vertical trajectories, U–Th trend-line model ages are calculated by assuming an initial ($^{230}Th/^{232}Th$) disequilibrium along the zero-age trend-line at the sample ($^{238}U/^{232}Th$) and by determining the time needed for that initial ($^{230}Th/^{232}Th$) disequilibrium to decay to the ($^{230}Th/^{232}Th$) of the sample. Errors are estimated by accounting for model age variations owing to ±1SD of the zero-age ($^{230}Th/^{232}Th$) for either N-MORB or E-MORB samples. Thus, E-MORB sample ages will have greater errors because of the smaller number of samples and the wider range of ($^{230}Th/^{232}Th$) nearer the enriched end-member. Th–Ra minimum and maximum ages were calculated using the range of ($^{226}Ra/^{230}Th$) in the zero-age axial samples from 9°17′ to 10°N (2·01–2·89) from Sims *et al*. (2002). For Th–Ra model ages, a zero-age trend-line was extrapolated through the axial samples from Sims *et al*. (2002) (Fig. 9a). Model ages for N-MORB were calculated assuming vertical decay of ($^{226}Ra/^{230}Th$) from the Th–Ra zero-age trend-line at constant ^{230}Th excess (Sims *et al*., 2003). As with U–Th ages, errors were calculated from ±1SD from the zero-age trend-line. Because all E-MORB samples are in equilibrium within analytical uncertainties with respect to ($^{226}Ra/^{230}Th$), no Th–Ra ages were calculated for E-MORB. Paleointensity age constraints are from Bowles *et al*. (2006). NM, not measured.

[2]Emplacement distances were calculated by multiplying the difference between the age expected based on the spreading rate and the U-series model age by the spreading rate, 5·5 cm a^{-1}.

[3]Samples 2489-3 and 2489-4a have U–Th trend-line ages greater than the spreading age. (See text and Fig. 10 for details.)

[4]Samples 2700-7, 2701-11a, and 2702-1 have small ^{226}Ra excesses of 6–8%, and although these excesses may be significant, we believe that this is unlikely and that these measurements are at the edge of our measurement uncertainties. Thus, for the purposes of age constraints, we assume that these samples are in secular equilibrium (see Analytical Methods section in text for details), and model ages and emplacement distances are calculated based on this assumption.

have low paleointensities, and thus by inference eruption ages >20 ka, Bowles *et al.* (2006) further suggested that no flows were emplaced in this region for the last 20 kyr. Thus, it is very likely that both the E-MORB and N-MORB in this area have not been covered by younger flows.

U-series age constraints

^{238}U–^{230}Th and ^{230}Th–^{226}Ra disequilibria can be used to place constraints on lava eruption ages; these constraints are shown in Table 6. Both ($^{230}Th/^{238}U$) and ($^{226}Ra/^{230}Th$) return to secular equilibrium within analytical uncertainties after about five half-lives, or 375 and 8 kyr, respectively. Thus, samples with ^{226}Ra excesses erupted less than ~8 kyr ago, and samples with ($^{226}Ra/^{230}Th$) in equilibrium are older than 8 ka, assuming they were erupted with ^{226}Ra excesses. [Note that the inverse correlation between ($^{230}Th/^{238}U$) and ($^{226}Ra/^{230}Th$) predicts that E-MORB should have high ^{230}Th excesses and low ^{226}Ra excesses.] Because all samples from this study have ^{230}Th excesses, they can be assumed to be younger than ~375 ka. However, no E-MORB samples have ^{226}Ra excesses, indicating that all 9°30′N E-MORB were erupted >8 kyr ago (provided they were erupted with significant ^{226}Ra excesses). Only three samples from this study have significant ^{226}Ra excesses, indicating that their eruption occurred within the last few thousand years: an N-MORB from 9°30′N, an N-MORB from 9°50′N, and an E-MORB from 9°50′N (Fig. 8b; see Results section). It should be noted that because lavas can flow for considerable distances in this region of the EPR, the presence of a ^{226}Ra excess in a lava by itself implies nothing about its eruption location, only that it erupted within the last 8 kyr.

A trend-line model age technique has been applied to N-MORB from the 9°50′N area to provide more rigorous lava age constraints (Sims *et al.*, 2003). We extend this trend-line model age method to dating E-MORB at 9–10°N EPR. However, as explicitly outlined by Sims *et al.* (2003), calculating robust ^{238}U–^{230}Th and ^{230}Th–^{226}Ra model ages requires: (1) that primary magmatic processes generated the initial ^{238}U–^{230}Th and ^{230}Th–^{226}Ra disequilibria and that these lavas have remained a closed system; (2) that magmas have not resided for significant periods of time in a magma chamber relative to the ^{238}U, ^{230}Th, and ^{226}Ra half-lives; (3) that the mantle source between the zero-age lava and a sample of unknown age is compositionally constant; (4) that the initial extent of disequilibria in the zero-age lava and sample of unknown age is the same. These criteria were met by N-MORB samples collected off-axis at 9°50′N EPR (Sims *et al.*, 2003). However, because there is only one E-MORB sample from the 9–10°N EPR region with a ^{226}Ra excess (sample 2697-1), this is the only E-MORB from this area for which the initial ($^{230}Th/^{232}Th$) and ^{230}Th excess are also known. In turn, regressing initial ($^{230}Th/^{232}Th$) against ($^{238}U/^{232}Th$) data on an equiline diagram to generate a zero-age trend-line for purposes of ^{238}U–^{230}Th dating means that the enriched end of this trend-line is weighted only by this one sample, leaving the range of initial ^{230}Th disequilibria for E-MORB much more uncertain than that for N-MORB. Furthermore, there are no E-MORB with known zero-age ^{226}Ra excesses, and hence dating E-MORB by the ^{230}Th–^{226}Ra method is more problematic than dating N-MORB. However, we stress that this technique nevertheless is more robust than the model age techniques used by Goldstein *et al.* (1992, 1993, 1994), which used a single point to estimate the initial ^{230}Th and ^{231}Pa disequilibria for a given lava type (E-MORB vs N-MORB) despite the clear correlation between ($^{230}Th/^{232}Th$) and ($^{238}U/^{232}Th$) among young EPR lavas (see Sims *et al.*, 2003, for discussion). Lastly, we also note that the N-MORB ages from Goldstein *et al.* (1994) were used to infer young ages for nearby E-MORB lavas that in part led to the model that these EPR E-MORB were erupted off-axis (Perfit *et al.*, 1994).

Thus, more uncertainty is associated with determining model ages for E-MORB. However, given the negative correlations among ^{226}Ra excesses, ^{230}Th excesses, and ($^{238}U/^{232}Th$) for E-MORB, N-MORB and D-MORB samples from the Siqueiros Fracture Zone, the Lamont Seamounts, and 9–10°N EPR, it seems likely that the primary processes (namely, partial melting and mixing during melt transport) that generate U-series disequilibria in N-MORB are also responsible for generating disequilibria in E-MORB (Fig. 8c). Furthermore, all samples in this study have been analyzed for ($^{234}U/^{238}U$) and are in equilibrium or show no other signs of alteration, indicating that these lavas have remained unaffected by seawater alteration after eruption, and that they have most probably remained closed systems after eruption. Additionally, because long-lived radiogenic isotopic compositions, ($^{230}Th/^{232}Th$), and ($^{238}U/^{232}Th$) are all correlated owing to mixing, as described above, the zero-age trend-line also represents mixing of partial melts of isotopically distinct sources. Hence, by extrapolating the zero-age ^{238}U–^{230}Th and ^{230}Th–^{226}Ra trend-lines for axial N-MORB to include D-MORB and E-MORB, we also account for source heterogeneity [note that Sims *et al.* (2003) regressed only zero-age, axial N-MORB with uniform isotopic compositions to date off-axis N-MORB of unknown age]. We note as a caveat, however, that this is not strictly true, as the Siqueiros E-MORB are not isotopically identical to the 9–10°N E-MORB, have different U and Th abundances, and do not derive from the same mantle source as 9–10°N E-MORB; yet they heavily weigh the enriched end of the ^{238}U–^{230}Th zero-age trend-line.

Finally, a recent study of ^{210}Pb disequilibria by Rubin *et al.* (2005) limits crustal residence time at 9–10°N EPR

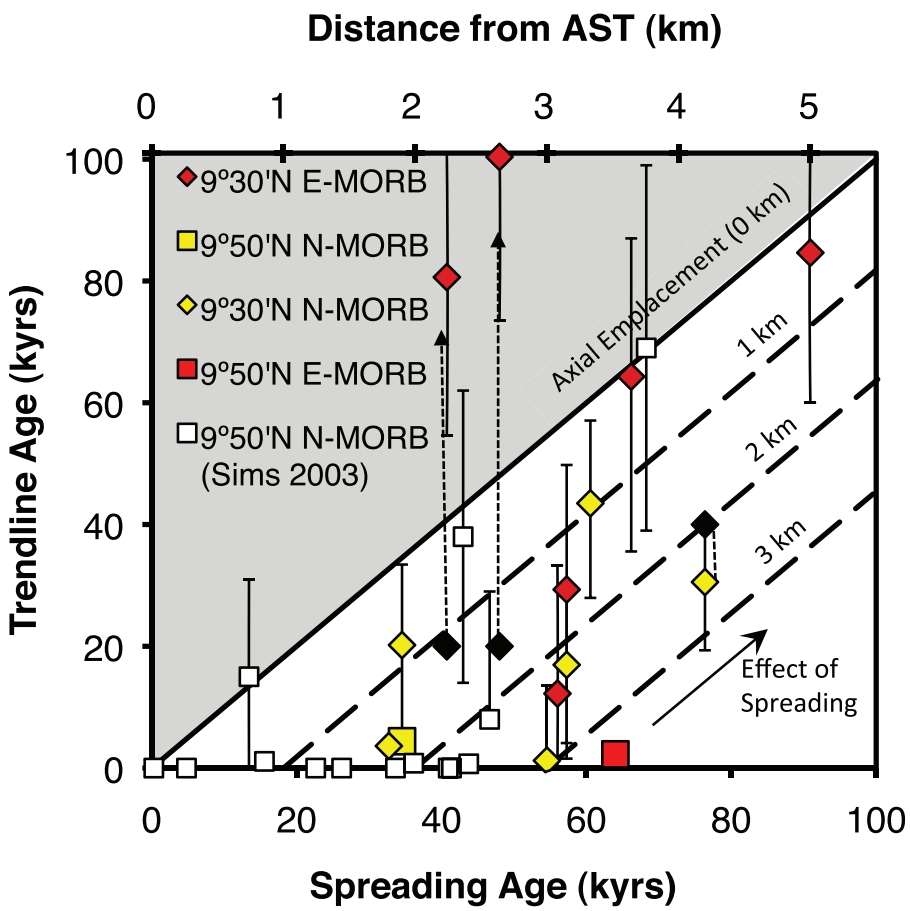

Fig. 9. Spreading age (ka) vs model age trend-line (ka) and distance from the AST (km). Spreading ages were calculated as described in Table 6. Model U–Th and Th–Ra ages are plotted using different symbols (as in Fig. 2); paleointensity age constraints (Bowles *et al.*, 2006) are plotted as black diamonds. Thin dashed (vertical) lines between black diamonds and colored symbols connect U–Th ages and paleointensity age constraints for single samples; lines with arrows indicate that the paleointensity constraint is a minimum estimate. Thick continuous and dashed lines represent the effect of variable lava emplacement distances on spreading ages. Shown are lines for lava emplacement in the axial summit trough, 1 km off-axis, 2 km off-axis, and 3 km off-axis. We interpret the trend-line age as the true sample age, whereas the spreading ages may also reflect the distance the lava was emplaced off-axis. Trend-line model ages significantly younger than the spreading ages are consistent with a significant component of off-axis volcanic accretion. Emplacement may occur via eruption within the AST and subsequent flow away from the AST or from direct emplacement owing to off-axis eruption. The gray shaded field represents lava ages older than the spreading age, a physical implausibility. It should be noted that Th–Ra model ages often provide higher resolution and significantly different age information from U–Th model ages. Error bars for Th–Ra model ages are smaller than the size of the symbol.

to less than a few hundreds of years; thus—as with N-MORB—it is unlikely that magma storage has a significant impact on the extent of ^{230}Th and ^{226}Ra disequilibria in E-MORB. Although trend-line model ages for E-MORB will not be as robust as those for N-MORB, they should still provide reasonable estimates. Better knowledge of primary (^{230}Th/^{232}Th) and (^{238}U/^{232}Th) in a larger number of E-MORB from the 9–10°N EPR region would undoubtedly allow for much more robust model age calculations. Details of the trend-line model age calculations are reported in the caption to Table 6.

^{238}U–^{230}Th trend-line model ages for both N-MORB and E-MORB are generally significantly younger than the spreading ages, which is consistent with significant crustal accretion up to ~3 km off-axis (e.g. Goldstein *et al.*, 1993; Hooft *et al.*, 1996; Schouten *et al.*, 1999; Sims *et al.*, 2003) (Fig. 9). All N-MORB (except for sample 2489-12) have (^{230}Th/^{232}Th) indistinguishable from axial N-MORB samples [(^{230}Th/^{232}Th) ~ 1·386 ± 0·038 (2σ; n = 19); Sims *et al.*, 2002] and thus may have been more recently erupted. However, four of these N-MORB samples have (^{226}Ra/^{230}Th) in equilibrium and must have erupted >8 kyr ago.

Figure 9 illustrates the relationship between trend-line age, spreading age (or distance from the AST), and the effect of off-axis emplacement on the spreading age. The ^{238}U–^{230}Th trend-line ages of these samples are younger than their expected spreading ages based on their distance

from the AST, and this indicates that lava emplacement generally occurred <3 km off-axis. The neo-volcanic zone frequently extends to ~3 km in width along the 9–10°N EPR, including on the western side of the axis at 9°30′N (Escartin *et al.*, 2007). Thus, lava distribution may have occurred via off-axis eruption or by eruption within the AST and subsequent transport to the ridge flanks—a feature now well documented in the 9°50′N area (Schouten *et al.*, 2002; Sims *et al.*, 2003; Soule *et al.*, 2005, 2009).

One of the most striking aspects of these data is that there is no systematic difference between E-MORB and N-MORB emplacement distances (and ages). Thus, there is also no reason to suspect that the mechanism of emplacement of E-MORB is different from that of N-MORB: both N-MORB and E-MORB probably erupt in the AST and flow off-axis up to several kilometers, although it is possible that a relatively small volume of N-MORB and E-MORB erupts off-axis from axis-parallel faults and fissures, and this is observed in pillow ridges (note that studied pillow ridges have been verified to be N-MORB in composition; Sims *et al.*, 2003; Hinds, 2004). It is also possible that E-MORB may be erupted as pillow mounds within the AST, and this type of lava emplacement has been documented for N-MORB near third-order segment ends (White *et al.*, 2002).

We draw attention to the fact that many of the E-MORB in this study from 9°30′N were sampled from pillow lavas in association with fault scarps. However, these E-MORB were generally sampled at the tops of outward dipping faults, and several were sampled from intact pillows midway up outward dipping fault scarps (e.g. 2701-1, 2702-1), suggesting that many of them are pillow lavas draped over volcanic growth faults (Macdonald *et al.*, 1996). Thus, an axial origin for these lavas is consistent with dive observations, remote sensing imagery, and the paleointensity and ^{238}U–^{230}Th–^{226}Ra age constraints. From these lines of evidence, we can infer that the off-axis E-MORB were emplaced within ~3 km of the axis, which is within the present-day extent of the neo-volcanic zone (Fornari *et al.*, 1998; Schouten *et al.*, 1999; Sims *et al.*, 2003; Soule *et al.*, 2005), and that their distribution reflects that of preservation, and not eruption: abundant E-MORB are found in areas of diminished young volcanism and less frequent volcanic repaving of the ocean floor, such as off-axis to the west at 9°50′N, off-axis to the east at 9°30′N, and at the western limb of the small OSC at 9°37′N EPR (Fig. 1). Furthermore, although the resolution of the ^{238}U–^{230}Th dating technique, particularly for E-MORB, is not precise enough to discern fine-scale differences in E-MORB vs N-MORB eruption times, model eruption ages for E-MORB are as little as ~5 kyr different from N-MORB eruption ages (Fig. 9; Table 6). Thus, we speculate that shifts in the bulk mantle source composition and/or the melt transport processes that sample and preserve the enriched melt compositions reflected in the isotopic and chemical variations of EPR lavas may occur over relatively short time scales, perhaps <1–10 kyr.

E-MORB samples 2489-3 and 2489-4a plot above the line for axial emplacement because they have ^{238}U–^{230}Th model ages of 81 ± 26 and 100 ± 27 ka, respectively, which are much greater than their spreading ages (41 ka and 48 ka, respectively). One possible explanation for why these lavas have model ages ~40 kyr older than their spreading ages is that they have been exposed by faulting. However, although many of the E-MORB in this study—including samples 2489-3, 2489-4a, and 2489-5, which are nearly identical with respect to their chemical compositions and paleointensities—were sampled from near a large volcanic growth fault (Macdonald *et al.*, 1996), the exposed graben on the east side of the axis at 9°30′N is only ~75 m below what would be expected if the extrusive layer were constructed symmetrically about the ridge axis. However, the lava 'missing' from this graben amounts to only ~500 years to several thousand years worth of volcanic construction (Escartin *et al.*, 2007). Thus, exposure of these E-MORB by faulting and uplift is not sufficient to explain this age disparity. Hence, this age disparity is physically implausible and must be explained otherwise.

Older eruption age estimates by ^{231}Pa model age dating on sample 2489-3 gave a similar result of 64 ± 3 ka (Goldstein *et al.*, 1994). Goldstein *et al.* (1994) attributed this discrepancy to either a longer magma residence time for this sample or asymmetric spreading with slower spreading on the Cocos side. Although longer magma residence times can explain this discrepancy, constraints from other U-series disequilibria, namely ^{226}Ra and ^{210}Pb disequilibria, indicate very short residence times of only hundreds of years (Sims *et al.*, 2002; Rubin *et al.*, 2005), compared with the ~40 kyr needed to explain this discrepancy. If we assume that a melt lens containing E-MORB type magma was stored at a depth in the crust similar to the present-day AMC, but for 40 kyr instead of a few hundreds of years, this melt body would undergo much greater extents of cooling, crystallization, and compositional evolution than the N-MORB. However, these E-MORB samples are not correspondingly more differentiated than N-MORB samples. Despite substantial evidence for asymmetric construction of the extrusive layer to the east of the AST at 9°30′N, given the bilateral symmetry of small and large flow fronts on either side of the AST, spreading is most probably a symmetric process from 9°30′N to 9°50′N EPR (Fornari *et al.*, 2004). Instead, we suggest that the coherent isotopic variations seen between off-axis N-MORB and off-axis E-MORB from this area hint at complexity in the processes (namely, coupled variations in degree of melting and source composition) that generate U-series disequilibria, and, as such, it is likely that both our model age calculations and those of

Goldstein *et al.* (1994) may be flawed because of invalid assumptions about the initial (^{230}Th/^{232}Th) and (^{231}Pa/^{235}U) for these specific samples (see Sims *et al.*, 2003).

We also note that Goldstein *et al.* (1994) calculated a model age of 74 ± 3 ka for sample 2489-12. This is consistent with the spreading age of 78 ka, but much greater than the age indicated by its paleointensity (~40 ka) and our U–Th model age of 31 ± 11 ka. The reason for this discrepancy is because we use a different initial (^{230}Th/^{232}Th) based on the zero-age trend-line, whereas Goldstein *et al.* (1993, 1994) used a single and constant initial (^{230}Th/^{232}Th) and (^{231}Pa/^{235}U) value. For sample 2489-12, from its lower (^{230}Th/^{232}Th) and (^{238}U/^{232}Th) and more radiogenic isotope composition, we see that the assumption of constant initial (^{230}Th/^{232}Th) for all N-MORB is clearly erroneous. Likewise, we speculate that near the E-MORB end-member, our zero-age trend-line is not necessarily an accurate representation of the initial (^{230}Th/^{232}Th) for samples 2489-3 and 2489-4a. The initial (^{230}Th/^{232}Th) for these samples were possibly much lower and more similar to those for the enriched Siqueiros lavas. The wide range of (^{230}Th/^{232}Th) and large scatter around the zero-age trend-line exhibited by E-MORB from the 9–10°N EPR region (Goldstein *et al.*, 1993, 1994; Sims *et al.*, 2002, 2003), Siqueiros (Lundstrom *et al.*, 1999), and Juan de Fuca and Gorda Ridge (Goldstein *et al.*, 1992, 1993) seem to suggest that it is somewhat difficult to predict initial (^{230}Th/^{232}Th) for some samples for the purpose of calculating model ages. In contrast, initial (^{230}Th/^{232}Th) values in N-MORB appear much more homogeneous and predictable, as suggested by the coherent ages determined by U-series (Sims *et al.*, 2003) and paleointensity (Bowles *et al.*, 2006) methods.

Petrogenesis of E-MORB

Recent studies of E-MORB far from hotspots have argued for a globally common process for MORB-source enrichment through subduction of ocean island basalt (OIB) material or through metasomatic enrichment of the mantle wedge or oceanic lithospheric mantle (Niu *et al.*, 2002; Donnelly *et al.*, 2004; Hemond *et al.*, 2006; Nauret *et al.*, 2006). For example, Donnelly *et al.* (2004) argued that E-MORB are produced by a process in which a small proportion (0·5%) of eclogitized slab melt (batch melt of F ~1%) enriches by metasomatism the overlying mantle wedge peridotite (of depleted mantle composition and in the proportion of 99·5%) in the most incompatible trace elements. This metasomatized peridotite [99·5% depleted mantle, 0·5% eclogite melt (F ~1%)] is subsequently entrained in the upper mantle over a time scale (a few hundred million years) long enough to change its Nd, Hf, Sr, and Pb isotope compositions. This aged metasomatized peridotite then undergoes high degrees of melting (9%) at shallow depths (above the garnet–spinel transition) beneath ridges to produce E-MORB. By batch melting metasomatized spinel peridotite, this model accounts for the chondritic Dy/Yb in E-MORB—as it is argued that melting in the presence of garnet will produce too high Dy/Yb.

Although the Donnelly *et al.* (2004) model reproduces the trace element abundances of the EPR E-MORB fairly well (see below), they did not address the observations of ^{230}Th excesses in MORB (e.g. Goldstein *et al.*, 1992, 1993, 1994; Volpe & Goldstein, 1993; Lundstrom *et al.*, 1995, 1999, 2000; Sims *et al.*, 1995, 2002, 2003), which require very recent melting in the presence of garnet (≪375 kyr ago). Previous experimental studies have demonstrated that large ^{230}Th excesses must be generated in the presence of garnet, and that even in the presence of garnet, significant fractionation of Th over U may occur only at very low degrees of melting (Beattie, 1993; LaTourrette *et al.*, 1993; Hauri *et al.*, 1994; Salters & Longhi, 1999; Landwehr *et al.*, 2001; Salters *et al.*, 2002; Pertermann *et al.*, 2004; Elkins *et al.*, 2008). Because of the small D values for Th and U in all relevant phases, batch melting of metasomatically enriched spinel peridotite to F ~8–10% is inconsistent with observed large ^{230}Th excesses in both Pacific N-MORB and E-MORB (unless the metasomatism is recent; i.e. took place much more recently than ~375 kyr ago). However, this recent metasomatism is not supported by the long-lived radiogenic isotope compositions of E-MORB reported in this study, which imply an old (10^8–10^9 years) enrichment process and subsequent radiogenic ingrowth.

Studies of U-series disequilibria at 9–10°N EPR and the Juan de Fuca Ridge demonstrate a positive correlation between (^{230}Th/^{232}Th) and (^{238}U/^{232}Th) (Fig. 8a) (Goldstein *et al.*, 1993; Lundstrom *et al.*, 1995, 1999; Sims *et al.*, 1995, 2002) and negative correlations between ^{230}Th excesses and (^{238}U/^{232}Th) and between primary ^{230}Th and ^{226}Ra excesses (Fig. 8b and c) (Volpe & Goldstein, 1993; Lundstrom *et al.*, 1995, 1999; Sims *et al.*, 1995, 2002). These N-MORB and E-MORB data also show a distinct correlation between ^{238}U–^{230}Th disequilibria and Sm/Nd fractionation (Sims *et al.*, 1995). Data presented in this study augment these correlations (Fig. 8). The most recent studies of U-series disequilibria in 9–10°N EPR lavas have shown that for lavas to have both negatively correlated primary ^{226}Ra and ^{230}Th excesses and positively correlated (^{230}Th/^{232}Th) and (^{238}U/^{232}Th), the melting must occur in a two-porosity melting regime (Kelemen *et al.*, 1997; Sims *et al.*, 1999, 2002; Lundstrom, 2000; Jull *et al.*, 2002). Based on these U-series constraints, which require recent fractionation in the presence of garnet and subsequent mixing of melts, we propose that the mixing trends among trace elements and long-lived radiogenic isotopes reflect mixing of melts during melt extraction and crustal residence and not large-degree melting of an ancient, metasomatized spinel peridotite. Below,

we put forward a model for the genesis of E-MORB that involves low-degree melting of an enriched, garnet-bearing source that is melting deep and in the marginal extents of the MORB melting regime (i.e. corners, bottom). Metasomatism, recycling of oceanic crust (MORB), and recycling of OIB are all possible candidates for the origin of the mantle source enrichment of E-MORB. However, the large ^{230}Th excesses observed in E-MORB are difficult to reconcile with a model that involves large degrees of melting of ancient metasomatized spinel peridotite.

A model for progressive polybaric and two-porosity melting and mixing in a lithologically and chemically heterogeneous mantle source

In an effort to reproduce the trends and ranges of compositional and isotopic variability observed for the 9–10°N EPR data (Sims *et al.*, 2002, 2003; this study) we have developed a model in which melting occurs in a lithologically and chemically heterogeneous source composed of pyroxenite and peridotite. In our polybaric, progressive melting scenario, the derived melts of each lithology are accumulated and mixed at all depths during transport through the mantle or in shallow crustal reservoirs. This model is similar to that of Stracke & Bourdon (2009). We also simulate two-porosity melting and mixing by mixing deep pyroxenite melts with shallow melts produced from the polybaric, progressive melting model. However, we note that although Stracke & Bourdon (2009) compared their model results with both Icelandic and 9–10°N EPR lavas, the suite of EPR lavas they used are N-MORB from Sims *et al.* (2002), which do not display the elemental and isotopic variability of the E-MORB and N-MORB reported in this study. Thus, they were not able to use their model to place constraints on the relationships between melting and the compositional variability of MORB. They also did not investigate the effects of a two-porosity melting regime on lava compositions.

Physical model parameters for progressive polybaric melting and mixing

Model parameters are illustrated in Figs 10–12. Figure 10a shows the assumed adiabatic gradient and the solidi for peridotite and three pyroxenites used to calculate the trace element compositions of melts produced by melting of a lithologically and compositionally heterogeneous mantle source. The mantle potential temperature was set at 1340°C with an adiabatic gradient of 10°C GPa^{-1} (Ita & Stixrude, 1992), which coincides with melting of dry peridotite at ~60 km, or ~2 GPa, using the solidus of Hirschmann (2000). Three pyroxenite solidi were used to investigate variations in melt composition that result from changes in the depth of the pyroxenite solidus relative to the peridotite solidus. The deepest pyroxenite solidus was parameterized after the G2 solidus (Pertermann & Hirschmann, 2003), and the shallower pyroxenite solidi, which are intended to be representative of the range of possible solidi expected for the silica-deficient pyroxenite MixlG (Hirschmann *et al.*, 2003; Kogiso *et al.*, 2003; Elkins *et al.*, 2008), were assumed to be parallel to the solidus of G2. We assumed maximum and minimum solidi for MixlG of 1375°C and 1405°C at 2·5 GPa [similar to the range of 1375–1400°C found by Hirschmann *et al.* (2003)].

The effects of different productivities and solidus depths on the total melt fraction, as modeled in this study, are shown in Fig. 10b. Pyroxenite productivity was calculated as a function of pressure based on the parameterization of a silica-rich pyroxenite (G2) from Pertermann & Hirschmann (2003). Under these conditions, G2 pyroxenite crosses its solidus at ~3·5 GPa and melts >70% prior to peridotite melting. In contrast, the MixlG pyroxenite crosses its solidus between 2·16 and 2·45 GPa and melts only ~3–12% before peridotite starts melting. Once peridotite melting begins, pyroxenite productivity decreases to a constant 16·5% GPa^{-1} (Hirschmann & Stolper, 1996). G2 pyroxenite melts 100% by the time peridotite melting ceases; the total degree of melting (F) of MixlG pyroxenite ranges from 35 to 44%. We assume that peridotite melting begins in the spinel stability field and that peridotite productivity is constant, adjusting peridotite productivities in each of the three cases ($dF/dP_{G2} = 5\%$ GPa^{-1}, $dF/dP_{MixlG\text{-}1375^\circ C} = 3\%$ GPa^{-1}, and $dF/dP_{MixlG\text{-}1405^\circ C} = 11\%$ GPa^{-1}) to best match the trace element abundances of E-MORB and N-MORB samples.

Figure 10c shows the relative contribution of melt from either a peridotite or a pyroxenite source for each pyroxenite solidus, assuming that pyroxenite constitutes 3% of the total solid mantle, which is consistent with constraints on G2 pyroxenite solid volumes based on oceanic crustal thickness (Pertermann & Hirschmann, 2003). Peridotite and pyroxenite melts are mixed in proportions based on their relative melt fractions (where relative melt fraction $= F_{pyx}X_{pyx}/[F_{pyx}X_{pyx} + F_{Peridotite}(1 - X_{pyx})]$, where F_{pyx} is the pyroxenite melt fraction, $F_{Peridotite}$ is the peridotite melt fraction, and X_{pyx} is the solid fraction of pyroxenite).

Figure 10d is a plot of pressure (GPa) vs pyroxenite productivity (% GPa^{-1}), illustrating the model parameterization after Hirschmann & Stolper (1996) and Pertermann & Hirschmann (2003). G2 pyroxenite initiates melting at ~3·5 GPa and productivity increases rapidly to ~71% GPa^{-1} before peridotite begins melting. MixlG pyroxenite (with the minimum solidus estimate of 1375°C) initiates melting at ~2·45 GPa and productivity peaks at ~31% GPa^{-1}. The hotter MixlG pyroxenite solidus (1405°C) crosses the adiabat at ~2·16 GPa and increases productivity to a maximum of ~20% GPa^{-1}. Again, once peridotite begins melting, all pyroxenite productivities are 16·5% GPa^{-1}.

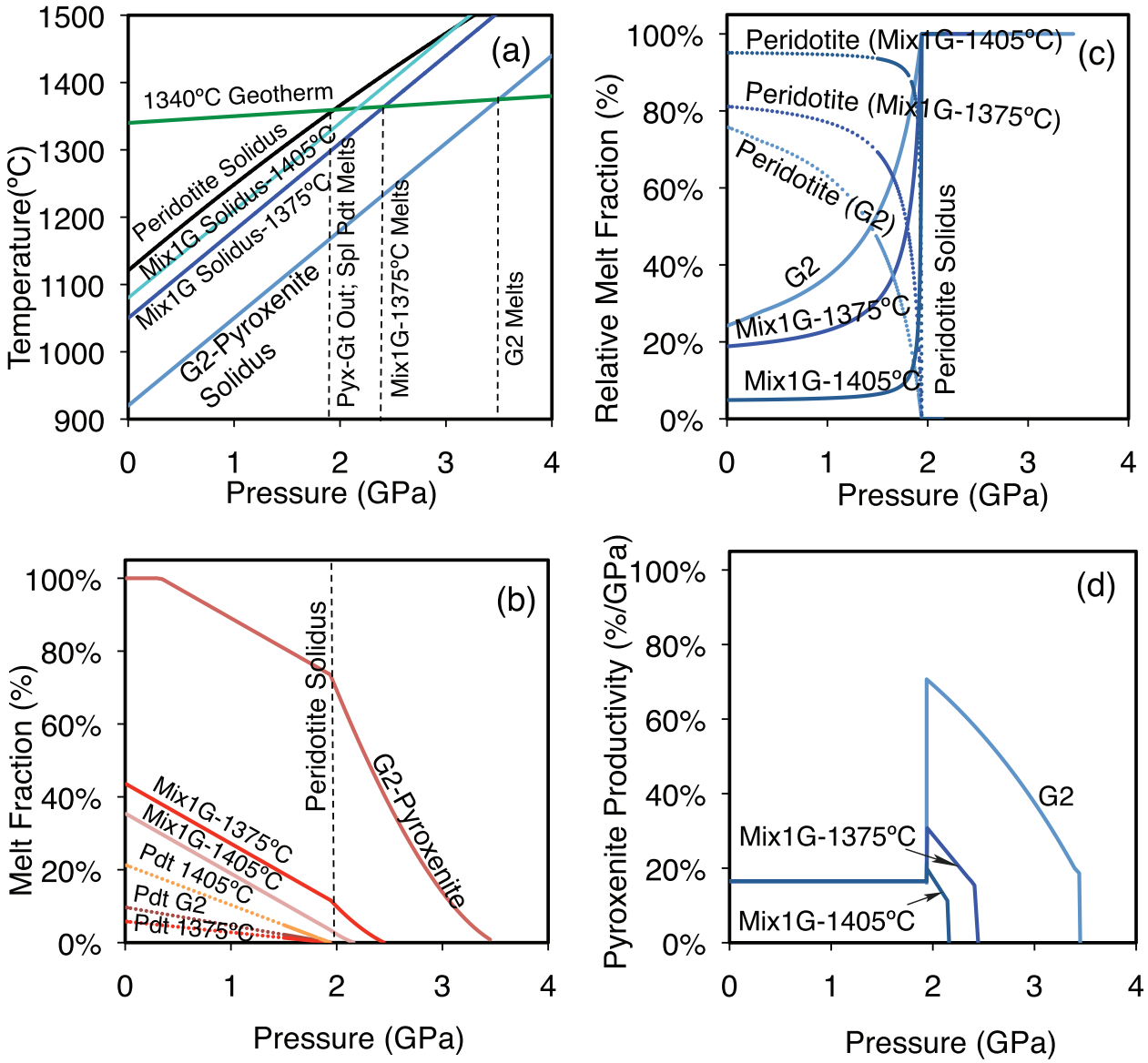

Fig. 10. (a) Variation of pressure (GPa) vs temperature (°C) showing the adiabatic gradient and the solidi for peridotite and three pyroxenites used to calculate the trace element compositions of melts produced by melting of a lithologically and compositionally heterogeneous mantle source. (b) Pressure (GPa) vs melt fraction (%) showing the effect of different productivities and solidi depths on the total melt fraction, as modeled in this study. (c) Pressure (GPa) vs relative melt fraction (%) showing the relative contribution of melt from either a peridotite or a pyroxenite source for each pyroxenite solidus. (d) Pressure (GPa) vs pyroxenite productivity (% GPa^{-1}) showing model parameterization, after Hirschmann & Stolper (1996) and Pertermann & Hirschmann (2003). Pyx-Gt, garnet in pyroxenite; Spl, spinel; Pdt, peridotite. (See text for details.)

Given the productivities (Fig. 10d), for a large difference in pyroxenite and peridotite solidi, as is the case for G2 pyroxenite, pyroxenite melt compositions will have a more lasting influence on the bulk melt composition and ultimately contribute a much greater fraction of the total volume of melt than the unmelted pyroxenite did to the solid mantle (~24% melt vs 3% solid). In contrast, more similar pyroxenite and peridotite solidi—particularly Mix1G (1405°C)—result in much more rapid decreases in the proportion of pyroxenite melt and thus pyroxenite compositional influence. In all cases, however, peridotite melting overwhelms pyroxenite melting—pyroxenite melt constitutes only 5–24% of the total melt.

Chemical model parameters for progressive polybaric and two-porosity melting and mixing

Using the physical model parameters described above, we have also investigated the effect of progressive depletion of

a lithologically and chemically heterogeneous (i.e. pyroxenite + peridotite) mantle source on the trace element composition of melts. To simulate progressive depletion, peridotite and pyroxenite undergo modal fractional melting independently and the accumulated melts from both lithologies are mixed at all depths. In Fig. 11 and the discussion below, we refer to these accumulated pyroxenite–peridotite melt mixes as 'mixed melts (MM)'. To simulate a 'two-porosity (TP)' melting regime, we mix deep pyroxenite melts with shallow accumulated mixed melts of EPR N-MORB composition. For the peridotite source, we use the DMM composition of Workman & Hart (2005), and for the pyroxenite source, we use the composition of Donnelly *et al.* (2004) for average EPR oceanic crust, noting that the true sources—particularly the enriched source—are not well constrained. Peridotite partition coefficients are taken from a compilation by Donnelly *et al.* (2004), and bulk pyroxenite partition coefficients are calculated from Pertermann & Hirschmann (2004), using the cpx/melt D values from run A343 and garnet/melt D values from the 'preferred average' (see Pertermann & Hirschmann, 2004, table 9). Spinel peridotite mineral proportions are 52% olivine, 18% clinopyroxene, and 30% orthopyroxene (from Donnelly *et al.*, 2004). Trace elements are assumed to partition between spinel and melt similarly to olivine/melt. Pyroxenite mineral proportions are 82% clinopyroxene and 18% garnet, as described by Pertermann & Hirschmann (2003). We also assume that garnet is no longer stable in pyroxenite at the peridotite solidus (Pertermann & Hirschmann, 2003).

Progressive polybaric and two-porosity melting and mixing model results

Figure 11 shows trajectories for melting of peridotite, pyroxenite, and the mixed melts of peridotite and pyroxenite that are meant to represent progressive depletion of a lithologically and chemically heterogeneous mantle source. The three peridotite melting trajectories distinguish peridotites with three productivities [e.g. the most productive peridotite source, Mix1G (1405°C), undergoes the greatest extent of melting, whereas the least productive peridotite, Mix1G (1375°C), undergoes the smallest extent of melting]. The pyroxenite melting trajectories illustrate the effects of different solidi on trace element compositions. Figures 11c & d shows that mixed melts G2 and Mix1G (1375°) follow trajectories nearly identical to their respective pyroxenite melting trajectories (Figs 11a & b) and that these melting trajectories do not closely match the MREE/HREE compositions of 9–10°N E-MORB, nor the mixing trend among N-MORB and E-MORB lavas, although the final compositions are similar to N-MORB. However, the smaller the difference in solidi, the more closely the trajectory matches the mixing trend observed among N-MORB and E-MORB lavas. For example, although assuming that a deep G2 pyroxenite solidus produces a trajectory nearly perpendicular to the EPR lava mixing trend, Mix1G (1375°C) is more similar to the observed EPR mixing trend, and Mix1G (1405°C) is even more similar (Fig. 11d). This is probably because Mix1G (1405°C) melts only ~3% prior to peridotite melting, and the enriched pyroxenite melt Sm/Nd is slower to respond to the addition of more depleted spinel peridotite melts than either G2 or Mix1G (1375°C) pyroxenite melts, which are more depleted by the onset of peridotite melting and have concentrations more similar to the spinel peridotite melts.

However, Fig. 11c clearly shows that the G2, Mix1G (1375°C), and Mix1G (1405°C) mixed melt trajectories have the wrong sense of curvature to account for the observed variations in EPR lava Th/U. Thus, progressive depletion of a heterogeneous mantle source cannot account for the observed EPR mixing array. As stated above, we also investigated the effect of a two-porosity melting regime on trace element compositions by mixing accumulated deep pyroxenite and shallow mixed melts (high and low pressure, respectively) for G2 and Mix1G (1375°C) pyroxenite solidi. The trajectories of these two-porosity melts are determined initially by melting of pyroxenite, and then mixing of pyroxenite melts with shallow mixed melts. These trajectories are shown in Fig. 11e–h. It should be noted that we do not calculate two-porosity melts for Mix1G (1405°C) because of the close proximity of its solidus to the peridotite solidus. We observe that mixing of deep, low-degree (~1%) pyroxenite melts with shallow mixed melts resembling EPR N-MORB appears to best reproduce the mixing trends observed in plots of Sm/Yb vs Th/U (Fig. 11e) and Sm/Yb vs Sm/Nd (Fig. 11f) among EPR E-MORB and N-MORB lavas. Thus we conclude that mixing of deep, enriched garnet pyroxenite melts with shallow melts produced by progressive depletion of a heterogeneous mantle better reproduces the EPR trace element data than progressive depletion of a heterogeneous mantle alone.

One of the strongest constraints on the genesis of EPR E-MORB is the presence of both shallow MREE/HREE slopes on mantle-normalized diagrams (Donnelly *et al.*, 2004) and large ^{230}Th excesses. Although the shallow, near-chondritic MREE/HREE slope has been used to argue against the presence of garnet in the mantle source residue (Donnelly *et al.*, 2004), the large ^{230}Th excesses (up to 20%) indicate otherwise. This seeming discrepancy can be reconciled by recognizing that highly incompatible elements, such as U and Th, are strongly partitioned into the melt in the smallest melt fractions, whereas the concentrations of moderately incompatible elements, such as the MREE and HREE, continue to change at higher degrees of melting. In the case of our two-porosity model, low degrees of melting of enriched pyroxenite will produce melts that are much more enriched in Th and U than the shallow, depleted peridotite melts with which they mix, with

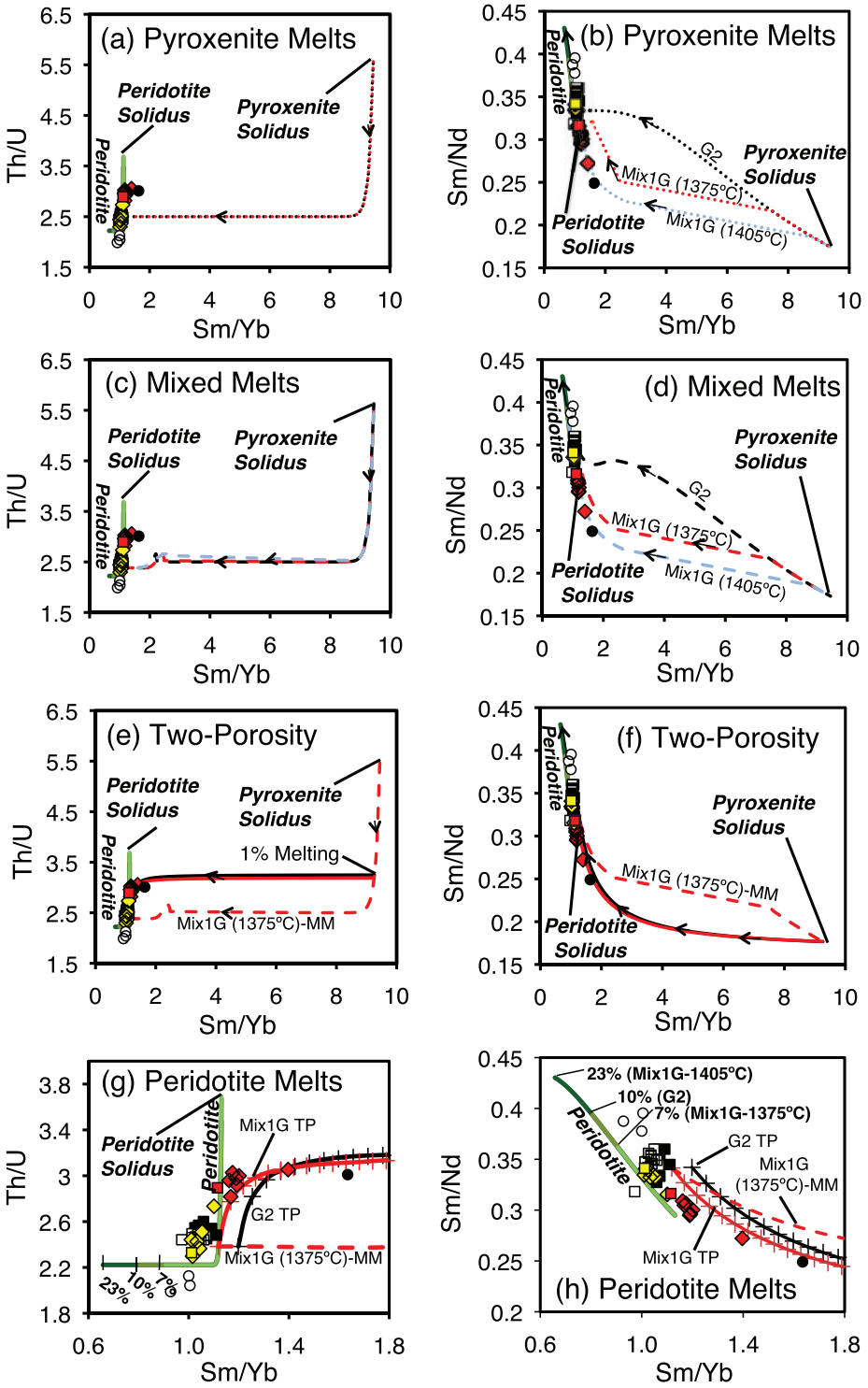

Fig. 11. Plots of Sm/Yb vs Th/U and Sm/Yb vs Sm/Nd for model results showing (a, b) pyroxenite melt, (c, d) mixed melt, (e, f) two-porosity, and (g, h) peridotite melt trajectories compared with the 9–10°N EPR dataset. (g) and (h) are expanded views to show more detail and have different scales from the other panels. Dotted trajectories shown in (a) and (b) are pure pyroxenite melts, dashed trajectories in (c) and (d) are mixed pyroxenite–peridotite melts intended to represent progressive melting of a pyroxenite–peridotite mantle source, and continuous-line trajectories in (e)–(h) are two-porosity melts calculated by mixing of deep pyroxenite melts with shallow mixed melts. Crosses along the two-porosity trajectories in (g) and (h) indicate 1% mixing increments. MixlG (1375°C) mixed melt (MM) trajectory (dashed line) is shown in (e)–(h) for reference. It should be noted that pyroxenite melting and mixed-melt trajectories for G2, MixlG (1375°C), and MixlG (1405°C) in (b) and (d) are essentially identical. Two-porosity trajectories for G2 and MixlG in (e) and (f) overlap and only MixlG (1375°C) is shown; single model trajectories are labeled in all other panels. Peridotite melting trajectories are represented in (g) and (h) by continuous lines labeled 'peridotite', and maximum extents of melting for different peridotite productivities are marked [23% for MixlG (1405°C) with 11% GPa^{-1}; 10% for G2 with 5% GPa^{-1}; 7% for MixlG (1375°C) with 3% GPa^{-1}]. Arrows along trajectories indicate decreasing pressure and increasing extent of melting. MM, mixed melts; TP, two-porosity. Data symbols and references are the same as in Figs 2 and 5 and 6.

the outcome that the pyroxenite melts will control the highly incompatible element ratios, such as Th/U. In contrast, more moderately incompatible elements, such as the MREE and HREE, will not be removed from the solid mantle as extensively at the same low degrees of melting and will therefore not experience the same relative enrichment in the melt as the highly incompatible elements. Consequently, peridotite and pyroxenite melts will have more similar MREE and HREE concentrations than they would Th and U concentrations, and thus peridotite melts will be more effective at diluting the concentrations of pyroxenite MREE and HREE and changing their MREE/HREE ratios. For example, the two-porosity melting trajectories in Fig. 11e show that there is a large change in Th/U (and Th and U abundances, not shown) for the first ~1% of melting of garnet pyroxenite and essentially no change in Sm/Yb [note that Mix1G (1405°C) pyroxenite starts mixing with peridotite at ~3% melting]. The strongly hyperbolic geometry of these melting trajectories is a direct response to the partitioning differences between Th and U and the MREE and HREE, and the ability of large volumes of depleted peridotite melts to dilute the MREE and HREE, but not the highly incompatible elements.

Finally, we attempted to match the trace element concentrations of the most enriched E-MORB sample, 2703-1, while still adequately matching the average N-MORB composition, by progressive depletion of a heterogeneous source (Fig. 12). For extraction of N-MORB melt, we cease melting of Mix1G (1405°C) + peridotite at 1 GPa, G2 + peridotite at 1 GPa, and Mix1G (1375°C) + peridotite at 0·1 GPa. Both G2 and Mix1G (1375°C) model N-MORB are very similar to average 9–10°N EPR N-MORB, but the Mix1G (1405°C) model N-MORB is more depleted than average 9–10°N EPR N-MORB owing to higher peridotite productivity (11% GPa^{-1}) (Fig. 12).

Mix1G (1405°C) pyroxenite–peridotite mixed melts were extracted at ~1·79 GPa to best reproduce the incompatible element abundances of sample 2703-1 (Fig. 12). In contrast, G2 and Mix1G (1375°C) pyroxenite–peridotite mixed melts resemble pure enriched pyroxenite melts when their abundances in the most incompatible elements are similar to E-MORB 2703-1. These melts are similar to pure pyroxenite melts because their trace element budgets are largely controlled by the enriched pyroxenite melt, and peridotite melting has not substantially diluted the abundances of the MREE and HREE (Fig. 11). This observation allows us to further rule out progressive depletion of a lithologically and chemically heterogeneous pyroxenite + peridotite mantle as a source for E-MORB under conditions where the pyroxenite has a deeper solidus. However, our two-porosity melts appear to reproduce the trace element abundances fairly well (Fig. 12b and c). Binary mixing of small proportions (5%) of ~1% melts of G2 and Mix1G (1375°C) pyroxenites with peridotite–pyroxenite mixed melts at 1 and 0·1 GPa (the pressures for N-MORB extraction) result in excellent matches to the pattern for E-MORB 2703-1 (Fig. 12b and c), suggesting that a two-porosity melting regime is plausible, but indicating that melting of the enriched component must be limited to about 1% (for accumulated fractional melting).

Thus, our modeling illustrates that to reproduce the observed shallow MREE/HREE slope (e.g. Sm/Yb) and still maintain high $^{230}Th/^{238}U$ (and by inference high Th/U) in E-MORB, small proportions (<5%) of low-degree, enriched melts of garnet pyroxenite (with relatively high Th/U) must mix with large proportions (>95%) of depleted melts of N-MORB composition (Figs 11c and 12). Although our model suggests that melts of N-MORB composition may be produced by progressive melting of a lithologically heterogeneous mantle, it is also possible that the most depleted N-MORB end-member melts may be generated solely by melting of spinel peridotite, with the caveat that mixing of these N-MORB melts with some E-MORB melt must occur to produce the observed ^{230}Th excesses (Fig. 11).

Melting and mixing model discussion: implications for EPR E-MORB genesis

As discussed above, three distinct scenarios can explain the asymmetric and off-axis distribution and the preserved enriched composition of 9–10°N EPR E-MORB: (1) E-MORB and N-MORB are produced concurrently, but E-MORB are transported to small off-axis magma bodies (bypassing AMC storage) and erupted shortly thereafter (Goldstein *et al.*, 1994; Perfit *et al.*, 1994); (2) E-MORB and N-MORB melts are produced at separate time intervals owing to periodic introduction of heterogeneities into the melting region or shifts in the melt transport and storage processes, but E-MORB do not bypass the AMC, but rather occupy it at discrete time intervals (Batiza & Niu, 1992); (3) E-MORB and N-MORB melts are produced concurrently and occupy the AMC at the same time, but during periods of E-MORB volcanism, E-MORB and N-MORB melts are not thoroughly homogenized because of physical discontinuities in the AMC or melt transport system (presumably during periods of short-lived and diminished magmatism). In the first scenario, E-MORB are hypothesized to erupt only off-axis, whereas in the latter two scenarios, E-MORB are allowed to erupt from within the AST. Because we believe the first scenario is relatively inconsistent with what we now know about neo-volcanic zone construction, we dismiss it as unlikely.

The second scenario contends that E-MORB and N-MORB production occurs at discrete time intervals, thus avoiding mixing in the AMC at periods of time in which N-MORB melt is abundant enough to overwhelm any enriched E-MORB signature. Periods of N-MORB volcanism alternate with periods of transitional, and then

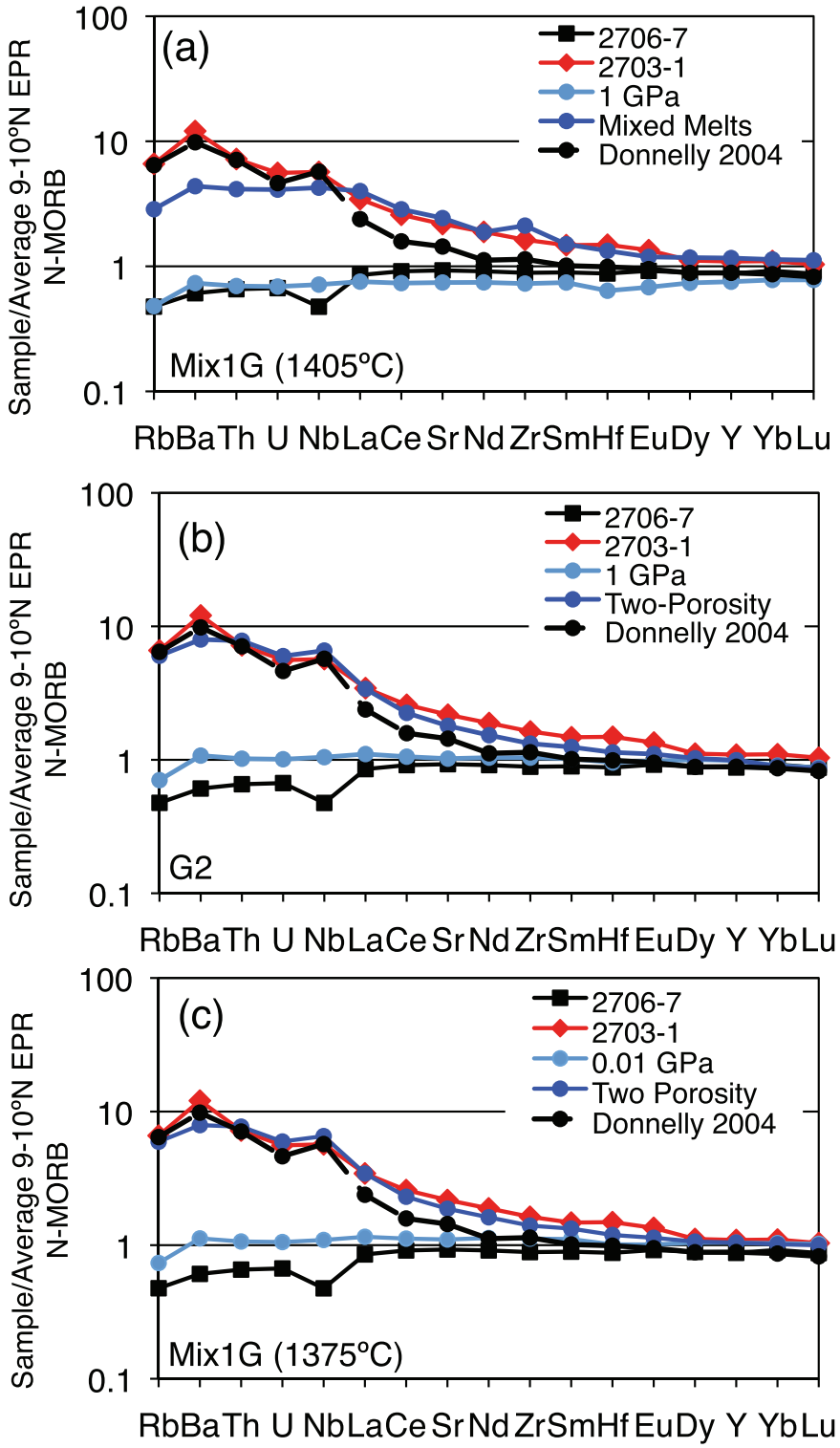

Fig. 12. Trace element abundances of modeled E-MORB and N-MORB melts normalized to average axial 9–10°N EPR N-MORB (Sims *et al.*, 2002) for one-dimensional melting of peridotite. (a) Mix1G (1405°C) mixed melt; (b) G2 two-porosity melt; (c) Mix1G (1375°C) two-porosity melt. The most enriched (2703-1) and depleted (2706-7) 9°30′N EPR samples from this study are shown for comparison. Using the parameters described in the captions to Figs 10 and 11, we have tried to match the most enriched E-MORB composition while still adequately matching the average N-MORB composition (labeled by melt extraction pressures of 1 and 0·01 GPa) by progressive depletion of a heterogeneous source. The results of the Donnelly *et al.* (2004) model are also shown. (See text for details.)

dominantly enriched volcanism as the supply of enriched melts increases. This type of scenario requires that the magmatic system either randomly ceases the sampling of isotopic heterogeneities for given time intervals, or that new enriched heterogeneities periodically enter the melting region. If this is the case, based on our model ages, either variations in the melt transport system occur or heterogeneities are periodically introduced into the melting region on time scales of <1–10 kyr. We note that periodic introduction of new heterogeneities into the melting region does not require that older heterogeneities be removed from the melting region. This scenario does, however, require that beyond the threshold of 1% melting, melts from the older heterogeneities cannot be transported to shallow depths to mix directly with depleted melts. If this scenario is correct, we suspect that these higher degree melts become 'hidden' by thorough mixing with peridotite melts during progressive depletion (i.e. constrained to a 'mixed melts' trajectory).

As described in the melt modeling section above, our trace element modeling is consistent with the third scenario, which involves concurrent production of N-MORB (through progressive depletion) and E-MORB (through mixing of deep and shallow melts) and with shared N-MORB and E-MORB storage in the shallow mantle or AMC. The large proportion of N-MORB melts (>95%) required to mix with the enriched pyroxenite end-member melts (<5%) to generate the EPR mixing array strongly suggests that mixing commonly nears completion (to the N-MORB end-member composition). Whether mixing occurs in the shallow mantle or in the AMC, diminished magmatic activity should allow for even better separation of geochemically variable melts. Our melting model further suggests that only a slight variation in the proportion of N-MORB melt available in the AMC can mean the difference between erupting N-MORB and E-MORB.

Although the AMC at 9–10°N EPR may be continuous along-axis on the scale of tens of kilometers, remaining continuous through even third-order discontinuities (e.g. Kent *et al.*, 1993; Toomey *et al.*, 1994; White *et al.*, 2002), it has been proposed, based on seismic studies, that this may occur because of the geometry of the AMC, where along-axis mixing of geochemically diverse melts may be inhibited by the thinness (~10–50 m) of the melt lens overlying partially solidified crystal mush (Kent *et al.*, 1993; Singh *et al.*, 1998). In regions of decreased magma replenishment, the melt lens may be thinner and the crystal mush zone thicker, further inhibiting homogenization of depleted and enriched melts. Indeed, this is what we observe at 9–10°N EPR. The more magmatically robust 9°50′N EPR ridge segment has a much greater abundance of lavas of more transitional compositions (akin to the chemically but not isotopically enriched sample 2697-1) in comparison with the less magmatically robust 9°30′N ridge segment, where E-MORB tend to be more enriched (e.g. sample 2703-1; Fig. 1). Across-axis bathymetric profiles at 9°30′N show that the current AST is nested within a larger, older axial graben, suggesting a relatively recent increase in volcanic and magmatic activity (Fornari *et al.*, 1998), which would explain why E-MORB have not been recently erupted from this region. Lastly, this is consistent with variations in Mg-number, where even N-MORB erupted from 9°30′N tend to be more evolved than those erupted at 9°50′N. Similar relationships between seismic estimates of AMC melt content and wt % MgO have been observed to vary along-axis at the Juan de Fuca Cleft segment (Canales *et al.*, 2006).

CONCLUSIONS

Geological and geophysical evidence for diminished volcanic activity in the 9°30′N region, particularly to the east side, has been presented in numerous studies (e.g. Harding *et al.*, 1993; Toomey *et al.*, 1994; Fornari *et al.*, 1998; Schouten *et al.*, 1999; Crawford & Webb, 2002; Soule *et al.*, 2005; Bowles *et al.*, 2006; Escartin *et al.*, 2007). However, decreased volcanism and the preservation of E-MORB have so far been only tentatively linked (Reynolds *et al.*, 1992; Smith *et al.*, 2001). To understand the geological and temporal relationships between N-MORB and E-MORB, we have measured major and trace elements, and Sr, Nd, Hf, Pb, and U–Th–Ra isotopes for a suite of lavas collected off-axis, including several E-MORB, from the 9–10°N region along the East Pacific Rise.

Age constraints from magnetic paleointensities and U–Th–Ra disequilibria show that E-MORB from 9°30′N EPR erupted from 12 to 85 ka, indicating that these lavas have not been covered by subsequent volcanic activity in the form of lava flows down the ridge flanks. This is consistent with observations that volcanic activity is locally diminished west of the AST at 9°50′N, east of the AST at 9°30′N, and near the dying western limb tip at 9°37′N, which are all locations where E-MORB have been sampled in greater abundance. After correction for spreading, the paleointensity and U-series age constraints further indicate that emplacement of E-MORB lava flows occurred from 0 to 3 km from the AST. In fact, there are no systematic differences in the emplacement locations of E-MORB and N-MORB throughout the 9–10°N EPR region, implying similar emplacement mechanisms for the two types of basalt. Thus, our examination of geological, magnetic paleointensity, and U–Th–Ra age constraints supports the notion that 9–10°N EPR E-MORB compositions are preserved on the seafloor because of locally diminished volcanic activity, and not because they were necessarily erupted off-axis, as has been previously suggested (Perfit *et al.*, 1994).

E-MORB from 9°30′N have more enriched $^{87}Sr/^{86}Sr$, $^{143}Nd/^{144}Nd$, and $^{176}Hf/^{177}Hf$ isotope compositions and

elevated highly incompatible element abundances compared with any of the N-MORB from the 9–10°N EPR region reported in this study and by Sims *et al.* (2002, 2003). However, E-MORB and N-MORB from the 9–10°N EPR region form a continuum of compositions that are best explained by mixing of melts derived from a heterogeneous mantle source with at least two major components that are both elementally and isotopically distinct. All young N-MORB and E-MORB collected from within ~5 km of the AST along 9–10°N EPR have significant ^{230}Th excesses (Sims *et al.*, 2002, 2003), most probably indicating the presence of garnet in the mantle source residue and recent (<375 ka) fractionation of U from Th. These observations are at odds with studies of E-MORB that have called upon a two-stage process involving (1) ancient metasomatism and (2) melting of metasomatized spinel peridotite beneath the ridge axis to generate E-MORB compositions (Donnelly *et al.*, 2004).

However, we show that mixing of deeply generated garnet pyroxenite melts with shallowly generated accumulated pyroxenite–peridotite melt mixes in a two-porosity melting and melt transport region results in excellent matches to both the incompatible element abundances and ratios of E-MORB and the trajectory of the EPR mixing array. In particular, our model produces both elevated highly incompatible element abundances and a shallow MREE/HREE slope, a common feature of E-MORB previously attributed to melting of spinel peridotite (Donnelly *et al.*, 2004).

Taken together, the results of this two-porosity melting–mixing model and the non-systematic U-series and paleointensity ages of E-MORB and N-MORB suggest that E-MORB and N-MORB may be produced concurrently and occupy the AMC at the same time. However, along-axis variations in the aspect ratio of the axial melt lens may inhibit along-axis mixing (e.g. Kent *et al.*, 1993), and we suggest that this may also affect the ability of N-MORB and E-MORB melts to mix. Because even small increases in the proportion of garnet pyroxenite melt vs N-MORB melt (<5%) can result in the eruption of E-MORB and not N-MORB, the less robust nature of magmatism at 9°30′N EPR and the western limb of the small OSC at 9°37′N compared with 9°50′N EPR may decrease melt sill thickness and inhibit along-axis mixing of geochemically variable melts. Thus, along-axis differences in the physical properties of the AMC owing to variations in magma supply may be directly related to the greater abundance of E-MORB erupted near 9°30′N and 9°37′N as compared with 9°50′N EPR.

ACKNOWLEDGEMENTS

We would like to thank Adam Soule, Maurice Tivey, Glenn Gaetani, Tim Grove, Dan Fornari, Matt Jackson, and Adam Goss for thoughtful comments and discussions that have helped to improve this study. We also thank Ken Macdonald and P. J. Fox for providing samples from the Abyssal Hills cruise. The paper benefited substantially from careful reviews of an earlier version by Craig Lundstrom, Charlie Langmuir, and Fred Frey. Constructive reviews by John Maclennan, Christophe Beier, and an anonymous reviewer further improved the quality of the paper.

FUNDING

This research was supported primarily by National Science Foundation (NSF) grants (OCE-0623838 and OCE-0137325) to K.W.W.S.; M.R.P. acknowledges NSF grants (OCE-9402360, 9403773, and 0138088) and J.B.T. acknowledges financial support from the French Institut National des Sciences de l'Univers.

SUPPLEMENTARY DATA

Supplementary data for this paper are available at *Journal of Petrology* online.

REFERENCES

Alexander, R. T. & Macdonald, K. C. (1996*a*). Small off-axis volcanoes on the East Pacific Rise. *Earth and Planetary Science Letters* **139**, 387–394.

Alexander, R. T. & Macdonald, K. C. (1996*b*). Sea Beam, SeaMARC II and *ALVIN*-based studies of faulting on the East Pacific Rise 9°20′N–9°50′N. *Marine Geophysical Researches* **18**, 557–587.

Allan, J. F., Batiza, R., Perfit, M. R., Fornari, D. J. & Sack, R. O. (1989). Petrology of lavas from the Lamont Seamount Chain and adjacent East Pacific Rise, 10°N. *Journal of Petrology* **30(5)**, 1245–1298.

Allègre, C. J. & Turcotte, D. L. (1986). Implications of a two-component marble-cake mantle. *Nature* **323**, 123–127.

Allègre, C. J., Hart, S. R. & Minster, J.-F. (1983). Chemical structure and evolution of the mantle and continents determined by inversion of Nd and Sr isotopic data, I. Theoretical methods. *Earth and Planetary Science Letters* **66**, 177–190.

Ball, L., Sims, K. W. W. & Schweiters, J. (2008). Measurement of ^{234}U/^{238}U and ^{230}Th/^{232}Th in volcanic rocks using the Neptune MC-ICP-MS. *Journal of Analytical Atomic Spectrometry* **23**, 173–180.

Batiza, R. & Niu, Y. (1992). Petrology and magma chamber processes at the East Pacific Rise–9°30′N. *Journal of Geophysical Research* **97**, 6779–6797.

Beattie, P. (1993). Uranium–thorium disequilibria and partitioning on melting of garnet peridotite. *Earth and Planetary Science Letters* **363**, 63–65.

Ben Othman, D. & Allègre, C. J. (1990). U–Th isotopic systematics at 13°N East Pacific Ridge segment. *Earth and Planetary Science Letters* **98**, 129–137.

Bergmanis, E. C., Sinton, J. & Rubin, K. H. (2007). Recent eruptive history and magma reservoir dynamics on the East Pacific Rise at 17°30′S. *Geochemistry, Geophysics, Geosystems* **8(12)**, doi:10.1029/2207GC001742.

Blichert-Toft, J. & Albarède, F. (1997). The Lu–Hf isotope geochemistry of chondrites and the evolution of the mantle–crust system. *Earth and Planetary Science Letters* **148**, 243–258.

Blichert-Toft, J., Chauvel, C. & Albarède, F. (1997). Separation of Hf and Lu for high-precision isotope analysis of rock samples by magnetic sector-multiple collector ICP-MS. *Contributions to Mineralogy and Petrology* **127**, 248–260.

Bowles, J., Gee, J. G., Kent, D. V., Perfit, M. R., Soule, S. A. & Fornari, D. J. (2006). Paleointensity applications to timing and extent of eruptive activity, 9–10°N East Pacific Rise. *Geochemistry, Geophysics, Geosystems* **7(6)**, paper number 2005GC001141.

Bryce, J. G., DePaolo, D. J. & Lassiter, J. C. (2005). Geochemical structure of the Hawaiian plume: Sr, Nd, and Os isotopes in the 2·8 km HSDP-2 section of Mauna Kea volcano. *Geochemistry, Geophysics, Geosystems* **6(9)**, paper number 2004GC000809.

Canales, J. P., Singh, S. C., Detrick, R. S., Carbotte, S. M., Harding, A., Kent, G. M., Diebold, J. B., Babcock, J. & Nedimovic, M. R. (2006). Seismic evidence for variations in axial magma chamber properties along the southern Juan de Fuca Ridge. *Earth and Planetary Science Letters* **246**, 353–366.

Carbotte, S. M. & Macdonald, K. C. (1992). East Pacific Rise 8–10°30′N: Evolution of ridge segments and discontinuities from SeaMARC II and three-dimensional magnetic studies. *Journal of Geophysical Research* **97**, 6959–6982.

Castillo, P. R., Klein, E., Bender, J., Langmuir, C., Shirey, S., Batiza, R. & White, W. (2000). Petrology and Sr, Nd, and Pb isotope geochemistry of mid-ocean ridge basalt glasses from the 11°45′N to 15°00′N segment of the East Pacific Rise. *Geochemistry, Geophysics, Geosystems* **1**, paper number 1999GC000024.

Chazey III, W. J., Neal, C. R., Jain, J. C. & Kinman, W. S. (2003). A reappraisal of Rb, Y, Zr, Pb, and Th values in geochemical reference material BHVO-1. *Geostandards Newsletter* **27**, 181–192.

Christeson, G. L., Purdy, G. M. & Fryer, G. J. (1994). Seismic constraints on shallow crustal emplacement processes at the fast-spreading East Pacific Rise. *Journal of Geophysical Research* **99**, 17957–17973.

Christeson, G. L., Kent, G. M., Purdy, G. M. & Detrick, R. S. (1996). Extrusive thickness variability at the East Pacific Rise, 9–10°N, constraints from seismic techniques. *Journal of Geophysical Research* **101**, 2859–2873.

Cochran, J. R., Fornari, D. J., Coakley, B. J., Herr, R. & Tivey, M. A. (1999). Continuous near-bottom gravity measurements made with a BGM-3 gravimeter in DSV *Alvin* on the East Pacific Rise crest near 9°30′N and 9°50′N. *Journal of Geophysical Research* **104**, 10841–10861.

Crawford, W. C. & Webb, E. S. (2002). Variations in the distribution of magma in the lower crust and at the Moho beneath the East Pacific Rise at 9–10°N. *Earth and Planetary Science Letters* **203**, 117–130.

DePaolo, D. J. & Wasserburg, G. J. (1976). Nd isotopic variations and petrogenetic models. *Geophysical Research Letters* **3(5)**, 249–252.

Donnelly, K. E., Goldstein, S. L., Langmuir, C. H. & Spiegelman, M. (2004). Origin of enriched ocean ridge basalts and implications for mantle dynamics. *Earth and Planetary Science Letters* **226**, 347–366.

Dunn, R.A., Toomey, D.R. & Solomon, S.C. (2000). Three-dimensional structure and physical properties of the crust and shallow mantle beneath the East Pacific Rise. *Journal of Geophysical Research* **105(B10)**, 23537–23555.

Elkins, L. J., Gaetani, G. A. & Sims, K. W. W. (2008). Partitioning of U and Th during garnet pyroxenite partial melting: Constraints on the source of alkaline ocean island basalts. *Earth and Planetary Science Letters* **265**, 270–286.

Escartin, J., Soule, S. A., Fornari, D. J., Tivey, M. A., Schouten, H. & Perfit, M. R. (2007). Interplay between faults and lava flows in construction of the upper oceanic crust: The East Pacific Rise crest 9°25′–9°58′N. *Geochemistry, Geophysics, Geosystems* **8**, Q06005, 20 pp., doi:10.1029/2006GC001399.

Fornari, D. J., Perfit, M. R., Allan, J. F. & Batiza, R. (1988). Small-scale heterogeneities in depleted mantle sources—near-ridge seamount lava geochemistry and implications for mid-ocean ridge magmatic processes. *Nature* **331**, 511–513.

Fornari, D. J., Perfit, M. R., Allan, J. F., Batiza, R., Haymon, R., Barone, A., Ryan, W. B. F., Smith, T., Simkin, T. & Luckman, M. A. (1989). Geochemical and structural studies of the Lamont Seamount—seamounts as indicators of mantle processes. *Earth and Planetary Science Letters* **89(1)**, 63–83.

Fornari, D., Haymon, R., Perfit, M., Gregg, T. K. P. & Edwards, M. H. (1998). Axial summit trough of the East Pacific Rise, 9–10°N: Geological characteristics and evolution of the axial zone on fast spreading mid-ocean ridges. *Journal of Geophysical Research* **103**, 9827–9855.

Fornari, D., Tivey, M., Schouten, H., Perfit, M., Yoerger, D., Bradley, A., Edwards, M., Haymon, R., Scheirer, D., Von Damm, K., Shank, T. & Soule, A. (2004). Submarine lava flow emplacement at the East Pacific Rise 9°50′N: implications for uppermost ocean crust stratigraphy and hydrothermal fluid circulation. In: German, C. R., Lin, J. & Parson, L. M. (eds) *Mid-Ocean Ridges: Hydrothermal Interactions between the Lithosphere and Oceans. Geophysical Monographs, American Geophysical Union* **148**, 187–217.

Galer, S. J. G. & O'Nions, R. K. (1986). Magmagenesis and the mapping of chemical and isotopic variations in the mantle. *Chemical Geology* **56**, 45–61.

Goldstein, S. J., Murrell, M. T., Janecky, D. R., Delaney, J. R. & Clague, D. A. (1992). Erratum to Geochronology and petrogenesis of MORB from the Juan de Fuca and Gorda ridges by ^{238}U–^{230}Th disequilibrium. *Earth and Planetary Science Letters* **109**, 255–272.

Goldstein, S. J., Murrell, M. T. & Williams, R. W. (1993). ^{231}Pa and ^{230}Th chronology of mid-ocean ridge basalts. *Earth and Planetary Science Letters* **115**, 151–159.

Goldstein, S. J., Perfit, M. R., Batiza, R., Fornari, D. J. & Murrell, M. T. (1994). Off-axis volcanism at the East Pacific Rise detected by uranium-series dating of basalts. *Nature* **367**, 157–159.

Goss, A. R., Perfit, M. R., Ridley, W. I., Rubin, K. H., Kamenow, G. D., Soule, S. A., Fundis, A. & Fornari, D. J. (2010). Geochemistry of lavas from the 2005–2006 eruption at the East Pacific Rise, 9°46′N–9°56′N: Implications for ridge crest plumbing and decadal changes in magma chamber compositions. *Geochemistry, Geophysics, Geosystems* **11(5)**, doi:10.1029/2009GC002977.

Harding, A. J., Kent, G. M. & Orcutt, J. A. (1993). A multichannel seismic investigation of upper crustal structure at 9°N on the East Pacific Rise: Implications for crustal accretion. *Journal of Geophysical Research* **98**, 13925–13944.

Harpp, K., White, W. M. & Batiza, R. (1990). Isotopic study of contrasting magmatic studies: The East Pacific Rise at 9°30′N and the MAR in the FAMOUS area. *EOS Transactions, American Geophysical Union* **71**, ,658.

Hart, S. R. & Blusztajn, J. (2006). Age and geochemistry of the mafic sills, ODP site 1276, Newfoundland margin. *Chemical Geology*, doi:10.1016/j.chemgeo.2006.07.001.

Hart, S. R., Schilling, J.-G. & Powell, J. L. (1973). Basalts from Iceland and along Reykjanes Ridge Sr isotope geochemistry. *Nature, Physical Science* **246(155)**, 104–107.

Hart, S. R., Workman, R. K., Ball, L. & Blusztajn, J. (2004). High precision Pb isotope techniques from the WHOI NEPTUNE PIMMS. WHOI Plasma Facility Open File Technical Report 10. http://www.whoi.edu/science/GG/people/shart/openfile.htm.

Hauri, E. H., Wagner, T. P. & Grove, T. L. (1994). Experimental and natural partitioning of Th, U, Pb, and other trace elements

between garnet, clinopyroxene, and basaltic melts. *Chemical Geology* **117**, 149–166.

Haymon, R. M., Fornari, D. J., Von Damm, K. L., Lilley, M. D., Perfit, M. R. & Edmond, J. M. (1993). Volcanic eruption of the mid-ocean ridge along the East Pacific Rise crest at 9°45–45′N: Direct submersible observations of seafloor phenomena associated with an eruption event in April, 1991. *Earth and Planetary Science Letters* **119**, 85–101.

Hedge, C. E. & Peterman, Z. E. (1970). The strontium isotopic composition of basalts from the Gordo and Juan de Fuca Rises, northeastern Pacific Ocean. *Contributions to Mineralogy and Petrology* **27**, 114–120.

Hekinian, R., Thompson, G. & Bideau, D. (1989). Axial and off-axial heterogeneity of basaltic rocks from the East Pacific Rise at 12°35′N–12°51′N and 11°26′N–11°30′N. *Journal of Geophysical Research* **94(B12)**, 17437–17463.

Hemond, C., Hofmann, A. W., Vlastélic, I. & Nauret, F. (2006). Origin of MORB enrichment and relative trace element compatibilities along the Mid-Atlantic Ridge between 10° and 24°N. *Geochemistry, Geophysics, Geosystems* **7(12)**, paper number 2006GC001317.

Henderson, G. M., Cohen, A. S. & Onions, R. K. (1993). U-234/U-238 ratios and Th-230 ages for Hateruma Atoll corals—implications for coral diagenesis and seawater U-234/U-238 ratios. *Earth and Planetary Science Letters* **115**, 65–73.

Hinds, J. (2005). Construction of the oceanic crustal layer 2A: a detailed petrographic and geochemical study of lavas from 9°30′N and 9°50′N East Pacific Rise. M.S. Thesis, University of Florida.

Hirschmann, M. M. (2000). Mantle solidus: Experimental constraints and the effects of peridotite composition. *Geochemistry, Geophysics, Geosystems* **1**, paper number 2000GC000070.

Hirschmann, M. M. & Stolper, E. M. (1996). A possible role for garnet pyroxenite in the origin of the 'garnet signature' in MORB. *Contributions to Mineralogy and Petrology* **124**, 185–208.

Hirschmann, M. M., Kogiso, T., Baker, M. B. & Stolper, E. M. (2003). Alkalic magmas generated by partial melting of garnet pyroxenite. *Geology* **31(6)**, 481–484.

Hooft, E. E. E., Schouten, H. & Detrick, R. S. (1996). Constraining crustal emplacement processes from the variation in seismic layer 2A thickness at the East Pacific Rise. *Earth and Planetary Science Letters* **142**, 289–309.

Hurley, P. M. (1968). Absolute abundance and distribution of Rb, K, and Sr in the Earth. *Geochimica et Cosmochimica Acta* **32**, 273–288.

Ita, J. & Stixrude, L. (1992). Petrology, elasticity, and composition of the mantle transition zone. *Journal of Geophysical Research* **97**, 6849–6866.

Jarosewich, E., Nelen, J. A. & Norberg, J. A. (1979). Electron microprobe reference samples for mineral analysis. In: Fudali, R. F. (ed.) *Mineral Sciences Investigations 1976–1977; Smithsonian Contributions to the Earth Sciences* **22**, 68–72.

Jochum, K. P., Nohl, U., Herwig, K., Lammel, E., Stoll, B. & Hofmann, A. W. (2005). GeoReM: a new geochemical database for reference materials and isotopic standards. *Geostandards and Geoanalytical Research* **29**, 333–338.

Jull, M., Kelemen, P. B. & Sims, K. (2002). Consequences of diffuse and channelled porous melt migration on uranium series disequilibria. *Geochimica et Cosmochimica Acta* **66(23)**, 4133–4148.

Kelemen, P. B., Hirth, G., Shimizu, N., Spiegelman, M. & Dick, H. J. B. (1997). A review of melt migration processes in the adiabatically upwelling mantle beneath oceanic spreading ridges. *Philosophical Transactions of the Royal Society of London, Series A* **355(1723)**, 283–318.

Kent, G. M., Harding, A. J. & Orcutt, J. A. (1993). Distribution of magma beneath the East Pacific Rise between the Clipperton Transform and the 9°17′N Deval from forward modeling of Common Depth Point data. *Journal of Geophysical Research* **98(B8)**, 13945–13969.

Klein, E. M. & Langmuir, C. H. (1987). Global correlations of ocean ridge basalt chemistry with axial depth and crustal thickness. *Journal of Geophysical Research* **92**, 853–874.

Kogiso, T., Hirschmann, M. M. & Frost, D. J. (2003). High-pressure partial melting of garnet pyroxenite: possible mafic lithologies in the source of ocean island basalts. *Earth and Planetary Science Letters* **216**, 603–617.

Ku, T.-L., Knauss, K. G. & Mathieu, G. G. (1977). Uranium in open ocean: Concentration and isotopic composition. *Deep-Sea Research* **24**, 1005–1017.

Kurras, G. J., Fornari, D. J., Edwards, M. H., Perfit, M. R. & Smith, M. C. (2000). Volcanic morphology of the East Pacific Rise crest 9°49′–52′N: implications for volcanic emplacement processes at fast-spreading mid-ocean ridges. *Marine Geophysical Researches* **21(1)**, 23–41.

Kutza, S. (2002). Petrology and geochemistry of mid-ocean ridge basalts from the East Pacific Rise (9°24′ and 10°06′N): Implications for off-axis magmatic processes. M.S. thesis, University of Florida, Gainesville.

Laj, C., Kissel, C., Mazaud, A., Channel, J. E. T. & Beer, J. (2000). North Atlantic palaeointensity stack since 75 ka (NAPIS-75) and the duration of the Laschamp event. *Philosophical Transactions of the Royal Society of London, Series A* **358(1768)**, 1009–1025.

Landwehr, D., Blundy, J., Chamorro-Perez, E. M., Hill, E. & Wood, B. (2001). U-series disequilibria generated by partial melting of spinel lherzolite. *Earth and Planetary Science Letters* **188**, 329–348.

Langmuir, C. H., Bender, J. F. & Batiza, R. (1986). Petrological and tectonic segmentation of the East Pacific Rise, 5°30′–14°30′N. *Nature* **322**, 422–429.

LaTourette, T. Z., Kennedy, A. K. & Wasserburg, G. J. (1993). Uranium–thorium fractionation of garnet—evidence for a deep source and rapid rise of oceanic basalts. *Science* **261**, 739–742.

Lundstrom, C. C. (2000). Models of U-series disequilibria generation in MORB: the effects of two scales of melt porosity. *Physics of the Earth and Planetary Interiors* **121**, 189–204.

Lundstrom, C. C., Gill, J., Williams, Q. & Perfit, M. R. (1995). Mantle melting and basalt extraction by equilibrium porous flow. *Science* **270(5244)**, 1958–1961.

Lundstrom, C. C., Williams, Q. & Gill, J. B. (1998). Investigating solid mantle upwelling rates beneath mid-ocean ridges using U-series disequilibria, 1: a global approach. *Earth and Planetary Science Letters* **157**, 151–165.

Lundstrom, C. C., Sampson, D. E., Perfit, M. R., Gill, J. & Williams, Q. (1999). Insights into mid-ocean ridge basalt petrogenesis: U-series disequilibria from the Siqueiros Transform, Lamont Seamounts, and East Pacific Rise. *Journal of Geophysical Research* **104(B6)**, 13035–13048.

Macdonald, K. C., Sempere, J.-C. & Fox, P. J. (1984). East Pacific Rise from Siquieros to Orozco fracture zones: Along-strike continuity of axial neovolcanic zone and structure and evolution of overlapping spreading centers. *Journal of Geophysical Research* **89**, 6049–6069.

Macdonald, K. C., Fox, P. J., Alexander, R. T. *et al.* (1996). Volcanic growth faults and the origin of Pacific abyssal hills. *Nature* **380**, 125–129.

Mahoney, J. J., Sinton, J. M., Kurz, M. D., Macdougall, J. D., Spencer, K. J. & Lugmair, G. W. (1994). Isotope and trace element characteristics of a super-fast spreading ridge: East Pacific rise, 13–23°S. *Earth and Planetary Science Letters* **121**, 173–193.

McDonough, W. F. & Sun, S. S. (1995). The composition of the Earth. *Chemical Geology* **120**, 223–253.

Nauret, F., Abouchami, W., Galer, S. J. G., Hofmann, A. W., Hémond, C., Chauvel, C. & Dyment, J. (2006). Correlated trace element–Pb isotope enrichments in Indian MORB along 18–20°S, Central Indian Ridge. *Earth and Planetary Science Letters* **245**, 137–152.

Niu, Y. L. & Batiza, R. (1997). Trace element evidence from seamounts for recycled oceanic crust in the eastern Pacific mantle. *Earth and Planetary Science Letters* **148**, 471–483.

Niu, Y. & O'Hara, M. J. (2008). Global correlations of ocean ridge basalt chemistry with axial depth: a new perspective. *Journal of Petrology* **49(4)**, 633–664.

Niu, Y., Collerson, K. D., Batiza, R., Wendt, J. I. & Regelous, M. (1999). Origin of enriched-type mid-ocean ridge basalt at ridges far from mantle plumes: The East Pacific Rise at 11°20′N. *Journal of Geophysical Research* **104(B4)**, 7067–7087.

Niu, Y. L., Regelous, M., Wendt, I. J., Batiza, R. & O'Hara, M. J. (2002). Geochemistry of near-EPR seamounts: importance of source vs process and the origin of enriched mantle component. *Earth and Planetary Science Letters* **199**, 327–345.

Perfit, M. R. & Chadwick, W. W., Jr (1998). Magmatism at mid-ocean ridges: Constraints from volcanological and geochemical investigations. In: Buck, W. R., Delaney, P., Karson, J. A. & Lababrille, Y. (eds) *Faulting and Magmatism at Mid-Ocean Ridges. Geophysical Monograph, American Geophysical Union* **106**, 41–70.

Perfit, M., Fornari, D., Smith, M., Bender, J., Langmuir, C. & Haymon, R. (1994). Small-scale spatial and temporal variations in MORB geochemistry and implications for ridge crest magmatic processes. *Geology* **22**, 375–379.

Perfit, M. R., Fornari, D. J., Ridley, W. I., Kirk, P. D., Casey, J., Kastens, K. A., Reynolds, J. R., Edwards, M., Desonie, D., Shuster, R. & Paradis, S. (1996). Recent volcanism in the Siqueiros transform fault: picritic basalts and implications for MORB magma genesis. *Earth and Planetary Science Letters* **141**, 91–108.

Pertermann, M. & Hirschmann, M. M. (2003). Partial melting experiments on a MORB-like pyroxenite between 2 and 3 GPa: Constraints on the presence of pyroxenite in basalt source regions from solidus location and melting rate. *Journal of Geophysical Research* **108(B2)**, doi:10.1029/2000JB000118.

Pertermann, M., Hirschmann, M. M., Hametner, K., Gunther, K. & Schmidt, M. W. (2004). Experimental determination of trace element partitioning between garnet and silica-rich liquid during anhydrous partial melting of MORB-like eclogite. *Geochemistry, Geophysics, Geosystems* **5(5)**, paper number 2003GC000638.

Prinzhofer, A., Lewin, E. & Allègre, C. J. (1989). Stochastic melting of the marble cake mantle—evidence from local study of the East Pacific Rise at 12°50′N. *Earth and Planetary Science Letters* **92(2)**, 189–206.

Reynolds, J. R. (1995). Segment-scale systematic of mid-ocean ridge magmatism and geochemistry. Ph.D. thesis. Columbia University, Palisades NY, 483 p.

Reynolds, J. R. & Langmuir, C. H. (2000). Identification and implications of off-axis lava flows around the East Pacific Rise. *Geochemistry, Geophysics, Geosystems* **1**, paper number 1999GC000033.

Reynolds, J. R., Langmuir, C. H., Bender, J. F., Kastens, K. A. & Ryan, W. B. F. (1992). Spatial and temporal variability in the geochemistry of basalts from the East Pacific Rise. *Nature* **359**, 493–499.

Richter, S. & Goldberg, S. A. (2003). Improved techniques for high accuracy isotope ratio measurements of nuclear materials using thermal ionization mass spectrometry. *International Journal of Mass Spectrometry* **229**, 181–197.

Robinson, L. F., Belshaw, N. S. & Henderson, G. M. (2004). U and Th concentrations and isotope ratios in modern carbonates and waters from the Bahamas. *Geochimica et Cosmochimica Acta* **68(8)**, 1777–1789.

Rubin, K., MacDougall, J. D. & Perfit, M. R. (1994). ^{210}Po–^{210}Pb dating of recent volcanic eruptions on the sea floor. *Nature* **368**, 841–844.

Rubin, K., van der Zander, I., Smith, M. C. & Bergmanis, E. C. (2005). Minimum speed limit for ocean ridge magmatism from ^{210}Pb–^{226}Ra–^{230}Th disequilibria. *Nature* **437**, 534–538.

Salters, V. J. M. & Longhi, J. E. (1999). Trace element partitioning during the initial stages of melting beneath ocean ridges. *Earth and Planetary Science Letters* **166**, 15–30.

Salters, V. J. M., Longhi, J. E. & Bizimis, M. (2002). Near mantle solidus trace element partitioning at pressures up to 3·4 GPa. *Geochemistry, Geophysics, Geosystems* **3(7)**, paper number 2001GC000148.

Scheirer, D. S. & Macdonald, K. C. (1993). Variation in cross-sectional area of the axial ridge along the East Pacific Rise: Evidence for the magmatic budget of a fast spreading center. *Journal of Geophysical Research* **98**, 22321–22338.

Schouten, H., Tivey, M. A., Fornari, D. J. & Cochran, J. R. (1999). Central anomaly magnetization high: constraints on the volcanic construction and architecture of seismic layer 2A at a fast-spreading mid-ocean ridge, the EPR at 9°30′–50′N. *Earth and Planetary Science Letters* **169**, 37–50.

Schouten, H., Tivey, M. A., Fornari, D. J., Yoerger, D., Bradley, A., Edwards, M., Johnson, P. & Ship Board Science and Technical Teams (2001). Near-bottom investigations of the central anomaly magnetic high (CAMH) at the East Pacific Rise 9°25′–57′N, cruise report R/V Atlantis Voyage 7 Leg 4, 11/05-12/04/2001 (Available at http://imina.soest.hawaii.edu/HMRG/EPR/index.htm).

Schouten, H., Tivey, M., Fornari, D., Yoerger, D., Bradley, A., Johnson, P., Edwards, M. & Kurokawa, T. (2002). Lava transport and accumulation processes on EPR 9°27′N to 10°N: Interpretations based on recent near-bottom sonar imaging and seafloor observations using ABE, Alvin and a new digital deep sea camera. *Eos Transactions, American Geophysical Union*, **83**(47), Fall Meeting Supplement, Abstract T11C-1262.

Sims, K. W. W. & DePaolo, D. J. (1997). Inferences about mantle magma sources from incompatible element concentration ratios in oceanic basalts. *Geochimica et Cosmochimica Acta* **61(4)**, 765–784.

Sims, K. W. W. & Hart, S. R. (2006). Comparison of Th, Sr, Nd, and Pb isotopes in oceanic basalts: Implications for mantle heterogeneity and magma genesis. *Earth and Planetary Science Letters* **245**, 743–761.

Sims, K. W. W., DePaolo, D. J., Murrell, M. T., Baldridge, W. S., Goldstein, S. J. & Clague, D. (1995). Mechanisms of magma generation beneath Hawaii and mid-ocean ridges: uranium/thorium and samarium/neodymium isotopic evidence. *Science* **267(5197)**, 508–512.

Sims, K. W. W., Kelemen, P. & Jull, M. (1999). U-series disequilibria and melt transport in the mantle beneath mid-ocean ridges. Presented at American Geophysical Union Meeting, San Francisco, CA. *EOS Transactions, American Geophysical Union*, abstract V22D.

Sims, K. W. W., Goldstein, S. J., Blichert-Toft, J., Perfit, M. R., Kelemen, P., Fornari, D. J., Michael, P., Murrell, M. T., Hart, S. R., DePaolo, D. J., Layne, G. & Jull, M. (2002). Chemical and isotopic constraints on the generation and transport of melt beneath the East Pacific Rise. *Geochimica et Cosmochimica Acta* **66**, 3481–3504.

Sims, K. W. W., Blichert-Toft, J., Fornari, D. J., Perfit, M. R., Goldstein, S. J., Johnson, P., DePaolo, D. J., Hart, S. R., Murrell, M. T., Michael, P. J., Layne, G. D. & Ball, L. (2003).

Aberrant youth: Chemical and isotopic constraints on the origin of off-axis lavas from the East Pacific Rise, 9–10°N. *Geochemistry, Geophysics, Geosystems* **4(10)**, paper number 2002GC000443.

Sims, K. W. W., Hart, S. R., Reagan, M. K., Blusztajn, J., Staudigel, H., Sohn, R. A., Layne, G. D., Ball, L. A. & Andrews, J. (2008a). ^{238}U–^{230}Th–^{226}Ra–^{210}Pb–^{210}Po, ^{232}Th–^{228}Ra, and ^{235}U–^{231}Pa constraints on the ages and petrogenesis of Vailulu′u and Malumalu Lavas, Samoa. *Geochemistry, Geophysics, Geosystems* **9**(4), paper number 2007GC001651.

Sims, K. W. W., Gill, J. B., Dosseto, A., Hoffmann, D. L., Lundstrom, C. C., Williams, R. W., Ball, L., Tollstrup, D., Turner, S., Prytulak, J., Glessner, J. J. G., Standish, J. J. & Elliot, T. (2008*b*). An inter-laboratory assessment of the thorium isotopic composition of synthetic and rock reference materials. *Geostandards and Geoanalytical Research* **32**, 65–91.

Singh, S. C., Kent, G. M., Collier, J. S., Harding, A. J. & Orcutt, J. A. (1998). Melt to mush variations in crustal magma properties along the ridge crest at the southern East Pacific Rise. *Nature* **394**, 874–878.

Smith, M. C., Perfit, M. R., Fornari, D. J., Ridley, W. I., Edwards, M. H., Jurras, G. J. & Von Damm, K. L. (2001). Magmatic processes and segmentation at a fast spreading mid-ocean ridge; detailed investigation of an axial discontinuity on the East Pacific Rise crest at 9°37′N. *Geochemistry, Geophysics, Geosystems* **2**, paper number 2000GC000134.

Sohn, R. A., Webb, S. C. & Hildebrand, J. A. (2004). Fine-scale seismic structure of the shallow volcanic crust on the East Pacific Rise at 9°50′N. *Journal of Geophysical Research* **109**, B12104, doi:10.1029/2004JB003152.

Soule, S. A., Fornari, D. J., Perfit, M. R., Tivey, M. A., Ridley, W. I. & Schouten, H. (2005). Channelized lava flows at the East Pacific Rise crest 9–10°N: The importance of off-axis lava transport in developing the architecture of young oceanic crust. *Geochemistry, Geophysics, Geosystems* **6(8)**, paper number 2005GC000912.

Soule, S. A., Fornari, D. J., Perfit, M. R. & Rubin, K. H. (2007). New insights into mid-ocean ridge volcanic processes from the 2005–2006 eruption of the East Pacific Rise, 9°46′N–9°56′N. *Geology* **35(12)**, 1079–1082.

Soule, S. A., Escartin, J. E. & Fornari, D. J. (2009). A record of eruption and intrusion at a fast-spreading ridge axis: the axial summit trough of the East Pacific Rise. *Geochemistry, Geophysics, Geosystems* **10**, Q10T07, paper number 2008GC002354.

Stracke, A. & Bourdon, B. (2009). The importance of melt extraction for tracing mantle heterogeneity. *Geochimica et Cosmochimica Acta* **73**, 218–238.

Tatsumoto, M. (1966). Genetic relations of oceanic basalts as indicated by lead isotopes. *Science* **153**, 1094–1101.

Thornber, C. R., Sherrod, D. R., Siems, D. F., Heliker, C. C., Meeker, G. P., Oscarson, R. L. & Kauahikaua, J. P. (2002). Whole-rock and glass major-element geochemistry of Kilauea Volcano, Hawaii, near-vent eruptive products: September 1994 through September 2001. *US Geological Survey Open-File Report* **02–17**, 9.

Thurber, D. (1962). Anomalous ^{234}U/^{238}U in nature. *Journal of Geophysical Research* **67**, 4518.

Todt, W., Cliff, R. A., Hanser, A. & Hofmann, A. W. (1996). Evaluation of a ^{202}Pb–^{205}Pb double spike for high-precision lead isotope analysis. In: Hart, S. R. & Basu, A. (eds) *Earth Processes: Reading the Isotopic Code. Geophysical Monograph, American Geophysical Union* **95**, 429–437.

Tolstoy, M., Cohen, J. P., Baker, E. T., Fornari, D. J., Rubin, K. H., Shank, T. M., Waldhauser, F., Bohnenstiehl, D. R., Forsyth, D. W., Holmes, R. C., Love, B., Perfit, M. R., Weekly, R. T., Soule, S. A. & Glazer, B. (2006). A seafloor spreading event captured by seismometers. *Science Express*, 10.1126/science.1133950.

Toomey, D. R., Solomon, S. C. & Purdy, G. M. (1994). Tomographic imaging of the shallow crustal structure of the East Pacific Rise at 9°30′N. *Journal of Geophysical Research* **99(B12)**, 24,135–24,157.

Vera, E. E. & Diebold, J. B. (1994). Seismic imaging of oceanic layer 2A between 9°30 and 10°N on the East Pacific Rise from two ship wide-aperture profiles. *Journal of Geophysical Research* **99**, 3031–3041.

Volpe, A. M. & Goldstein, S. J. (1990). Dating young MORB: ^{226}Ra–^{230}Th isotopic disequilibria measured by mass spectrometer. *EOS Transactions, American Geophysical Union* **71**, 1702.

Volpe, A. M. & Goldstein, S. J. (1993). ^{226}Ra–^{230}Th disequilibrium in axial and off-axis mid-ocean ridge basalts. *Geochimica et Cosmochimica Acta* **57**, 1233–1242.

White, S. M., Haymon, R. M., Fornari, D. J., Perfit, M. R. & Macdonald, K. C. (2002). Correlation between volcanic and tectonic segmentation of fast-spreading ridges: evidence from volcanic structures and lava flow morphology on the East Pacific Rise at 9–10°N. *Journal of Geophysical Research* **107(B8)**, doi:10.1029/2002GC000443.

White, W. M. & Schilling, J.-G. (1978). The nature and origin of geochemical variation in Mid-Atlantic Ridge basalts from the Central North Atlantic. *Geochimica et Cosmochimica Acta* **42**, 1501–1516.

Workman, R. K. & Hart, S. R. (2005). Major and trace element composition of the depleted MORB mantle (DMM). *Earth and Planetary Science Letters* **231**, 53–72.

Zindler, A. & Hart, S. R. (1986). Chemical geodynamics. *Annual Review of Earth and Planetary Sciences* **14**, 493–571.

Zindler, A., Staudigel, H. & Batiza, R. (1984). Isotope and trace element geochemistry of young Pacific seamounts: implications for the scale of upper mantle heterogeneity. *Earth and Planetary Science Letters* **70(2)**, 175–195.